

NUREG/CR-3822  
LA-10132-MS

Los Alamos National Laboratory is operated by the University of California for the United States Department of Energy under contract W-7409-ENG-88.

## ***SOLA-PTS:***

***A Transient, Three-Dimensional Algorithm  
for Fluid-Thermal Mixing and Wall Heat Transfer  
in Complex Geometries***

**Los Alamos** Los Alamos National Laboratory  
Los Alamos, New Mexico 87545

8409110081 840731  
PDR NUREG  
CR-3822 R PDR

Affirmative Action/Equal Opportunity Employer

Prepared by Adrienne Hayes, Group T-3

NOTICE

This report was prepared as an account of work sponsored by an agency of the United States Government. Neither the United States Government nor any agency thereof, or any of their employees, makes any warranty, expressed or implied, or assumes any legal liability or responsibility for any third party's use, or the results of such use, of any information, apparatus, product or process disclosed in this report, or represents that its use by such third party would not infringe privately owned rights.

NUREG/CR-3822  
LA-10132-MS

R4

## **SOLA-PTS:**

### **A Transient, Three-Dimensional Algorithm for Fluid-Thermal Mixing and Wall Heat Transfer in Complex Geometries**

Bart J. Daly  
Martin D. Torrey

Manuscript submitted: May 1984  
Date published: July 1984

Prepared for  
Division of Accident Evaluation  
Office of Nuclear Regulatory Research  
US Nuclear Regulatory Commission  
Washington, DC 20555

NRC FIN No. A7306

**Los Alamos** Los Alamos National Laboratory  
Los Alamos, New Mexico 87545

## CONTENTS

	Page
Nomenclature	v
Abstract	1
I. Introduction	1
II. The Physical Model	2
III. The Numerical Model	9
A. The Momentum Equations	10
B. The Temperature Equations	18
C. The Turbulence Equations	21
1. The $\epsilon$ Equation	22
2. The $k$ Equation	26
3. The $\overline{T'^2}$ Equation	26
IV. Experimental Comparisons	28
A. Creare Experiment 51	29
B. Creare Experiment 50	33
References	37
Appendix A. Comparison of the Turbulence Models	39
Appendix B. Running a Problem with SOLA-PTS	41

## NOMENCLATURE

A	Symmetric coefficient matrix in the pressure iteration
B	Van Driest's constant, 26.0
$c_{p_f}$	Specific heat of the fluid
$c_{p_m}$	Specific heat of the metal
E	Wall roughness parameter, 9.0 for a smooth wall
$E_Y$	Class of functions that are minimized by the Conjugate Gradient methods
$\underline{g}$	The gravitational acceleration
$\underline{h}$	Vector of source terms in the pressure iteration
$h_c$	Thickness of the wall clad
k	Turbulent kinetic energy
$\tilde{k}$	The turbulent kinetic energy after the first step in the solution
$k_b$	Thermal conductivity of the base metal
$k_c$	Thermal conductivity of the clad
kFLX	The turbulent kinetic energy advection terms
kLAG	The turbulent kinetic energy, less the advection terms, after the first step in the solution
$k_m$	Thermal conductivity of the metal
p	The fluid pressure
P	Round pipe to square duct perimeter ratio
$q_w$	Wall heat flux
$\underline{r}$	Vector of residual errors in the pressure iteration
t	Time
T	Temperature
$\tilde{T}$	The temperature after the first step in the solution
$\bar{T}$	The temperature after the third step in the solution
$\overline{T'^2}$ (= TPS)	The mean square fluctuating temperature
TC	Thermocouple number, from Creare experiments
TFLX	The temperature advection terms
TLAG	The temperature, less the advection terms, after the first step in the solution
$T_m$	Temperature of the metal
$T_o$	Reference temperature
$T_p$	Fluid temperature in a computation cell adjacent to a wall

$\tilde{T}PS$	The mean-square fluctuating temperature field after the first step in the solution
TPSFLX	The advection terms for the mean-square fluctuating temperature field
TPSLAG	The mean-square fluctuating temperature field, less the advection terms, after the first step in the solution
$T_w$	Temperature of a wall edge
U	The mean azimuthal velocity component
u	The fluctuating azimuthal velocity component
V	The mean axial velocity component
v	The fluctuating axial velocity component
VOL	The cell volume
W	The mean vertical velocity component
w	The fluctuating vertical velocity component
x	The azimuthal spatial component
y	The axial spatial component
z	The vertical spatial component
$\alpha$	The volumetric coefficient of expansion
$\beta$	Increment to thermal diffusion, from $k-\epsilon-T'^2$ model
$\delta$	Distance from the wall to the center of the computation cell
$\delta t$	The time increment
$\delta x$	The x-component spatial increment
$\delta y$	The y-component spatial increment
$\delta z$	The z-component spatial increment
$\epsilon$	Turbulent energy decay rate
$\tilde{\epsilon}$	The turbulent energy decay rate after the first step in the solution
$\epsilon FLX$	The turbulent energy decay rate advection terms
$\epsilon LAG$	The turbulent energy decay rate, less the advection terms, after the first step in the solution
$\kappa$	Von Karman's constant, 0.4
$\mu_T$	Turbulent viscosity
$\nu_L$	Laminar kinematic viscosity
$\rho$	Fluid density, assumed constant
$\rho_m$	Density of the metal
$\sigma_h$	Turbulent fluid Prandtl number
$\sigma_{h,l}$	Laminar fluid Prandtl number
$\sigma_T$	Turbulent thermal diffusion coefficient
$\tau_w$	Wall shear stress
vi	

SOLA-PTS: A TRANSIENT, THREE-DIMENSIONAL ALGORITHM FOR FLUID-THERMAL  
MIXING AND WALL HEAT TRANSFER IN COMPLEX GEOMETRIES

by

Bart J. Daly and Martin D. Torrey

ABSTRACT

The SOLA-PTS computer code has been developed to analyze fluid-thermal mixing in the cold legs and downcomer of pressurized water reactors in support of the pressurized thermal shock study. SOLA-PTS is a transient, three-dimensional code with the capability of resolving complex geometries using variable cell noding in the three coordinate directions. The computational procedure is second-order accurate and utilizes a state-of-the-art iteration method that allows rapid convergence to an accurate solution for the pressure field. Two different turbulence models are used in the code, a two-equation  $k-\epsilon$  model that is used in the cold leg pipe away from the HPI inlet and a three-equation  $k-\epsilon-T'^2$  model for use near the HPI inlet and in the downcomer.

The physical modeling and the numerical procedure used in SOLA-PTS are described in this report. Applications of the method to two Creare 1/5th-scale experiments are also presented. Two appendices are included. Appendix A provides a comparison of the two- and three-equation turbulence models, while Appendix B provides instructions for setting up and running a problem with SOLA-PTS.

---

I. INTRODUCTION

The SOLA-PTS code has been developed specifically to address the nuclear reactor safety problem that has been given the title pressurized thermal shock (PTS). The PTS question is concerned with the rapid cooling of a reactor vessel wall as the result of injecting cold water into the reactor downcomer, in response to an accident situation. The rapid chilling of the vessel wall can conceivably cause the propagation of cracks into the wall metal and result in the leakage of radioactive water into the containment region.

The numerical study of this problem involves three complementary analyses. A thermal-hydraulic systems study is needed to determine the response of the reactor to the accident situation and the consequent temperature distribution in the downcomer. However, this temperature distribution computed by the system code is not known in detail because the system study is coarsely noded and cannot account for thermal stratification of the fluid in the cold leg pipes. Therefore, a detailed three-dimensional analysis is required to compute the detailed mixing of fluid in the piping and downcomer and the transient temperature distribution at the vessel wall. The third part of the analysis is a fracture-mechanics study to determine the extent of crack propagation through the metal given the temperature history at the fluid interface.

The SOLA-PTS code fills the requirement for a detailed three-dimensional analysis of the fluid-thermal mixing in the downcomer. It calculates the injection of coolant water into the cold leg pipe that feeds the downcomer, the mixing and stratification of the flow in the cold leg, the injection of the cold fluid into the warm downcomer fluid, and the consequent buoyant mixing in the downcomer. These flows are highly turbulent, so the SOLA-PTS code utilizes a state-of-the-art turbulence model to compute the buoyancy- and shear-generated mixing processes. Furthermore, the code is second-order accurate so that diffusive numerical truncation errors do not overwhelm the real diffusion processes.

Eight partial differential equations are solved in a SOLA-PTS calculation: the momentum and continuity equations, the temperature equation, and three equations for computing turbulence parameters. These equations and the associated boundary conditions are described in Sec. II. The bulk of that section is concerned with the two separate turbulence models that are used in the code.

Section III is a detailed description of the numerical modeling used in SOLA-PTS. Two experimental comparisons with 1/5th-scale Creare data are presented in Sec. IV. Appendix A provides a comparison of the two- and three-equation turbulence models and the manner in which these are included in the momentum, energy, and turbulence equations. A careful study of this section is recommended to those who intend to use the code. Appendix B discusses the procedures used in setting up a SOLA-PTS calculation.

## II. THE PHYSICAL MODEL

The SOLA-PTS method is an outgrowth of the SOLA-3D numerical procedure developed by Hirt and Stein<sup>1</sup> and extended by Hirt, Ramshaw, and Stein.<sup>2</sup> In spe-



cializing the method to the pressurized thermal shock application a number of capabilities have been added to the code. These include a temperature transport equation and transport equations for the turbulent kinetic energy, the kinetic energy decay rate, and the mean square temperature fluctuations. In addition, a second-order accurate difference scheme, a provision for controlling numerical dispersion errors, and a state-of-the-art iteration procedure have been incorporated. A necessary extension for PTS applications was the capability of logically connecting subregions of different geometrical shapes.

In the SOLA-PTS code we solve the three-dimensional Navier-Stokes equations with turbulent diffusion, and we employ the Boussinesq approximation, in which variations in density are ignored except in the gravitational acceleration term. With these modifications the momentum equations are written \*

$$\begin{aligned} \frac{\partial U}{\partial t} + U \frac{\partial U}{\partial x} + V \frac{\partial U}{\partial y} + W \frac{\partial U}{\partial z} = - \frac{1}{\rho} \frac{\partial p}{\partial x} + g_x [1 - \alpha(T - T_o)] + \frac{2}{\rho} \frac{\partial}{\partial x} \left( \mu_T \frac{\partial U}{\partial x} \right) \\ + \frac{1}{\rho} \frac{\partial}{\partial y} \left[ \mu_T \left( \frac{\partial U}{\partial y} + \frac{\partial V}{\partial x} \right) \right] + \frac{1}{\rho} \frac{\partial}{\partial z} \left[ \mu_T \left( \frac{\partial W}{\partial x} + \frac{\partial U}{\partial z} \right) \right] , \end{aligned} \quad (1)$$

$$\begin{aligned} \frac{\partial V}{\partial t} + U \frac{\partial V}{\partial x} + V \frac{\partial V}{\partial y} + W \frac{\partial V}{\partial z} = - \frac{1}{\rho} \frac{\partial p}{\partial y} + g_y [1 - \alpha(T - T_o)] + \frac{2}{\rho} \frac{\partial}{\partial y} \left( \mu_T \frac{\partial V}{\partial y} \right) \\ + \frac{1}{\rho} \frac{\partial}{\partial z} \left[ \mu_T \left( \frac{\partial V}{\partial z} + \frac{\partial W}{\partial y} \right) \right] + \frac{1}{\rho} \frac{\partial}{\partial x} \left[ \mu_T \left( \frac{\partial U}{\partial y} + \frac{\partial V}{\partial x} \right) \right] , \text{ and} \end{aligned} \quad (2)$$

$$\begin{aligned} \frac{\partial W}{\partial t} + U \frac{\partial W}{\partial x} + V \frac{\partial W}{\partial y} + W \frac{\partial W}{\partial z} = - \frac{1}{\rho} \frac{\partial p}{\partial z} + g_z [1 - \alpha(T - T_o)] + \frac{2}{\rho} \frac{\partial}{\partial z} \left( \mu_T \frac{\partial W}{\partial z} \right) \\ + \frac{1}{\rho} \frac{\partial}{\partial x} \left[ \mu_T \left( \frac{\partial W}{\partial x} + \frac{\partial U}{\partial z} \right) \right] + \frac{1}{\rho} \frac{\partial}{\partial y} \left[ \mu_T \left( \frac{\partial V}{\partial z} + \frac{\partial W}{\partial y} \right) \right] . \end{aligned} \quad (3)$$

The mass and energy conservation equations are expressed in terms of the continuity condition and a temperature transport equation,

$$\frac{\partial U}{\partial x} + \frac{\partial V}{\partial y} + \frac{\partial W}{\partial z} = 0 , \text{ and} \quad (4)$$

\*The variables are defined in the Nomenclature.

$$\frac{\partial T}{\partial t} + U \frac{\partial T}{\partial x} + V \frac{\partial T}{\partial y} + W \frac{\partial T}{\partial z} = \frac{1}{\rho} \frac{\partial}{\partial x} \left( \sigma_T \frac{\partial T}{\partial x} \right) + \frac{1}{\rho} \frac{\partial}{\partial y} \left( \sigma_T \frac{\partial T}{\partial y} \right) + \frac{1}{\rho} \frac{\partial}{\partial z} \left( \sigma_T \frac{\partial T}{\partial z} \right) . \quad (5)$$

The thermal diffusion coefficient  $\sigma_T$  includes turbulent and laminar contributions. We use a turbulent Prandtl number 1.0 and a laminar Prandtl number 6.7, so the only difference between  $\mu_T$  and  $\sigma_T$  is in the laminar contribution. Generally, this is small.

Two different turbulence models are used in SOLA-PTS to represent the diffusion of momentum and heat. In buoyant-jet regions, such as the HPI inlet and the downcomer, a three-equation model<sup>3,4</sup> is used, while in the cold leg pipe away from the HPI inlet, a two-equation model<sup>5</sup> is used. In both cases we solve transport equations for the turbulent kinetic energy  $k$  and the turbulent energy-decay rate  $\epsilon$ , but in the three-equation model we also solve a transport equation for the mean square fluctuating temperature  $\overline{T'^2}$ . There are other differences between these models, as will be shown in their description below and in Appendix A. The principal difference is that the  $k$ - $\epsilon$ - $\overline{T'^2}$  model<sup>3,4</sup> results in much greater diffusion of momentum and energy than the  $k$ - $\epsilon$  model.<sup>5</sup> This greater diffusion is intended to represent the enhanced mixing with entrained ambient fluid in jets and plumes.

In the Launder-Spalding model<sup>5</sup> a turbulent eddy viscosity is obtained from the relation

$$\mu_T = c_\mu \rho k^2 / \epsilon , \quad (6)$$

with  $k$  and  $\epsilon$  determined by solution of the transport equations,

$$\frac{\partial k}{\partial t} + U_i \frac{\partial k}{\partial x_i} = \frac{1}{\rho} \frac{\partial}{\partial x_i} \left( \frac{\mu_T}{c_k} \frac{\partial k}{\partial x_i} \right) + \frac{\mu_T}{\rho} \left( \frac{\partial U_i}{\partial x_j} + \frac{\partial U_j}{\partial x_i} \right) \frac{\partial U_i}{\partial x_j} - \epsilon , \quad \text{and} \quad (7)$$

$$\frac{\partial \epsilon}{\partial t} + U_i \frac{\partial \epsilon}{\partial x_i} = \frac{1}{\rho} \frac{\partial}{\partial x_i} \left( \frac{\mu_T}{\sigma_\epsilon} \frac{\partial \epsilon}{\partial x_i} \right) + \frac{c_1 \mu_T}{\rho} \frac{\epsilon}{k} \left( \frac{\partial U_i}{\partial x_j} + \frac{\partial U_j}{\partial x_i} \right) \frac{\partial U_i}{\partial x_j} - c_2 \frac{\epsilon^2}{k} , \quad (8)$$

where, for conciseness, the summation convention has been used. After extensive examination of free turbulent flows, these authors recommend the values in Table I for the coefficients appearing in these equations.

TABLE I  
THE COEFFICIENTS OF THE k-ε MODEL

$c_\mu$	$c_1$	$c_2$	$\sigma_k$	$\sigma_\epsilon$
0.09	1.44	1.92	1.0	1.3

At a computation cell adjacent to a rigid boundary, Eq. (8) is replaced by

$$\epsilon = \frac{c_\mu^{3/4} k_p^{3/2}}{\kappa \delta} \quad , \quad (9)$$

where  $k_p$  is the value of  $k$  in the computation cell and  $\delta$  is the distance from the wall to the center of the computation cell. The wall shear stress in the momentum equations is obtained from

$$(\tau/\rho)_w = \frac{\kappa c_\mu^{1/4} k_p^{1/2}}{\ln \left( \frac{E \delta c_\mu^{1/4} k_p^{1/2}}{v_L} \right)} U_p \quad , \quad (10)$$

where  $U_p$  is the tangential velocity component in the computation cell adjacent to the wall.

The original Launder-Spalding model<sup>5</sup> did not account for modifications of the turbulence field due to buoyancy effects. Thus for our purposes Eqs. (7) and (8) must be modified as follows:

$$\frac{\partial k}{\partial t} + U_i \frac{\partial k}{\partial x_i} = \frac{1}{\rho} \frac{\partial}{\partial x_i} \left( \frac{\mu_T}{\sigma_k} \frac{\partial k}{\partial x_i} \right) + \frac{\mu_T}{\rho} \left[ \left( \frac{\partial U_i}{\partial x_j} + \frac{\partial U_j}{\partial x_i} \right) \frac{\partial U_i}{\partial x_j} + \alpha g_i \frac{\partial T}{\partial x_i} \right] - \epsilon \quad . \quad (11)$$

$$\frac{\partial \epsilon}{\partial t} + U_i \frac{\partial \epsilon}{\partial x_i} = \frac{1}{\rho} \frac{\partial}{\partial x_i} \left( \frac{\mu_T}{\sigma_\epsilon} \frac{\partial \epsilon}{\partial x_i} \right) + \frac{c_1 \mu_T}{\rho} \frac{\epsilon}{k} \left[ \left( \frac{\partial U_i}{\partial x_j} + \frac{\partial U_j}{\partial x_i} \right) \frac{\partial U_i}{\partial x_j} + \alpha g_i \frac{\partial T}{\partial x_i} \right] - c_2 \frac{\epsilon^2}{k} \quad . \quad (12)$$

The wall heat flux is given by

$$\dot{q}_w = \frac{(T_p - T_w) c_p \rho_c^{1/4} \mu_p^{1/2}}{\frac{\sigma_h}{\kappa} \ln \left( \frac{E \delta_c^{1/4} \mu_p^{1/2}}{v_L} \right) + \sigma_h \left( \frac{\pi/4}{\sin \pi/4} \right) \left( \frac{B}{\kappa} \right)^{1/2} \left( \frac{\sigma_{h,\ell}}{\sigma_h} - 1 \right) \left( \frac{\sigma_h}{\sigma_{h,\ell}} \right)^{1/4}}, \quad (13)$$

where  $T_p$  is the fluid temperature in the computation cell adjacent to the wall. The wall edge temperature  $T_w$  is replaced in Eq. (13) by the temperature of the metal at depth using the formulation for the heat flux from the wall to the fluid,

$$\dot{q}_w = \frac{k_m (T_w - T_m)}{\delta_m}, \quad (14)$$

where  $T_m$  is the metal temperature at a depth  $\delta_m$  from the wall edge and  $k_m$  is the thermal conductivity of the metal. Near the wall edge,  $k_m$  is determined from a thickness-weighted average of the clad and base-metal conductivities.

The various constants appearing in Eqs. (9)-(13) have the values shown in Table II. The volume coefficient of expansion  $\alpha$  and the laminar kinematic viscosity  $v_L$  of the fluid are functions of temperature, and for the applications made to date, the specific heat of the fluid has been taken to be  $4.285 \times 10^7$  erg/gm $\cdot$ °C (constant).

In a combined experimental-computational study of turbulent mixing in thermally stratified shear flows, P. L. Violette<sup>6</sup> found that, for Froude numbers of about 1.0 or less, the turbulent mixing of the different temperature layers is almost completely suppressed. He also found that this phenomenon could be accurately simulated with the turbulence model of Launder and Spalding<sup>5</sup> if the buoyancy creation term in the modified  $\epsilon$  equation, Eq. (12), was set to zero. Since this term leads to a suppression of turbulent energy in stably stratified flow, its inclusion in the  $k$  equation but not the  $\epsilon$  equation leads to an exaggerated

TABLE II

CONSTANTS FOR THE  $k$ - $\epsilon$  WALL FUNCTIONS

$\kappa$	E	$\sigma_h$	$\sigma_{h,\ell}$	B
0.4	9.0	1.0	6.7	26.0

suppression of turbulence that agrees well with data for Froude numbers less than 1.0. Since this is the range of Froude numbers of the Creare experiments and the reactor flows, we have set the buoyancy-creation term in Eq. (12) to zero for stratified flow in the cold leg pipe.

The three-equation ( $k-\epsilon-T'^2$ ) turbulence model<sup>3,4</sup> is usually written in steady-state form but we have assumed that the same model applies for transient calculations. For a two-dimensional planar buoyant jet, these equations are

$$\frac{\partial k}{\partial t} + U_i \frac{\partial k}{\partial x_i} = \frac{\partial}{\partial x_i} \left( c_k \frac{\overline{kv^2}}{\epsilon} \frac{\partial k}{\partial x_i} \right) - \overline{uv} \frac{\partial U_i}{\partial x_j} - \alpha_{g_i} \overline{uT'} - \epsilon, \quad (15)$$

$$\frac{\partial \epsilon}{\partial t} + U_i \frac{\partial \epsilon}{\partial x_i} = \frac{\partial}{\partial x_i} \left( c_\epsilon \frac{\overline{kv^2}}{\epsilon} \frac{\partial \epsilon}{\partial x_i} \right) + c_{\epsilon 1} \frac{\epsilon}{k} \left( -\overline{uv} \frac{\partial U_i}{\partial x_j} - \alpha_{g_i} \overline{uT'} \right) - c_{\epsilon 2} \frac{\epsilon^2}{k}, \quad \text{and} \quad (16)$$

$$\frac{\partial \overline{T'^2}}{\partial t} + U_i \frac{\partial \overline{T'^2}}{\partial x_i} = \frac{\partial}{\partial x_i} \left( c_T \frac{k^2}{\epsilon} \frac{\partial \overline{T'^2}}{\partial x_i} \right) - 2\overline{vT'} \frac{\partial T}{\partial y} - c_{T1} \frac{\overline{\epsilon T'^2}}{k}, \quad (17)$$

where the overbarred terms are appropriate averages of products of fluctuating quantities. In the steady-state case the appropriate averaging of these quantities would be a time-average, while in the unsteady case an ensemble-averaging procedure would be more appropriate. In this study we assume that the correlations obtained in the time-averaging process are equivalent to those that would be obtained as a result of an ensemble-averaging process. These correlations are

$$\overline{uv} = \frac{1 - c_0}{c_1} \frac{\overline{v^2}}{k} \left[ 1 - \frac{1}{c_h} \frac{k}{\epsilon} \alpha_g (\partial T / \partial y) / (\partial U / \partial y) \right] \frac{k^2}{\epsilon} \frac{\partial U}{\partial y}, \quad (18)$$

$$\overline{v^2} = c_2 k, \quad (19)$$

$$\overline{vT'} = \frac{1}{c_h} \frac{\overline{v^2}}{k} \frac{k^2}{\epsilon} \frac{\partial T}{\partial y}, \quad \text{and} \quad (20)$$

$$\overline{uT'} = \frac{1}{c_h} \frac{k}{\epsilon} \left[ -\overline{uv} \frac{\partial T}{\partial y} - \overline{vT'} (1 - c_{hl}) \frac{\partial U}{\partial y} - (1 - c_{hl}) \overline{\alpha g T'^2} \right], \quad (21)$$

where we have chosen for illustration the particular case where  $x$  and  $u$  are parallel to the jet axis and  $y$  and  $v$  are normal to that axis in the mixing plane. For these same conditions the momentum and temperature diffusion terms in Eqs. (1) and (5) are modified by Chen and Rodi<sup>3</sup> as follows:

$$\text{Eq. (1): } \frac{1}{\rho} \mu_T \frac{\partial U}{\partial y} \rightarrow -\overline{uv}, \quad (22)$$

$$\text{Eq. (5): } \frac{1}{\rho} \sigma_T \frac{\partial T}{\partial y} \rightarrow -\overline{vT'}. \quad (23)$$

Similar descriptions apply for other orientations. The values of the coefficients appearing in Eqs. (15)-(21) are presented in Table III.

This buoyant-jet turbulence model has been developed for flows at a distance from confining walls, so a method for treating the interaction with walls is not included in the model. In these calculations, where it is necessary to account for the effect of walls on fluid drag and heat transfer, the boundary treatment that is used in the two-equation turbulence model [Eqs. (9), (10), and (13)] is also used in the buoyant-jet model.

In spite of the fact that the buoyant-jet turbulence model was developed for much simpler flow conditions than those that exist in the neighborhood of the HPI inlet or the downcomer, the use of this model in those regions results in much better agreement with the Creare data than is obtained when the two-equation turbulence model is used throughout. The reason for this is that the buoyant-jet model provides better mixing of the fluid in the jet with the entrained ambient fluid. This increased mixing becomes apparent when one compares corresponding

TABLE III

THE COEFFICIENTS OF THE  $k-\epsilon-T'^2$  MODEL

$c_0$	$c_1$	$c_2$	$c_\epsilon$	$c_{\epsilon 1}$	$c_{\epsilon 2}$	$c_k$	$c_T$	$c_{T1}$	$c_h$	$c_{hl}$
0.55	2.2	0.53	0.15	1.43	1.92	0.225	0.13	1.25	3.2	0.5

terms from the momentum, thermal energy, and turbulence equations using the two models. A quantitative comparison of the affected terms is presented in Appendix A.

### III. THE NUMERICAL MODEL

The SOLA-PTS code follows the Marker and Cell code<sup>7</sup> convention in which velocity components are located at cell faces and all other dependent variables are located at cell centers. A term  $q_{ijk}^n$  refers to a quantity  $q(x,y,z,t)$  at time level  $n\delta t$  and at the center of the  $i$ th cell in the  $x$ -direction, the  $j$ th cell in the  $y$ -direction, and the  $k$ th cell in the  $z$ -direction. The velocity component  $U_{i+\frac{1}{2}jk}^n$  is located at the boundary between cell  $(ijk)$  and cell  $(i+1jk)$ . When quantities are required at points other than their normal location, an interpolation formula is used.

The momentum (and all other transport) equations are solved in several steps, which will be described in detail below. In the first step the equations are updated explicitly using a centered-difference advection formulation. Since this formulation is numerically unstable, we modify the result of the first step by the addition of Tensor Viscosity<sup>8</sup> terms to stabilize the solution and make it second-order accurate. In the third step we apply the FRAM procedure,<sup>9</sup> which compares the result of the first two steps with what we call the Lagrangian values for the 6 surrounding computation cells. The Lagrangian value is the value obtained in the first step except that the advection terms are not included. If the result of the first two steps is an extremum relative to the surrounding Lagrangian values, then we replace the second-order solution for the quantity at that location with a first-order solution using donor-cell differencing.

The velocity components must be further modified by solving the continuity equation, Eq. (4), to determine the updated pressure field, which is then used to correct the result of the explicit solution so that the advanced-time pressure and velocity fields are consistent. A state-of-the-art iteration procedure known as the Conjugate Residual method<sup>10</sup> is used with a preconditioning algorithm to collapse the eigenvalues of the coefficient matrix into a narrow band for faster convergence. The use of this procedure allows us to rapidly converge to an accurate solution for the pressure field.

To illustrate the finite-difference formulation for the momentum equations, we will write the equation for  $U_{i+\frac{1}{2}jk}$ . The equations for  $V_{ij+\frac{1}{2}k}$  and  $W_{ijk+\frac{1}{2}}$  are completely analogous.

A. The Momentum Equations

The Lagrangian equation is written

$$\begin{aligned}
 \text{ULAG}_{i+\frac{1}{2}jk} = & U_{i+\frac{1}{2}jk}^n + \delta t \left\{ \frac{1}{\rho} \left( \frac{p_{ijk}^n - p_{i+1jk}^n}{\delta x_{i+\frac{1}{2}}} \right) \right. \\
 & + g_x \left\{ 1 - \alpha \left[ \frac{1}{2} \left( \frac{\delta x_{i+1} T_{ijk}^n + \delta x_i T_{i+1jk}^n}{\delta x_{i+\frac{1}{2}}} \right) - T_o \right] \right\} \\
 & + \frac{2}{\rho} \left[ \mu_{T_{i+1jk}}^n \left( \frac{U_{i+3/2jk}^n - U_{i+\frac{1}{2}jk}^n}{\delta x_{i+1}} \right) - \mu_{T_{ijk}}^n \left( \frac{U_{i+\frac{1}{2}jk}^n - U_{i-\frac{1}{2}jk}^n}{\delta x_i} \right) \right] / \delta x_{i+\frac{1}{2}} \\
 & + \frac{1}{\rho} [(DUDF - DUDA) / \delta y_s_j + (DUDT - DUDB) / \delta z_s_k] \\
 & + \frac{1}{\rho} \left[ \mu_{T_{i+\frac{1}{2}j+\frac{1}{2}k}}^n \left( \frac{V_{i+1j+\frac{1}{2}k}^n - V_{ij+\frac{1}{2}k}^n}{\delta x_{i+\frac{1}{2}}} \right) - \mu_{T_{i+\frac{1}{2}j-\frac{1}{2}k}}^n \left( \frac{V_{i+1j-\frac{1}{2}k}^n - V_{ij-\frac{1}{2}k}^n}{\delta x_{i+\frac{1}{2}}} \right) \right] / \delta y_j \\
 & + \frac{1}{\rho} \left[ \mu_{T_{i+\frac{1}{2}jk+\frac{1}{2}}}^n \left( \frac{W_{i+1jk+\frac{1}{2}}^n - W_{ijk+\frac{1}{2}}^n}{\delta x_{i+\frac{1}{2}}} \right) - \mu_{T_{i+\frac{1}{2}jk-\frac{1}{2}}}^n \left( \frac{W_{i+1jk-\frac{1}{2}}^n - W_{ijk-\frac{1}{2}}^n}{\delta x_{i+\frac{1}{2}}} \right) \right] / \delta z_k \left. \right\}, \quad (24)
 \end{aligned}$$

where the volumetric coefficient of expansion is a function of temperature,

$$\alpha(T) = \begin{cases} 2.0661 \times 10^{-4} + [9.653 \times 10^{-6} - 7.155 \times 10^{-8} (T_{ijk}^n - 303)](T_{ijk}^n - 293), \\ \quad T_{ijk}^n < 313 \text{ K} \\ 7.4066 \times 10^{-6} T_{ijk}^n - 1.9412 \times 10^{-3}, \quad 313 \leq T_{ijk}^n \leq 373 \text{ K} \\ 4.333 \times 10^{-6} T_{ijk}^n - 8.663 \times 10^{-4}, \quad 373 \text{ K} < T_{ijk}^n \end{cases} \quad (25)$$



The turbulent diffusion coefficient  $\mu_T$  will have different forms depending on whether the Launder-Spalding<sup>5</sup> or Chen and Rodi<sup>3,4</sup> model is being used in that cell. See Appendix A for a description and comparison of these forms. The formulations DUDF, DUDA, DUDT, and DUDB can represent the effects of wall shear or internal viscous shear forces. For example, in a cell adjacent to a rigid wall<sup>5</sup> in the increasing y-direction,

$$DUDF = \frac{P \left( c_{\mu}^{\frac{1}{2}} k_{i+\frac{1}{2}jk}^n \right)^{\frac{1}{2}} U_{i+\frac{1}{2}jk}^n}{\frac{1}{\kappa} \ln \left[ E \frac{\delta y_j}{2} \left( c_{\mu}^{\frac{1}{2}} k_{i+\frac{1}{2}jk}^n \right)^{\frac{1}{2}} / v_{L,i+\frac{1}{2}jk}^n \right]}, \quad (26)$$

where P is the ratio of perimeters of a round pipe and a square duct of the same cross-sectional area,<sup>\*</sup>

$$P = \begin{cases} \sqrt{\pi/4}, & \text{in the cold leg} \\ 1, & \text{otherwise} \end{cases} \quad (27)$$

If the cell in question is not adjacent to a rigid wall,

$$DUDF = \frac{\mu_T^n_{i+\frac{1}{2}j+\frac{1}{2}k}}{\rho} \left( \frac{U_{i+\frac{1}{2}j+lk}^n - U_{i+\frac{1}{2}jk}^n}{\delta y_{j+\frac{1}{2}}} \right) \quad (28)$$

DUDA, DUDT, and DUDB have formulations similar to Eqs. (26) or (28) depending on the location of the cell relative to a rigid wall.

The laminar kinematic viscosity  $v_L$  in Eq. (26) is a function of temperature,

\*The SOLA-PTS code represents circular cross-section pipes as square ducts.

$$v_{L_{ijk}} = \begin{cases} 1.3326 \times 10^{-1} + 5.5996 \times 10^{-7} (T_{ijk}^n)^2 - 5.7633 \times 10^{-4} T_{ijk}^n, \\ T_{ijk}^n \leq 323 \text{ K} \\ 6.0758 \times 10^{-2} + 3.2005 \times 10^{-7} (T_{ijk}^n)^2 - 2.7436 \times 10^{-4} T_{ijk}^n, \\ 323 < T_{ijk}^n < 423 \text{ K} \\ 1.3513 \times 10^{-2} + 4.0273 \times 10^{-8} (T_{ijk}^n)^2 - 4.4326 \times 10^{-5} T_{ijk}^n, \\ 423 \text{ K} \leq T_{ijk}^n \end{cases} \quad (29)$$

The equation for ULAG, Eq. (24), must be modified to include the advection terms. Thus,

$$\tilde{U}_{i+\frac{1}{2}jk} = \text{ULAG}_{i+\frac{1}{2}jk} - \delta t \text{UFLX}_{i+\frac{1}{2}jk}, \quad (30)$$

where

$$\text{UFLX}_{i+\frac{1}{2}jk} = (\text{FUX} + \text{FUY} + \text{FUZ})_{i+\frac{1}{2}jk}, \quad (31)$$

$$\text{FUX}_{i+\frac{1}{2}jk} = \frac{1}{2} U_{i+\frac{1}{2}jk}^n \left[ \delta x_i \left( \frac{U_{i+3/2jk}^n - U_{i+\frac{1}{2}jk}^n}{\delta x_{i+1}} \right) + \delta x_{i+1} \left( \frac{U_{i+\frac{1}{2}jk}^n - U_{i-\frac{1}{2}jk}^n}{\delta x_i} \right) \right] / \delta x_{i+\frac{1}{2}}, \quad (32)$$

$$\begin{aligned} \text{FUY}_{i+\frac{1}{2}jk} = \frac{1}{2} V_{i+\frac{1}{2}jk}^n \left[ \delta y_{j-\frac{1}{2}} \left( \frac{U_{i+\frac{1}{2}j+1k}^n - U_{i+\frac{1}{2}jk}^n}{\delta y_{j+\frac{1}{2}}} \right) \right. \\ \left. + \delta y_{j+\frac{1}{2}} \left( \frac{U_{i+\frac{1}{2}jk}^n - U_{i+\frac{1}{2}j-1k}^n}{\delta y_{j-\frac{1}{2}}} \right) \right] / \delta y_{j+\frac{1}{2}}, \text{ and} \end{aligned} \quad (33)$$

$$\begin{aligned}
FUZ_{i+\frac{1}{2}jk} &= \frac{1}{2} W_{i+\frac{1}{2}jk}^n \left[ \delta z_{k-\frac{1}{2}} \left( \frac{U_{i+\frac{1}{2}jk+1}^n - U_{i+\frac{1}{2}jk}^n}{\delta z_{k+\frac{1}{2}}} \right) \right. \\
&\quad \left. + \delta z_{k+\frac{1}{2}} \left( \frac{U_{i+\frac{1}{2}jk}^n - U_{i+\frac{1}{2}jk-1}^n}{\delta z_{k-\frac{1}{2}}} \right) \right] / \delta z s_k .
\end{aligned} \tag{34}$$

The quantities  $\delta y_{j\pm\frac{1}{2}}$ ,  $\delta z_{k\pm\frac{1}{2}}$ ,  $\delta y s_j$ , and  $\delta z s_k$  are defined

$$\delta y_{j\pm\frac{1}{2}} = \frac{1}{2} (\delta y_j + \delta y_{j\pm 1}) ,$$

$$\delta z_{k\pm\frac{1}{2}} = \frac{1}{2} (\delta z_k + \delta z_{k\pm 1}) ,$$

$$\delta y s_j = \frac{1}{4} (\delta y_{j+1} + 2\delta y_j + \delta y_{j-1}) , \text{ and}$$

$$\delta z s_k = \frac{1}{4} (\delta z_{k+1} + 2\delta z_k + \delta z_{k-1}) .$$

In some of the calculations that have been performed with SOLA-PTS, we have simulated the effect of a vertical bend in a cold leg pipe by assigning a nonzero value to  $g_y$ , where the  $y$ -direction is associated with the axis of the pipe. However, when we do this we do not modify the value of  $g_z$ , the normally vertical component of gravity. The reason for this is that, if we allow  $g_z$  to vary with  $y$ , this leads to an artificial creation of vorticity  $\nabla \times \underline{U}$  through a term  $\partial g_z / \partial y$ . The term  $\partial g_y / \partial y$ , on the other hand, does not contribute to  $\nabla \times \underline{U}$ .

The interpolation procedures used in Eqs. (32)-(34) as well as in Eq. (24) do not introduce any low-order truncation errors, so at this point the equations are second-order accurate in space and first-order accurate in time. We now introduce the Tensor Viscosity<sup>8</sup> correction to Eq. (30), which makes the solution second-order in time by removing the destabilizing truncation error associated with forward-time, centered-space differencing. As pointed out in Reference 8, this error results from the fact that Eq. (30) is not time centered, rather than from the space centering of the terms in Eqs. (32)-(34). The modified equation is

$$\bar{U}_{i+\frac{1}{2}jk} = \tilde{U}_{i+\frac{1}{2}jk} + \frac{1}{2} \delta t^2 (U_{i+\frac{1}{2}jk}^n \text{DUFUDX} + V_{i+\frac{1}{2}jk}^n \text{DUFUDY} + W_{i+\frac{1}{2}jk}^n \text{DUFUDZ}) , \quad (35)$$

where

$$\begin{aligned} \text{DUFUDX} = \frac{1}{2} \left[ \delta x_i \left( \frac{\text{UFLX}_{i+3/2jk} - \text{UFLX}_{i+\frac{1}{2}jk}}{\delta x_{i+1}} \right) \right. \\ \left. + \delta x_{i+1} \left( \frac{\text{UFLX}_{i+\frac{1}{2}jk} - \text{UFLX}_{i-\frac{1}{2}jk}}{\delta x_i} \right) \right] / \delta x_{i+\frac{1}{2}} , \end{aligned} \quad (36)$$

$$\begin{aligned} \text{DUFUDY} = \frac{1}{2} \left[ \delta y_{j-\frac{1}{2}} \left( \frac{\text{UFLX}_{i+\frac{1}{2}j+1k} - \text{UFLX}_{i+\frac{1}{2}jk}}{\delta y_{j+\frac{1}{2}}} \right) \right. \\ \left. + \delta y_{j+\frac{1}{2}} \left( \frac{\text{UFLX}_{i+\frac{1}{2}jk} - \text{UFLX}_{i+\frac{1}{2}j-1k}}{\delta y_{j-\frac{1}{2}}} \right) \right] / \delta y_j , \text{ and} \end{aligned} \quad (37)$$

$$\begin{aligned} \text{DUFUDZ} = \frac{1}{2} \left[ \delta z_{k-\frac{1}{2}} \left( \frac{\text{UFLX}_{i+\frac{1}{2}jk+1} - \text{UFLX}_{i+\frac{1}{2}jk}}{\delta z_{k+\frac{1}{2}}} \right) \right. \\ \left. + \delta z_{k+\frac{1}{2}} \left( \frac{\text{UFLX}_{i+\frac{1}{2}jk} - \text{UFLX}_{i+\frac{1}{2}jk-1}}{\delta z_{k-\frac{1}{2}}} \right) \right] / \delta z_k . \end{aligned} \quad (38)$$

The important advantage of using a second-order accurate equation, such as Eq. (35), is that very little numerical damping is added to the solution, so that the physical damping that results from turbulence interactions can play an important role in the solution. However, because of the very limited numerical damping of the solution, the calculations can suffer from numerical dispersion errors. These appear as local overshoots and undershoots (oscillations) in the numerical results. They are generally not a severe problem for the SOLA-PTS applications considered here, because of the large physical damping in these problems. Nevertheless, we guard against the growth of these errors by applying the FRAM procedure<sup>9</sup> to the solution of Eq. (35). This is done by comparing

$$\bar{U}_{i+\frac{1}{2}jk} : \text{Max, Min} (ULAG_{i-\frac{1}{2}jk}, ULAG_{i+3/2jk}, ULAG_{i+\frac{1}{2}j-1k}, ULAG_{i+\frac{1}{2}j+1k}, ULAG_{i+\frac{1}{2}jk-1}, ULAG_{i+\frac{1}{2}jk+1}) .$$

If this updated value of  $\bar{U}_{i+\frac{1}{2}jk}$  is greater than the maximum of these quantities, or less than their minimum, then the solution in Eq. (35) is replaced by

$$\bar{U}_{i+\frac{1}{2}jk} = ULAG_{i+\frac{1}{2}jk} - St(FUXDC + FUYDC + FUZDC) , \quad (39)$$

where

$$FUXDC = \begin{cases} U_{i+\frac{1}{2}jk}^n \left( \frac{U_{i+3/2jk}^n - U_{i+\frac{1}{2}jk}^n}{\delta x_{i+1}} \right), & \text{if } U_{i+\frac{1}{2}jk}^n < 0 \\ U_{i+\frac{1}{2}jk}^n \left( \frac{U_{i+\frac{1}{2}jk}^n - U_{i-\frac{1}{2}jk}^n}{\delta x_i} \right), & \text{if } U_{i+\frac{1}{2}jk}^n > 0 , \end{cases} \quad (40)$$

$$FUYDC = \begin{cases} V_{i+\frac{1}{2}jk}^n \left( \frac{U_{i+\frac{1}{2}j+1k}^n - U_{i+\frac{1}{2}jk}^n}{\delta y_{j+\frac{1}{2}}} \right), & \text{if } V_{i+\frac{1}{2}jk}^n < 0 \\ V_{i+\frac{1}{2}jk}^n \left( \frac{U_{i+\frac{1}{2}jk}^n - U_{i+\frac{1}{2}j-1k}^n}{\delta y_{j-\frac{1}{2}}} \right), & \text{if } V_{i+\frac{1}{2}jk}^n > 0 , \end{cases} \quad (41)$$

$$FUZDC = \begin{cases} W_{i+\frac{1}{2}jk}^n \left( \frac{U_{i+\frac{1}{2}jk+1}^n - U_{i+\frac{1}{2}jk}^n}{\delta z_{k+\frac{1}{2}}} \right), & \text{if } W_{i+\frac{1}{2}jk}^n < 0 \\ W_{i+\frac{1}{2}jk}^n \left( \frac{U_{i+\frac{1}{2}jk}^n - U_{i+\frac{1}{2}jk-1}^n}{\delta z_{k-\frac{1}{2}}} \right), & \text{if } W_{i+\frac{1}{2}jk}^n > 0 . \end{cases} \quad (42)$$

Equations (40)-(42) are known as donor-cell advection terms. Their use in Eq. (39) reduces the accuracy of that equation to first order. In the SOLA-PTS calculations of this study, this first-order solution is applied in about 1-2% of the computation cells at any particular time cycle.

The final step in the solution for the velocity field is to obtain the updated pressures by solving the continuity equation,

$$\underline{\nabla} \cdot \underline{U}^{n+1} = 0 \quad , \quad (43)$$

together with the momentum equation

$$\underline{U}^{n+1} = - \delta t \underline{\nabla} p^{n+1} + \underline{\tilde{U}} \quad . \quad (44)$$

This gives

$$\delta t \text{VOL}_{ijk} \underline{\nabla} \cdot \underline{\nabla} p^{n+1} = \text{VOL}_{ijk} \underline{\nabla} \cdot \underline{\tilde{U}} \quad , \quad (45)$$

where Eq. (45) has been multiplied by the cell volume  $\text{VOL}_{ijk} = \delta x_i \delta y_j \delta z_k$  to make it conservative (and therefore symmetric).

Reference 10 describes procedures for solving equations such as Eq. (45), which may be written in matrix form as

$$\underline{A} \underline{s} = \underline{h} \quad , \quad (46)$$

where the vector  $\underline{s}$  represents the unknown pressures  $p^{n+1}$  and the matrix A is symmetric. These Conjugate Gradient methods are a family of iteration procedures that attempt to minimize error functionals of the form

$$E_Y(\underline{\tilde{s}}) = (\underline{s} - \underline{\tilde{s}})^T \underline{A}^Y (\underline{s} - \underline{\tilde{s}}) \quad , \quad (47)$$

where  $\underline{\tilde{s}}$  is an approximate solution obtained by iteration and  $\underline{s}$  is the actual solution of Eq. (46). Each integer value of  $\gamma$  corresponds to a different member of the family of solution procedures. It can be shown that these Conjugate Gradient schemes are the optimum iteration procedures for whichever norm [Eq. (47)] that is chosen to test convergence. We choose to employ the Conjugate Residual method, which corresponds to  $\gamma = 2$ ,

$$E_2(\underline{\tilde{s}}) = (\underline{s} - \underline{\tilde{s}})^T \underline{A}^2 (\underline{s} - \underline{\tilde{s}}) = \underline{r}^T \underline{r} \quad , \quad (48)$$

where  $\underline{r}$  is the residual error,

$$\underline{r} = \underline{h} - A\underline{s} \quad (49)$$

This method was chosen because  $\underline{r}$  can be related to the velocity divergence field, which is what we wish to minimize most efficiently.

These iteration procedures can be made even more efficient if one preconditions the system of equations (46). We multiply this equation by  $Q^{-1}$ ,

$$Q^{-1}AQ^{-T}Q^T\underline{s} = Q^{-1}\underline{h} \quad (50)$$

where  $Q$  is an unspecified nonsingular matrix that makes the equation easier to solve.

Then Eq. (46) becomes

$$A'\underline{s}' = \underline{h}' \quad (51)$$

where

$$A' = Q^{-1}AQ^{-T} \quad (52a)$$

$$\underline{s}' = Q^T\underline{s} \quad (52b)$$

$$\underline{h}' = Q^{-1}\underline{h} \quad (52c)$$

and Eq. (51) is solved by the Conjugate Residual method as before. We choose  $Q$  so that  $A$  is well approximated by  $M = QQ^T$ , so

$$A'\underline{s}' \approx Q^{-1}QQ^TQ^{-T}\underline{s}' = \underline{s}' \quad (53)$$

Therefore, with this approximation the eigenvalues of  $A'$  are all close to unity so the iteration proceeds very rapidly. The matrix  $Q$  is obtained by an incomplete Cholesky decomposition.

The convergence of the pressure iteration is tested by comparing the maximum absolute value of the divergence of the velocity field with  $10^{-4}$ . When the iterations have converged, the velocity components are corrected by replacing the n-level pressure gradients with the pressure gradients obtained from the iterated solution.

### B. The Temperature Equation

As with the momentum equations, the temperature equation is solved in three steps, the Lagrangian equation and advection contribution are computed, followed by the Tensor Viscosity<sup>8</sup> contribution and the FRAM<sup>9</sup> testing. The Lagrangian equation is written

$$\begin{aligned} \text{TLAG}_{ijk} = T_{ijk}^n + \delta t \left[ (1 + \beta_x)(\text{STXR} - \text{STXL})/\delta x_{s_i} + (1 + \beta_y)(\text{STYF} - \text{STYA})/\delta y_{s_j} \right. \\ \left. + (1 + \beta_z)(\text{STZT} - \text{STZB})/\delta z_{s_k} \right], \end{aligned} \quad (54)$$

where the terms  $\beta_x$ ,  $\beta_y$ , and  $\beta_z$  account for augmented thermal diffusion in the fluid as indicated by the  $k-\epsilon-T'^2$  turbulence model.<sup>3,4</sup> When that model is being applied in a cell, the diffusion coefficient in a direction normal to the axis of a thermal plume will be increased by 84% (see Appendix A). For example, in the downcomer  $\beta_x = 0.84$ , while  $\beta_y$  and  $\beta_z$  are zero.

The terms STXR, STXL, STYF, STYA, STZT, and STZB can represent the effects of heat flux to a wall or an internal diffusive flux. In a cell adjacent to a wall in the increasing x-direction,<sup>5</sup> for example,

$$\text{STXR} = \frac{\left( c_{\mu}^{\frac{1}{2}} k_{ijk}^n \right)^{\frac{1}{2}} \left( T_{i+1jk}^n - T_{ijk}^n \right)}{\frac{\sigma_n}{\kappa} \ln \left[ E \frac{\delta x_i}{2} \left( c_{\mu}^{\frac{1}{2}} k_{ijk}^n \right)^{\frac{1}{2}} v_{L_{ijk}}^n \right] + \zeta + \rho c_{\rho_f} \frac{\delta x_i}{2} \left( c_{\mu}^{\frac{1}{2}} k_{ijk}^n \right)^{\frac{1}{2}} k_m}, \quad (55)$$

where  $\zeta$  represents the second term in the denominator in Eq. (13). Equation (55) results from combining Eqs. (13) and (14) in order to express the wall heat flux in terms of the wall temperature at depth,  $T_{i+1jk}^n$  in this case. The thermal conductivity of the metal is obtained by interpolating between the clad and base-metal values,



$$k_m = (h_c k_c + (\delta x_{i+1} - h_c) k_b) / \delta x_{i+1} , \quad (56)$$

where  $h_c$  is the thickness of the clad.

If the cell in question is not adjacent to a rigid wall,

$$STXR = \frac{\sigma_T^n}{\rho} \left( \frac{T_{i+1,jk}^n - T_{i,jk}^n}{\delta x_{i+\frac{1}{2}}} \right) , \quad (57)$$

in a fluid cell, or

$$STXR = \frac{k_m}{\rho_m c \rho_m} \left( \frac{T_{i+1,jk}^n - T_{i,jk}^n}{\delta x_{i+\frac{1}{2}}} \right) , \quad (58)$$

in a wall cell. In a wall cell adjacent to a fluid cell in the increasing  $x$ -direction, a formulation similar to Eq. (55) would be used for STXR, except that it would be multiplied by  $\rho_c / \rho_m c \rho_m$ . Similar expressions to these for STXR apply to the other thermal flux terms.

The SOLA-PTS applications discussed in this report employ adiabatic wall boundary conditions, so these wall-heat-flux formulations have not been used. Indeed, users of the SOLA-PTS code should be advised that important changes have been made in the code since the wall-heat-flux capability has last been exercised, and the effect of these changes has not been tested. Therefore, more than the usual care should be used when applying the wall-heat-flux procedure.

The thermal advection term is expressed

$$\begin{aligned} TFLX_{i,jk} = \frac{1}{2} \left\{ U_{i,jk}^{n+1} \left[ \delta x_{i-\frac{1}{2}} \left( \frac{T_{i+1,jk}^n - T_{i,jk}^n}{\delta x_{i+\frac{1}{2}}} \right) + \delta x_{i+\frac{1}{2}} \left( \frac{T_{i,jk}^n - T_{i-1,jk}^n}{\delta x_{i-\frac{1}{2}}} \right) \right] / \delta x_s_i \right. \\ \left. + V_{i,jk}^{n+1} \left[ \delta y_{j-\frac{1}{2}} \left( \frac{T_{i,j+1k}^n - T_{i,jk}^n}{\delta y_{j+\frac{1}{2}}} \right) + \delta y_{j+\frac{1}{2}} \left( \frac{T_{i,jk}^n - T_{i,j-1k}^n}{\delta y_{j-\frac{1}{2}}} \right) \right] / \delta y_s_j \right. \\ \left. + W_{i,jk}^{n+1} \left[ \delta z_{k-\frac{1}{2}} \left( \frac{T_{i,jk+1}^n - T_{i,jk}^n}{\delta z_{k+\frac{1}{2}}} \right) + \delta z_{k+\frac{1}{2}} \left( \frac{T_{i,jk}^n - T_{i,jk-1}^n}{\delta z_{k-\frac{1}{2}}} \right) \right] / \delta z_s_k \right\} , \quad (59) \end{aligned}$$

where  $U_{ijk}^{n+1}$ ,  $V_{ijk}^{n+1}$ , and  $W_{ijk}^{n+1}$  are averages of the cell boundary velocities.

Thus, after the first step of the solution for the temperature field,

$$\tilde{T}_{ijk} = \text{TLAG}_{ijk} - \delta t \text{TFLX}_{ijk} \quad (60)$$

In the second step we make the Tensor Viscosity correction to Eq. (60),

$$\bar{T}_{ijk} = \tilde{T}_{ijk} + \frac{1}{2} \delta t^2 (U_{ijk}^{n+1} \text{DUBTCX} + V_{ijk}^{n+1} \text{DVBT CY} + W_{ijk}^{n+1} \text{DWBTCZ}) \quad (61)$$

where

$$\text{DUBTCX} = \frac{1}{2} \left[ \delta x_{i-\frac{1}{2}} \left( \frac{\text{TFLX}_{i+1jk} - \text{TFLX}_{ijk}}{\delta x_{i+\frac{1}{2}}} \right) + \delta x_{i+\frac{1}{2}} \left( \frac{\text{TFLX}_{ijk} - \text{TFLX}_{i-1jk}}{\delta x_{i-\frac{1}{2}}} \right) \right] / \delta x_s_i \quad (62)$$

$$\text{DVBT CY} = \frac{1}{2} \left[ \delta y_{j-\frac{1}{2}} \left( \frac{\text{TFLX}_{ij+1k} - \text{TFLX}_{ijk}}{\delta y_{j+\frac{1}{2}}} \right) + \delta y_{j+\frac{1}{2}} \left( \frac{\text{TFLX}_{ijk} - \text{TFLX}_{ij-1k}}{\delta y_{j-\frac{1}{2}}} \right) \right] / \delta y_s_j \quad (63)$$

$$\text{DWBTCZ} = \frac{1}{2} \left[ \delta z_{k-\frac{1}{2}} \left( \frac{\text{TFLX}_{ijk+i} - \text{TFLX}_{ijk}}{\delta z_{k+\frac{1}{2}}} \right) + \delta z_{k+\frac{1}{2}} \left( \frac{\text{TFLX}_{ijk} - \text{TFLX}_{ijk-l}}{\delta z_{k-\frac{1}{2}}} \right) \right] / \delta z_s_k \quad (64)$$

Finally, in the third step we apply the FRAM procedure to determine whether the second-order solution will stand or whether it will be necessary to revert to the first-order donor-cell solution. We compare

$$\bar{T}_{ijk} : \text{Max, Min} (\text{TLAG}_{i+1jk}, \text{TLAG}_{i-1jk}, \text{TLAG}_{ij+1k}, \text{TLAG}_{ij-1k}, \text{TLAG}_{ijk+1}, \text{TLAG}_{ijk-1}).$$

If  $\bar{T}_{ijk}$  is greater than this maximum or less than this minimum, then the solution Eq. (61) is replaced by

$$\bar{T}_{ijk} = \text{TLAG}_{ijk} - \delta t (\text{FTXDC} + \text{FTYDC} + \text{FTZDC}) \quad (65)$$

where

$$FTXDC = U_{ijk}^{n+1} \times \begin{cases} \left( \frac{T_{i+1jk}^n - T_{ijk}^n}{\delta x_{i+\frac{1}{2}}} \right), & \text{if } U_{ijk}^{n+1} < 0 \\ \left( \frac{T_{ijk}^n - T_{i-1jk}^n}{\delta x_{i-\frac{1}{2}}} \right), & \text{if } U_{ijk}^{n+1} > 0 \end{cases} \quad (66)$$

$$FTYDC = V_{ijk}^{n+1} \times \begin{cases} \left( \frac{T_{ij+1k}^n - T_{ijk}^n}{\delta y_{j+\frac{1}{2}}} \right), & \text{if } V_{ijk}^{n+1} < 0 \\ \left( \frac{T_{ijk}^n - T_{ij-1k}^n}{\delta y_{j-\frac{1}{2}}} \right), & \text{if } V_{ijk}^{n+1} > 0 \end{cases}, \text{ and} \quad (67)$$

$$FTZDC = W_{ijk}^{n+1} \times \begin{cases} \left( \frac{T_{ijk+1}^n - T_{ijk}^n}{\delta z_{k+\frac{1}{2}}} \right), & \text{if } W_{ijk}^{n+1} < 0 \\ \left( \frac{T_{ijk}^n - T_{ijk-1}^n}{\delta z_{k-\frac{1}{2}}} \right), & \text{if } W_{ijk}^{n+1} > 0 \end{cases} \quad (68)$$

As indicated with the momentum equations, it was only necessary to use the first-order solution Eq. (65) in about 1-2% of the computation cells at any particular time cycle.

The procedure described above for making the Tensor Viscosity<sup>8</sup> and FRAM<sup>9</sup> adjustments to the temperature equations also applies to the turbulence equations to be described below. Therefore we omit the description of these procedures for those equations.

### C. The Turbulence Equations

In SOLA-PTS the Launder-Spalding  $k-\epsilon$  model<sup>5</sup> of turbulence is used in the cold leg pipe except in the vicinity of the HPI inlet, while the Chen and Rodi  $k-\epsilon-T'^2$  model<sup>3,4</sup> is used near the HPI inlet and in the downcomer and core. The  $k-\epsilon-T'^2$  model provides enhanced mixing in the neighborhood of jets and plumes.

In the cold leg we use this model in the planes that include the HPI inlet cells and in two planes upstream and two downstream of these inlet planes. This provides good shear and buoyancy mixing in regions adjacent to the inlet cells without extending the  $k-\epsilon-T'^2$  model to stratified-flow regions of the cold-leg pipe where it would not be an appropriate model.

1. The  $\epsilon$  Equation. The Lagrangian equation for  $\epsilon$  is complicated, not only by the fact that there are many contributing terms, but also because of the modeling differences between the  $k-\epsilon$  scheme<sup>5</sup> and  $k-\epsilon-T'^2$  scheme.<sup>3,4</sup> Therefore, we will develop the various contributions to the Lagrangian equation before writing the full equation.

The shear-creation terms,

$$\frac{\mu_T}{\rho} \left( \frac{\partial U_\ell}{\partial x_m} + \frac{\partial U_m}{\partial x_\ell} \right) \frac{\partial U_\ell}{\partial x_m}, \quad (69)$$

are common to the  $k$  and  $\epsilon$  equations, so these terms are saved in a temporary array,

$$\begin{aligned} \text{TEMP}_{ijk} = & \frac{\mu_T}{\rho} \sum_{i,j,k}^n [ (PUPX + PUPX)PUPX + (PUPY + PVPX)PUPY + (PUPZ + PWPX)PUPZ \\ & + (PVPX + PUPY)PVPX + (PVPY + PVPY)PVPY + (PVPZ + PWPY)PVPZ \\ & + (PWPX + PUPZ)PWPX + (PWPY + PVPZ)PWPY + (PWPZ + PWPZ)PWPZ ]_{ijk}, \end{aligned} \quad (70)$$

where PUPX, PUPY, etc., are the various shear terms in Eq. (69). For example,

$$PWPX_{ijk} = \frac{1}{2} (\delta x_{i-\frac{1}{2}} DWDX_{i+\frac{1}{2}jk} + \delta x_{i+\frac{1}{2}} DWDX_{i-\frac{1}{2}jk}) / \delta x_{s_i}, \quad (71)$$

and the DWDX terms can represent wall shear or internal fluid shear. In a cell adjacent to a rigid wall in the increasing  $x$ -direction,

$$DWDX_{i+\frac{1}{2}jk} = \frac{P \left( c_{\frac{1}{2}}^{\frac{1}{2}} k_{ijk}^n \right)^{\frac{1}{2}} W_{ijk}^{n+1}}{\frac{1}{\kappa} \ln \left[ E \frac{\delta x_i}{2} \left( c_{\frac{1}{2}}^{\frac{1}{2}} k_{ijk}^n \right)^{\frac{1}{2}} / v_{L_{ijk}}^n \right] \mu_{T_{ijk}}^n / \rho}, \quad (72)$$

while in a cell away from rigid walls,

$$DWDX_{i+\frac{1}{2}jk} = (W_{i+1jk}^{n+1} - W_{ijk}^{n+1}) / \delta x_{i+\frac{1}{2}}. \quad (73)$$

If the computation cell is one in which the  $k-\epsilon-T^2$  turbulence model<sup>3,4</sup> is being applied, then Eq. (69) must be modified further. For example, to account for turbulent vertical buoyant jets in the downcomer, where  $z$  and  $W$  are parallel to the jet axis and  $x$  and  $U$  are normal to that axis, the term  $\frac{\mu_T}{\rho} \left( \frac{\partial W}{\partial x} \right)^2$  is replaced by

$$- \frac{w}{w} \frac{\partial W}{\partial x} = \frac{1 - c_0}{c_1} c_2 \left[ 1 - \frac{1}{c_h} \frac{k}{\epsilon} \alpha_{g_z} (\partial T / \partial x) / (\partial W / \partial x) \right] \frac{k^2}{\epsilon} \left( \frac{\partial W}{\partial x} \right)^2 \quad (74)$$

$$= .1084 \left[ 1 - \frac{k_{ijk}^n}{3.2 \epsilon_{ijk}^n} \alpha_{g_z} \frac{DTDX_{ijk}}{PWPX_{ijk}} \right] \frac{(k_{ijk}^n)^2}{\epsilon_{ijk}^n} (PWPX_{ijk})^2, \quad (75)$$

where

$$DTDX_{ijk} = \frac{1}{2} \left[ \delta x_{i-\frac{1}{2}} \left( \frac{T_{i+1jk}^{n+1} - T_{ijk}^{n+1}}{\delta x_{i+\frac{1}{2}}} \right) + \delta x_{i+\frac{1}{2}} \left( \frac{T_{ijk}^{n+1} - T_{i-1jk}^{n+1}}{\delta x_{i-\frac{1}{2}}} \right) \right] / \delta x_{si} \quad (76)$$

Likewise, in the HPI injection region the term  $\frac{\mu_T}{\rho} \left( \frac{\partial W}{\partial y} \right)^2$  is replaced by the analogous representation for  $- \frac{w}{w} \frac{\partial W}{\partial y}$ .

The shear-creation terms [Eq. (69)] combine with the buoyancy-creation terms in the same manner in the  $k$  and  $\epsilon$  equations [see Eqs. (11) and (12)]. Thus the temporary array [Eq. (70)] is modified to include these buoyancy terms,

$$\text{TEMP}_{ijk} = \text{TEMP}_{ijk} + \frac{\mu_T^n}{\rho} \alpha (DTDX_{ijk} g_x + DTDY_{ijk} g_y + DTDZ_{ijk} g_z) \quad (77)$$

As with the shear-creation terms, the buoyancy-creation terms must be modified if the computation cell is one in which the  $k-\epsilon-T'^2$  turbulence model<sup>3,4</sup> is being applied. Again considering the turbulent vertical buoyant jet in the downcomer, this requires replacing the term  $\frac{\mu_T}{\rho} \alpha g_z \frac{\partial T}{\partial z}$  from Eqs. (11) and (12) by the term  $-\alpha g_z \overline{wT'}$  from Eqs. (15) and (16). The turbulent correlation  $\overline{wT'}$  is given by Eq. (21) with the appropriate shift in the coordinate direction. The approximations for the partial derivatives are the same as those used in Eq. (74) and will not be repeated here. A similar modification of the buoyancy-creation terms is made in the HPI region. Notice that it is only through the buoyancy-creation terms that the  $T'^2$  part of the  $k-\epsilon-T'^2$  model is effective. In buoyant-jet regions the  $T'^2$  contribution to Eq. (21) is often dominant.

In stably stratified thermal regions, the buoyancy "creation" terms actually reduce  $k$  and  $\epsilon$ . We have already mentioned the fact that in those regions of the cold leg pipe away from the HPI inlet, we set the buoyancy-creation term to zero in the  $\epsilon$  equation but not in the  $k$  equation because experimental data of Reference 6 are best predicted for this modeling of the  $k-\epsilon$  approach. We have also found in our comparisons with experimental data that it is best to limit the negative contributions of the buoyancy-creation terms in stably stratified regions to be no greater in magnitude than the positive shear-creation terms.

We now turn our attention to the remaining terms in the  $\epsilon$  equation. The turbulent diffusion of  $\epsilon$  is given by

$$\begin{aligned} \text{DIFF} = \frac{1}{\rho \sigma_\epsilon} & \left\{ \left[ \mu_{T_{i+\frac{1}{2}jk}}^n \left( \frac{\epsilon_{i+1jk}^n - \epsilon_{ijk}^n}{\delta x_{i+\frac{1}{2}}} \right) - \mu_{T_{i-\frac{1}{2}jk}}^n \left( \frac{\epsilon_{ijk}^n - \epsilon_{i-1jk}^n}{\delta x_{i-\frac{1}{2}}} \right) \right] / \delta x_{s_i} \right. \\ & + \left[ \mu_{T_{ij+\frac{1}{2}k}}^n \left( \frac{\epsilon_{ij+1k}^n - \epsilon_{ijk}^n}{\delta y_{j+\frac{1}{2}}} \right) - \mu_{T_{ij-\frac{1}{2}k}}^n \left( \frac{\epsilon_{ijk}^n - \epsilon_{ij-1k}^n}{\delta y_{j-\frac{1}{2}}} \right) \right] / \delta y_{s_j} \\ & \left. + \left[ \mu_{T_{ijk+\frac{1}{2}}}^n \left( \frac{\epsilon_{ijk+1}^n - \epsilon_{ijk}^n}{\delta z_{k+\frac{1}{2}}} \right) - \mu_{T_{ijk-\frac{1}{2}}}^n \left( \frac{\epsilon_{ijk}^n - \epsilon_{ijk-1}^n}{\delta z_{k-\frac{1}{2}}} \right) \right] / \delta z_{s_k} \right\} \quad (78) \end{aligned}$$

The values of the turbulent viscosity coefficients at cell boundaries are obtained by interpolation, e.g.,

$$\mu_{T_{i+\frac{1}{2}jk}}^n = \frac{1}{2} \left( \delta x_{i+1} \mu_{T_{ijk}}^n + \delta x_i \mu_{T_{i+1jk}}^n \right) / \delta x_{i+\frac{1}{2}} \quad (79)$$

If the computation cell is one in which the  $k-\epsilon-T'^2$  turbulence model<sup>3,4</sup> is being applied, then Eq. (78) is multiplied by the factor 1.15 (see Appendix A). We also include a laminar diffusion expression in the  $\epsilon$  (and  $k$ ) equation; it is only effective in regions of low-intensity turbulence. This laminar expression is similar to Eq. (78) except that the term  $\sigma_\epsilon$  is deleted and the diffusion coefficients are the constant laminar values.

The creation and decay terms in Eq. (12) [and also Eq. (16), see Appendix A] include the quantity  $\epsilon$  as one of their factors. We can make use of this fact to enhance the stability of the  $\epsilon$  equation by writing this  $\epsilon$  factor in time-advanced form and solving the  $\epsilon$  equation semi-implicitly. However, stability is only enhanced if the sum of the creation and the decay terms is negative. Thus we only apply the implicit procedure in this case. We define

$$c4 = (c_1 \text{TEMP}_{ijk} - c_2 \epsilon_{ijk}^n) / k_{ijk}^n \quad (80)$$

$$\theta = \begin{cases} 0, & \text{if } c4 > 0 \\ 1, & \text{if } c4 < 0 \end{cases} \quad (81)$$

$$\text{Then } \epsilon_{LAG}_{ijk} = \{ \epsilon_{ijk}^n [1 + (1 - \theta)\delta t c4] + \delta t \text{DIFF} \} / (1 - \theta \delta t c4) \quad (82)$$

where DIFF includes the laminar and turbulent diffusion contributions.

The advective flux term  $\epsilon_{FLX}_{ijk}$  is formed exactly like  $T_{FLX}_{ijk}$  [Eq. (59)]. Likewise the Tensor Viscosity and FRAM corrections to the  $\epsilon$  equation,

$$\tilde{\epsilon}_{ijk} = \epsilon_{LAG}_{ijk} - \delta t \epsilon_{FLX}_{ijk} / (1 - \theta \delta t c4) \quad (83)$$

follow the same pattern used for the temperature equation.

2. The k Equation. The solution for the turbulence kinetic energy equation is similar to that of the energy dissipation rate equation. We have already pointed out the common creation terms and that these are saved in temporary storage to be used in the solution for  $k_{ijk}^{n+1}$ . Analogous diffusion terms are also used, with  $\sigma_k$  replacing  $\sigma_\epsilon$  in Eq. (78). However, in a computation cell in which the  $k-\epsilon-T'^2$  turbulence model<sup>3,4</sup> is used, the resulting diffusion term is multiplied by the factor 1.32 (see Appendix A). A laminar diffusion expression is also included in the total diffusive contribution to  $k_{ijk}$ .

As with the  $\epsilon$  equation, we use a semi-implicit formulation for the solution to the k equation, in this case by using Eq. (6) to express the dissipation rate in terms of k. This has the added advantage of solving the k and  $\epsilon$  equations at the same time level since the time-advanced value for  $\epsilon$  is not used in the k equation. That equation is then written

$$kLAG_{ijk} = [k_{ijk}^n + \delta t(DIFF + TEMP_{ijk})] / (1 + \delta t c_{\mu} \rho k_{ijk}^n / \nu_{T_{ijk}}^n), \quad (84)$$

and with the advection terms,

$$\tilde{k}_{ijk} = kLAG_{ijk} - \delta t k FLX_{ijk} / (1 + \delta t c_{\mu} \rho k_{ijk}^n / \nu_{T_{ijk}}^n). \quad (85)$$

The changes in  $\epsilon_{ijk}$ , Eq. (83), and  $k_{ijk}$ , Eq. (85), are limited to 25% of their magnitudes during any time cycle as a means of stabilizing these equations. The same Tensor Viscosity<sup>8</sup> and FRAM<sup>9</sup> procedures as used for the temperature field are applied here.

3. The  $T'^2$  Equation. The  $T'^2$  equations are similar in form to the temperature equations, Eqs. (54), (57), and (59-68), except for the addition of production and decay terms. We write the Lagrangian equation for  $T'^2$

$$\begin{aligned} TPFLAG_{ijk} = & TPS_{ijk}^n + \delta t [(STXR - STXL) / \delta x s_i + (STYF - STYA) / \delta y s_j \\ & + (STZT - STZB) / \delta z s_k + PROD - DECAY] \quad (86) \end{aligned}$$

The STXR, STXL, STYF, STYA, STZT, and STZB terms are diffusive fluxes as in Eq. (54), but unlike that equation these terms are zero at rigid walls since we do



not account for the flux of  $\overline{T'^2}$  into walls. These diffusive flux terms are also zero at the boundary between regions where the  $k-\epsilon$  model<sup>5</sup> and  $k-\epsilon-\overline{T'^2}$  model<sup>3,4</sup> are used. [Equation (86) and those following are only solved in regions where the  $k-\epsilon-\overline{T'^2}$  model is applied, of course.]

This form works well in the cold leg and the downcomer regions but in one case has led to excessive diffusion in the lower plenum. The coefficient  $\sigma_T$  is large in the lower plenum region because of the turbulent shear creation that results from fluid flowing under the core-barrel wall and then rising in the core. When these large values of  $\sigma_T$  are increased further by the factor 1.44 in Eq. (87), they have in the one case mentioned caused a diffusive instability in the  $\overline{T'^2}$  equation that grew exponentially with time. This can be cured by reducing the time step in the problem, but instead we have chosen to arbitrarily reduce the coefficient 1.44 in the lower plenum region. This allows us to compute more efficiently without sacrificing any important physical effects since it only applies in the  $\overline{T'^2}$  equation. While the diffusion coefficients in Eqs. (5) and (17) appear quite different, it is shown in Appendix A that both have the same form and differ only by a constant multiplier. Thus STXR in Eq. (86) can be expressed

$$STXR = 1.44 \frac{\sigma_T^n}{\rho} \left( \frac{TPS_{i+1,jk}^n - TPS_{i,jk}^n}{\delta x_{i+\frac{1}{2}}} \right). \quad (87)$$

The production term involves a temperature gradient normal to the axis of the buoyant jet in the mixing plane. In the downcomer this is an azimuthal gradient, which we write

$$DTDX_{i,jk} = \frac{1}{2} \left[ \delta x_{i-\frac{1}{2}} \left( \frac{T_{i+1,jk}^{n+1} - T_{i,jk}^{n+1}}{\delta x_{i+\frac{1}{2}}} \right) + \delta x_{i+\frac{1}{2}} \left( \frac{T_{i,jk}^{n+1} - T_{i-1,jk}^{n+1}}{\delta x_{i-\frac{1}{2}}} \right) \right] / \delta x_{s_i}. \quad (88)$$

The production term is then

$$PROD = 0.33(DTDX_{i,jk})^2 (k_{i,jk}^{n+1})^2 / \epsilon_{i,jk}^{n+1}. \quad (89)$$

The decay of  $\overline{T'^2}$  is expressed

$$\text{DECAY} = 1.2 > \epsilon_{ijk}^{n+1} \text{TPS}_{ijk}^n / k_{ijk}^{n+1} \cdot \quad (90)$$

With these formulations we need only specify the advection terms in order to complete the first step of the  $\overline{T'^2}$  solution, which is

$$\text{TPS}_{ijk} = \text{TPSLAG}_{ijk} - \delta t \text{TPSFLX}_{ijk} \cdot \quad (91)$$

These advective fluxes have the same form as the temperature flux  $\text{TFLX}_{ijk}$  in Eq. (59) and are not repeated here. Likewise the Tensor Viscosity<sup>8</sup> and FRAM<sup>9</sup> procedures correspond to those of the temperature field and are not repeated.

#### IV. EXPERIMENTAL COMPARISONS

A series of experiments have been performed by Creare, Inc.<sup>11</sup> to examine fluid-thermal mixing in a cold leg and a 90° sector of an unwrapped downcomer at 1/5th scale. Figure 1 shows an elevation view of the cold leg and a planar view of the downcomer from the experimental report.<sup>11</sup> Attached to the cold leg are a number of high-pressure-injection (HPI) ports that were used in various experiments to supply cold water to the system, which was initially filled with warm water. Warm water is continually supplied to the system through the riser section shown at the left of the cold leg in the figure. Thermocouples were located at various positions in the cold leg and downcomer to measure the transient temperature variation that results from the mixing of these fluids.

We have performed SOLA-PTS calculations in a geometry similar to the Creare configuration. The principal differences are that in the calculations the cold leg is represented as a square duct rather than a round pipe, the vertical inlet section of the cold leg is not included, and a 30° horizontal bend in the cold leg (not shown in the figure) is represented by a flow-resistance. We do include the hot leg obstacle and the downcomer expansion in the numerical study. This downcomer expansion is an indentation in the vessel wall that extends from the bottom of the downcomer to the lower of the two horizontal lines below the cold leg in Fig. 1 and over the full width of the downcomer.

We present comparisons with two of the Creare experiments, runs 50 and 51. Run 50 is a zero-loop-flow experiment, while in run 51 the ratio of loop to HPI flow rates is approximately 2. In both cases the HPI injection was through the pipe angled at 60° with the horizontal and closest to the downcomer in Fig. 1. The total number of computation cells in these calculations is 7557, of which 3977 are fluid cells and the rest boundary cells. The calculation of Creare experiment 50 to 100 s required 104 minutes of computer time on the Cray-1 computer, while the calculation of experiment 51 to the same time required 89 minutes.

#### A. Creare Experiment 51

We make comparisons with run 51 first. Table IV lists the experimental initial conditions for this experiment. The thermocouple locations listed in Table IV correspond to those shown in Fig. 1.

In the calculation the initial fluid temperature in the cold legs and downcomer is uniform at 147.9°F, and the fluid is at rest. At time zero the loop and HPI flows are initiated. This procedure differs from the experimental one in that a steady loop flow was present in the cold leg at the time of HPI initiation in the experiments. This difference may account for the only serious discrepancy between the calculated and experimental measurements, which exists at the HPI inlet.

Figures 2-8 show the calculated velocity vector and temperature contour plots for run 51 at a time of 100 seconds after HPI initiation. A velocity plot in a vertical cut through the centerline of the cold leg is shown in Fig. 2.

**TABLE IV**  
**INITIAL CONDITIONS FOR CREARE RUN 51**

Loop flow rate	4.00 gpm
HPI flow rate	2.14 gpm
Froude number	0.053
Loop flow temperature, TC 30	147.34°F
HPI temperature	62.00°F
Cold leg bottom temperature, TC 1	149.29°F
Vessel-wall temperature, TC 7	148.45°F
Vessel-wall temperature, TC 12	147.56°F
Core-barrel wall temperature, TC 8	147.69°F

This plot shows the HPI injection region about midway in the cold leg. There is a cold-fluid layer flowing from this region to the downcomer along the bottom of the cold leg and a much weaker counterflowing warm layer at the top of the cold leg. Conversely, upstream from the HPI inlet there is a circulating flow with a weak cold layer on the bottom and a strong warm layer on top. These flow distributions reflect the effect of loop flow in the cold leg.

As the flow from the cold leg enters the downcomer, it impacts on the core barrel wall and greater flow velocities develop on this surface than on the vessel wall. This radial velocity gradient is accentuated when the vertical flow reaches the downcomer expansion. In the lower plenum region the fluid flows under the core barrel wall and rises to exit at the top of the core region. The flow out of this surface exactly balances the HPI and loop flows into the system. Indeed the purpose of including a core region in these calculations is to locate the outflow boundary far away from the dynamics of interest in the downcomer and cold leg so that the influence of this boundary flow will be negligible. This core region has been coarsely noded and made shorter than the downcomer in order to reduce the number of computation cells. The finest noding in the calculation is across the downcomer gap and in the cold leg near the downcomer junction.

Figures 3 and 4 are velocity plots in horizontal planes through the bottom and top of the cold leg, respectively. In Fig. 3 we can see the region of impact of the HPI flow on the bottom of the cold leg and the spreading upstream and downstream. We also see that when the fluid impacts on the core-barrel wall, it spreads along that surface and produces small recirculation regions on each side of the cold leg flow. The empty region on the right side of the downcomer is the hot leg obstacle. Figure 4 shows that azimuthally flowing fluid is entrained into the top of the cold leg to form a weak countercurrent flow up to the HPI region. A much stronger flow exists upstream from the HPI inlet bringing loop flow toward the downcomer. Notice that this fluid flows around the incoming HPI jet.

Figures 5 and 6 show velocity plots in vertical planes parallel and adjacent to the core-barrel and vessel walls, respectively. Actually, the plane shown in Fig. 6 is adjacent to the vessel wall only in the upper part of the downcomer; below the downcomer expansion region this vertical plane is displaced about 1.5 cm from the vessel wall. The blank region in the upper right in the figure is the hot leg obstacle. From the placement of this obstacle one can see by comparing with Fig. 1 that the calculational and experimental geometries are reversed azimuthally.

The arrangement of the velocity vectors in Figs. 5 and 6 shows that the flow circulation in the downcomer diverts the falling cold fluid from the hot leg side with displaced warm water rising under the hot leg. The comparison of calculated and experimental temperatures shown below demonstrates a similar trend in the experimental data. Notice that the converging lateral flows in Fig. 6 tend to narrow the cold fluid region below the cold-leg outlet. Conversely, the flow on the core-barrel side in Fig. 5 spreads below the cold-leg outlet due to the impaction on this wall.

Figures 7 and 8 show temperature contour plots in the same vertical planes as the velocity plots of Figs. 5 and 6. The displacement of the cold fluid away from the hot leg side that was noted above is evident here. The cold fluid region is quite broad and extends to the bottom of the downcomer in Fig. 7 on the core barrel wall, but on the vessel side, Fig. 8, the cold fluid region is narrower and shorter. The mixing of warm recirculating water with the cold water plume on the vessel side seen in Fig. 6 has greatly reduced the penetration of that plume. In the transient temperature plots below, we will see this temperature difference between the core-barrel and vessel walls.

The transient temperature comparisons between calculation and experiment for Creare run 51<sup>11</sup> are shown in Figs. 9-34. The Creare data shown in these plots were digitized from the Creare report.<sup>11</sup> In each plot an insert shows the position of the sensor relative to an elevation sketch of the facility and the Creare sensor location is listed on the vertical legend; to determine the position of these sensors relative to the cold leg centerline, see Fig. 1.

A series of these transient temperature plots showing comparisons between the calculation and the experiment at positions at or near the bottom of the cold leg are shown in Figs. 9-13. The calculated temperatures are in excellent agreement with experiment in all cases except Fig. 10, which shows the temperature immediately below the HPI inlet. The calculated temperature there is approximately 20°F colder than the experimental measurement, indicating less mixing between the HPI and loop flows than actually occurred at this location. Indeed, we saw in Fig. 4 that the loop flow splits at the HPI inlet to flow around the inlet jet. This behavior may result from the nature of the initial conditions in the calculations, in which the HPI and loop flows were initiated simultaneously. The good agreement with experiment at the other locations indicates that the turbulence model is producing the proper mixing in the neighborhood of the jet.

The series of temperature plots in Figs. 14-18 show comparisons of the calculated results with temperatures measured on a thermocouple rake that spanned the cold leg height in the Creare experiment. The calculated temperatures shown in these plots were obtained by interpolation using an area weighting that related the square cross section of the cold-leg duct to the round experimental pipe. The comparison with experiment is good in all cases. Notice in Figs. 14 and 15 that the initial temperature was several degrees colder than in the experiment. This reflects the initial temperature variation in the experiment as contrasted with the assumed uniform initial temperature in the calculations.

Figures 19-23 show temperature comparisons along an azimuthal line on the vessel wall directly below the cold-leg junction (see Fig. 1). The Creare data<sup>11</sup> show large temperature oscillations in Figs. 21 and 22 and lesser fluctuations in the other figures. These oscillations probably reflect turbulent fluctuations in momentum and temperature in this low-pressure flow-separation region below the lip of the cold leg. The details of the turbulent motions cannot be computed in the calculations, but their effects are included in an average sense by the turbulence model. However, the calculations do capture the most macroscopic oscillations, which correspond to transient flow reversals in this part of the downcomer. Both the calculation and the experiment show an asymmetry in the cooling, with greater cooling occurring on the side opposite the hot-leg obstacle. Indeed, the fluid is cooler at thermocouple 27 than at thermocouple 7, which is located directly below the centerline of the cold leg.

The temperature variations on the core-barrel wall at approximately the same elevation as the vessel-wall data of Figs. 19-23 are shown in Figs. 24-26. These results differ markedly from those on the vessel wall. There is a greater spreading of the cold fluid on the core-barrel wall and a more uniform temperature decay rate. The experimental profile in Fig. 24 shows some large temperature fluctuations, which are probably related to the fact that this thermocouple is near the boundary between the cold and warm fluids. Both the calculation and the experiment show a similar asymmetry in the cooling pattern to that seen on the vessel side.

Figures 27-29 show the temperature comparisons along an azimuthal line on the vessel wall in the expanded region of the downcomer, and Fig. 30 shows the corresponding temperature on the core-barrel wall. The vessel-wall temperatures from both calculation and experiment exhibit less fluctuation than was seen in Figs. 19-23, probably because of the sheltering effect of the step in the vessel

wall (see Fig. 2). However, these vessel-wall plots do show the azimuthal asymmetry in temperature seen above. The calculated temperatures are in excellent agreement with the data on both the vessel- and core-barrel-wall sides.

Another group of temperature plots along an azimuthal line on the vessel wall and a plot at a corresponding elevation on the core-barrel wall are shown in Figs. 31-34. The trends here are very similar to those seen in Figs. 27-30. On the vessel side the experimental temperature fluctuations are small in amplitude, there is an asymmetry in the plots with the colder fluid on the side opposite the hot leg, and the calculated and experimental temperatures are in excellent agreement. On the core-barrel side, the calculated temperature is in good agreement with experiment at late times but about 5°F cooler at early times. The experimental temperatures show little variation across the downcomer gap at this elevation, as can be seen from Figs. 32 and 34.

#### B. Creare Experiment 50

The results presented above for experiment 51 demonstrate the capability of the SOLA-PTS code in modeling the fluid-thermal interactions that develop in the cold leg and downcomer when there is significant loop flow. The agreement with experiment was good, not only with regard to the transient temperature variation along the centerline of the cold leg and its projection in the downcomer, but also with regard to the azimuthal asymmetries in temperature. We now turn to experiment 50, which is a zero-loop-flow experiment. Buoyancy effects play a more important role in this application, so it should provide a good test of the  $k-\epsilon-T'^2$  turbulence model. Table V gives the experimental initial condition for experiment 50.

In the calculations the initial fluid temperature in the cold leg and downcomer is uniform at 149.9°F, so we can see from Table V that there will be some initial temperature differences between the calculation and the experiment. At time zero begin the injection of HPI flow into the stagnant fluid in the downcomer.

Figures 35-41 show velocity-vector and temperature-contour plots at a time of 100 seconds, which corresponds to the termination of the calculation. Figure 35 is a velocity plot in a vertical cut through the centerline of the cold leg showing flow in the cold leg, downcomer, lower plenum, and core. This plot shows a stronger countercurrent flow in the cold leg between the HPI region and the downcomer than was seen in the corresponding loop flow plot, Fig. 2. However,

**TABLE V**  
**INITIAL CONDITIONS FOR CREARE RUN 50**

Loop flow rate	0 gpm
HPI flow rate	4.00 gpm
Froude number	0.106
HPI temperature	64.00°F
Cold leg bottom temperature, TC 1	151.98°F
Vessel-wall temperature, TC 7	149.39°F
Vessel-wall temperature, TC 12	149.26°F
Core-barrel-wall temperature, TC 8	149.52°F

upstream from the HPI inlet the circulation is weaker than in Fig. 2, because of the lack of loop flow. The flow from the cold leg impacts on the core-barrel wall and there is a strong velocity gradient across the downcomer gap. The flow in this vertical plane comes almost to rest midway down the downcomer. We will see in some of the plots presented below that the reason for this is that the cold-water plume has shifted further to the side away from the hot leg at this particular time in the transient. As a result of this azimuthal shift in the plume location, which begins at about  $t = 70$  s, there is an apparent divergence between calculated and experimental temperatures in the lower part of the downcomer at late times. It actually corresponds to a lateral shift in the calculated plume location relative to the experimental one.

Velocity plots in horizontal planes through the bottom and top of the cold leg, respectively, are shown in Figs. 36 and 37. In Fig. 36 we see the effect of the impact of the HPI jet on the bottom of the cold leg and the spreading of this cold fluid upstream and downstream. When this cold stream enters the downcomer, the velocity vectors indicate a turn away from the hot-leg obstacle, which occupies the blank region on the right in the plot. At the top of the cold leg, Fig. 37, the returning warm fluid enters from the hot-leg side and is entrained into the cold leg. This fluid flows back to the HPI inlet region where it mixes with that cold fluid and with the fluid that is circulating upstream from the HPI inlet.

Figures 38 and 39 are velocity-vector plots in vertical planes parallel and adjacent to the core barrel and vessel walls, respectively. (As discussed above the vessel-wall plot is only immediately adjacent to that wall above the down-



comer expansion.) As these plots show, there is a displacement of the cold fluid plume to the side away from the hot-leg obstacle at this time in the transient. This is why Fig. 35, which is in a vertical plane through the cold-leg centerline, shows an almost stagnant velocity field in the lower part of the downcomer. It also explains why some of the calculated temperatures in the downcomer rise at late times in the transient-temperature plots shown below. At that time the locations at which those temperatures are measured are outside of the cold fluid stream.

Temperature contour plots in these same vertical planes adjacent to the core-barrel and vessel walls are shown in Figs. 40 and 41. These plots show the same azimuthal displacement seen in the velocity plots in Figs. 38 and 39. The temperature plot on the vessel wall, Fig. 41, shows a narrower plume than that on the core-barrel wall in Fig. 40. However, the vessel-wall plume does penetrate to the bottom of the downcomer, unlike the loop-flow case shown in Fig. 8. Also this plume is colder than that of Fig. 8.

Some comparisons between calculated and experimental temperatures at or near the bottom of the cold leg for Creare run 50 are shown in Figs. 42-46. The calculated temperatures are in very good agreement with experiments for these thermocouples. In particular this is true at thermocouple 34, Fig. 43, which is located directly under the HPI inlet. This is in contrast to Fig. 10, which showed poor agreement at this location for Creare run 51 with loop flow.

The calculated temperature curves in Figs. 42-46 show a drop in temperature at about 60 s that does not appear in the experimental curves. This temperature drop appears to be related to the cooling of the fluid that is circulating in the region upstream from the HPI inlet. Recall that the vertical inlet section to the cold leg, from which warm water is supplied to the system in the Creare experiments (Fig. 1), is not included in the calculation. The cold-leg duct upstream from the HPI inlet is closed at the position where the vertical inlet section begins. Thus any cold fluid that splashes upstream along the bottom of the cold-leg duct gives rise to a circulation in that region and a cooling of this upstream fluid. As a result of the circulating flow, this upstream fluid mixes with the HPI water at the top of the duct (Fig. 2). It requires about 50 or 60 s for this upstream mixing fluid to show an appreciable cooling at the top of the duct, and this time interval is consistent with the temperature drop seen in the calculated temperatures of Figs. 42-46. This same phenomenon would not be seen at this time in the experiments because the cold water that flows upstream along

the bottom of the cold-leg pipe would fill the vertical inlet pipe displacing warm water that would flow back along the top of the cold-leg pipe to mix with the HPI fluid. Reference 12, which makes comparisons of SOLA-PTS calculations with Creare test 50 for 200 s using an earlier version of the code, shows that once this temperature discrepancy between calculation and experiment develops, it is maintained throughout the calculation.

Figures 47-51 show temperature transients measured in the experiment on the thermocouple rake that spans the cold leg just upstream of the junction with the downcomer. The calculation is in good agreement with the experiment at the bottom and top of the cold leg, but there is a large discrepancy at the center. Thermocouple 3 in the middle of the cold leg shows a colder trend in the calculation than in the experiment, indicating that the cold fluid layer is thicker in the calculation. This thicker cold layer in the calculations is probably the result of excluding the riser section of the cold leg pipe. As indicated above, this leads to an accumulation of cool water upstream from the HPI inlet and the mixing of this cool water with the HPI fluid. This produces a thicker cold layer downstream from the HPI inlet. The large oscillations in the experimental temperature profile in Fig. 49 indicate that thermocouple 3 is close to the boundary between the hot and cold fluids during the early stages of the transient.

A series of temperature transients along an azimuthal line on the vessel wall just below the cold leg outlet is shown in Figs. 52-56. As with experiment 51, these plots show an azimuthal asymmetry, with the coldest fluid and the greatest temperature fluctuations occurring on the side opposite the hot leg obstacle. This is true in both the calculation and the experiment. The large temperature oscillations in this region result from the turbulent nature of the flow in this low-pressure region below the cold-leg lip. The calculations do not resolve the short time period oscillations seen in the experimental data, but they include these in an average sense through the turbulent-mixing model.

Temperature plots along an azimuthal line on the core-barrel side at about the same elevation as Figs. 52-56 are shown in Figs. 57-59. These temperatures on the core barrel wall show less fluctuation and greater cooling than on the vessel wall side. The experimental data in Fig. 57 show some large-amplitude oscillations, but these are probably related to the fact that this thermocouple is very close to the boundary of the cold plume on the core-barrel wall.

Notice that the calculated temperatures in Figs. 56 and 59 show a greater decrease in temperature after 70 s than occurs at the other locations along these

azimuthal lines on the vessel and core-barrel walls. These asymmetries are related to the displacement of the cold water stream to the side opposite the hot leg seen in Figs. 38-41. The experimental results do not show as great a tendency toward asymmetry. Thus, while the calculations continue to predict approximately the same minimum temperature on these walls as the experiment, the location of this minimum is shifted azimuthally relative to the experiment at late times.

Temperature plots along an azimuthal line on the vessel wall below the downcomer expansion are shown in Figs. 60-62, and a corresponding plot at about the same elevation on the core-barrel wall is shown in Fig. 63 (see Fig. 1). Figure 63 shows a departure of the calculated from the experimental temperatures at late times that results from the azimuthal shift of the calculated cold-water plume discussed above.

Another series of plots of temperatures on the vessel wall lower in the downcomer are shown in Figs. 64-66, and a corresponding plot at about the same elevation on the core-barrel wall is presented in Fig. 67. The latter figure shows an increase in temperature in the calculation after 55 s as a result of this lateral shift in the cold-water plume that we have been discussing.

In addition to the experimental comparisons presented in this section, the SOLA-PTS code has been tested by comparisons with an analytic solution to the laminar thermal-hydraulic entry-length problem and by comparison with experimental measurements of turbulent flow between parallel plates.<sup>13</sup>

The interested reader is also referred to Reference 14 for an application of the SOLA-PTS code to plant-specific accident scenarios.

#### ACKNOWLEDGMENTS

We wish to acknowledge the assistance of John K. Dukowicz in implementing the Conjugate Residual solution procedure for the pressure field.

#### REFERENCES

1. C. W. Hirt and L. R. Stein, "Numerical Simulation of Wind Forces on Structures," Proceedings of the Third U. S. National Conference on Wind Engineering Research, February 26-March 1, (University of Florida, Gainesville, Florida, 1978).
2. C. W. Hirt, J. D. Ramshaw, and L. R. Stein, "Numerical Simulation of Three-Dimensional Flow Past Bluff Bodies," Computer Methods in Applied Mechanics and Engineering 14, 93 (1978).

3. C. J. Chen and W. Rodi, "A Mathematical Model for Stratified Turbulent Flow and Its Application to Buoyant Jets," 16th IAHR Congress, Sao Paulo, Brazil (1975).
4. C. J. Chen and C. P. Nikitopolous, "On the Near Field Characteristics of Axisymmetric Turbulent Buoyant Jets in a Uniform Environment," *Int. J. Heat Mass Transfer* 22, 245 (1979).
5. B. E. Launder and B. D. Spalding, "The Numerical Computation of Turbulent Flows," *Computer Methods in Applied Mechanics and Engineering* 3, 269 (1974).
6. P. L. Violette, "Turbulent Mixing in a Two Layer Stratified Shear Flow," Second International Symposium on Stratified Flows, Trondheim, Norway (1980).
7. J. E. Welch, F. H. Harlow, J. P. Shannon, and B. J. Daly, "THE MAC METHOD: A Computing Technique for Solving Viscous, Incompressible, Transient Fluid-Flow Problems Involving Free Surfaces," Los Alamos Scientific Laboratory report LA-3425 (1966).
8. J. K. Dukowicz and J. D. Ramshaw, "Tensor Viscosity Method for Convection in Numerical Fluid Dynamics," *J. Comput. Phys.* 32, 71 (1979).
9. M. Chapman, "FRAM: Nonlinear Damping Algorithms for the Continuity Equations," *J. Comput. Phys.* 44, 84 (1981).
10. R. Chandra, "Conjugate Gradient Methods for Partial Differential Equations," Ph.D. Thesis, Yale University (1978).
11. P. H. Rothe and M. F. Ackerson, "Fluid and Thermal Mixing in a Model Cold Leg and Downcomer with Loop Flow," Electric Power Research Institute report NP-2312 (1982).
12. B. J. Daly and M. D. Torrey, "Three-Dimensional Thermal-Hydraulic Calculations using SOLA-PTS," Proceedings of the Eleventh Water Reactor Safety Research Information Meeting, Gaithersburg, Md., Oct. 24-28, 1983, U. S. Nuclear Regulatory Commission report NUREG/CP-0048 (1984), Vol. 2, p. 48.
13. B. J. Daly, B. A. Kashiwa, and M. D. Torrey, "Calculations of Pressurized Thermal Shock Problems with the SOLA-PTS Methods," Proceedings of the Tenth Water Reactor Safety Research Information Meeting, Gaithersburg, Md, October 12-15, 1982, U. S. Nuclear Regulatory Commission report NUREG/CP-0041 (1983), Vol. 2, p. 113.
14. B. J. Daly, "Three-Dimensional Calculations of Transient Fluid-Thermal Mixing in the Downcomer of the Calvert Cliffs-1 Plant Using SOLA-PTS," Los Alamos National Laboratory report LA-10039-MS, NUREG/CR-3704 (1984).

## APPENDIX A

### COMPARISON OF THE TURBULENCE MODELS

For the same conditions considered in the text, in which  $x$  and  $U$  are parallel to the jet axis and  $y$  and  $V$  are normal to that axis in the mixing plane, we compare in Table A-I the magnitude and form of affected terms using the  $k$ - $\epsilon$  model<sup>5</sup> and  $k$ - $\epsilon$ - $\overline{T'^2}$  model.<sup>3,4</sup>

Consider the coefficients of the diffusion terms first, since they appear in all of the equations. These reduce in both models to a numerical coefficient times the quantity  $k^2/\epsilon$ . A comparison of these numerical coefficients shows that the use of the  $k$ - $\epsilon$ - $\overline{T'^2}$  model results in increases in the magnitudes of these diffusion terms by 84% in the thermal energy equation, 30% in the turbulent energy equation, and 15% in the turbulent-energy decay-rate equation. Replacing the bracket term of the momentum-equation diffusion coefficient in the  $k$ - $\epsilon$ - $\overline{T'^2}$  model by unity results in a 20% increase in the momentum diffusion with the  $k$ - $\epsilon$ - $\overline{T'^2}$  model. However, the bracket term will generally be greater than unity in the buoyant jet since  $\partial T/\partial y$  and  $\partial U/\partial y$  should have the same sign.

The same relationship that holds between the two models in the momentum diffusion coefficients applies to the shear-creation coefficients in the  $k$  and  $\epsilon$  equations. The use of the  $k$ - $\epsilon$ - $\overline{T'^2}$  model results in a 20% increase in this coefficient by virtue of the terms outside of the bracket and a further increase due to the bracket term.

The buoyancy-creation term of the  $k$  and  $\epsilon$  equations shows the greatest departure of the  $k$ - $\epsilon$ - $\overline{T'^2}$  model from the  $k$ - $\epsilon$  model. It is through this term that the fluctuating temperature field affects the turbulent mixing of momentum and energy. Indeed we find that the third term in the bracket, the term proportional to  $\overline{T'^2}$ , is generally the dominant buoyancy-creation term and usually contributes to an increase in the levels of  $k$  and  $\epsilon$  for both stable and unstable temperature fields [see Eq. (12)]. The success of the  $k$ - $\epsilon$ - $\overline{T'^2}$  model in simulations of buoyant-jet flow indicates that a substantial part of the fluctuating energy resides in the temperature field. However, the presence of this term indicates that the  $k$ - $\epsilon$ - $\overline{T'^2}$  model is not likely to produce good results in stratified pipe flow where it is observed that the turbulence energy is generally suppressed in a stable temperature field.<sup>6</sup>

The decay terms are identical in the  $k$ - $\epsilon$  and the  $k$ - $\epsilon$ - $\overline{T'^2}$  models.

TABLE A-1  
COMPARISON OF THE TERMS

	<u>k-ε Model<sup>a</sup></u>	<u>k-ε-T'<sup>2</sup> Model<sup>b</sup></u>
<u>Kinematic Diffusion Coefficients</u>		
Momentum Eq.	$c_{\mu} \frac{k^2}{\epsilon}$	$\frac{1 - c_0}{c_1} \frac{\overline{v^2}}{k} \left[ 1 - \frac{1}{c_h} \frac{k}{\epsilon} \alpha g (\partial T / \partial y) / (\partial U / \partial y) \right] \frac{k^2}{\epsilon}$
Thermal Energy Eq.	$c_{\mu} \frac{k^2}{\epsilon}$	$\frac{1}{c_h} \frac{\overline{v^2}}{k} \frac{k^2}{\epsilon}$
k Eq.	$\frac{c_{\mu}}{\sigma_k} \frac{k^2}{\epsilon}$	$c_k \frac{\overline{v^2}}{k} \frac{k}{\epsilon}$
ε Eq.	$\frac{c_{\mu}}{\sigma_{\epsilon}} \frac{k^2}{\epsilon}$	$c_{\epsilon} \frac{\overline{v^2}}{k} \frac{k}{\epsilon}$
$\overline{T'^2}$ Eq.	—	$c_T \frac{k^2}{\epsilon}$
<u>Shear-Creation Coefficients</u>		
k, ε Eqs.	$c_{\mu} \frac{k^2}{\epsilon}$	$\left( \frac{1 - c_0}{c_1} \right) \frac{\overline{v^2}}{k} \left[ 1 - \frac{1}{c_h} \frac{k}{\epsilon} \alpha g (\partial T / \partial y) / (\partial U / \partial y) \right] \frac{k^2}{\epsilon}$
<u>Buoyancy-Creation Terms</u>		
k, ε Eqs.	$c_{\mu} \frac{k^2}{\epsilon} \alpha g \frac{\partial T}{\partial y}$	$-\alpha g \frac{1}{c_h} \frac{k}{\epsilon} \left[ -\overline{uv} \frac{\partial T}{\partial y} - \overline{vT'} (1 - c_{hl}) \frac{\partial U}{\partial y} \right. \\ \left. - (1 - c_{hl}) \alpha g \overline{T'^2} \right]$
<u>Decay Terms</u>		
k Eq.	-ε	-ε
ε Eq.	$-c_2 \frac{\epsilon^2}{k}$	$-c_{\epsilon 2} \frac{\epsilon^2}{k}$

<sup>a</sup>The values of the coefficients are given in Table I.

<sup>b</sup>The values of the coefficients are given in Table III.

## APPENDIX B

### RUNNING A PROBLEM WITH SOLA-PTS

A problem input file and a problem update file are needed to compute with SOLA-PTS. The input file contains information needed to generate a mesh and to set initial conditions. The problem update file is used to prescribe the boundary conditions for the problem.

Table B-I shows a typical input file for SOLA-PTS. Information is supplied to the code through a namelist file called XPUT, as indicated on the first line in Table B-I. All of the quantities in the file XPUT have default values that are listed in the subroutine RINPUT. Thus, one only needs to specify in the input file those variables that have values different from the default values.

Line 2 in Table B-I contains the problem identifiers JNM and NAME, which are included in the headings and titles of the printed and plotted output. Lines 3 and 4 contain information that is specific to this problem. EPSI is the initial value of the convergence criterion in the pressure iteration, and DELT is the initial value of the time increment. These quantities are automatically adjusted within the code in such a way as to maximize efficiency without compromising accuracy. EPSI is reduced by 5% in each cycle for which the number of iterations is less than 25, until the normal operating value  $10^{-4}$  is reached. DELT is increased by 5% each cycle unless limited by the Courant stability limit,

$$\delta t < 0.75 \left( \left| \frac{\delta x}{U} \right|, \left| \frac{\delta y}{V} \right|, \left| \frac{\delta z}{W} \right| \right)_{\max}, \quad (\text{B-1})$$

or by a diffusional stability limit. The term TI is the initial temperature in the system, while TO is the reference temperature in the Boussinesq term in the momentum equation. The variables PLTDT, TDDT, TWFN, and VELMX control output from the calculation. PLTDT is the time interval between plots, TDDT is the interval between tape dumps, and TWFN is the time when the problem will end. These quantities are specified in problem time units. (We do not usually generate printed output, so the time interval between prints PRTDT has a large default value.) Finally, VELMX is a scaling factor for the velocity vectors.

Lines 6-19 in Table B-I are concerned with the mesh generation for the problem. The procedure for generating meshes in SOLA-PTS is to build large meshes from a series of submeshes. In the example the number of submeshes in the

x-direction is  $NKX = 3$ . The first of these submeshes extends from  $XL(1) = 0.$  to  $XL(2) = 19.5112$ , with the minimum cell size in this interval occurring at  $XC(1) = 16.9792$ . The minimum  $\delta x$  in this interval is  $DXMN(1) = 2.532$ , and there are  $NXL(1) = 6$  cells on the left of  $XC(1)$  and  $NXR(1) = 1$  cell on the right of  $XC(1)$ . Using this information the mesh generator builds cells from the minimum values bordering  $XC(1)$  and increasing in size quadratically from this point. The result of this exercise is to build a submesh of seven cells in the x-direction with cell boundaries at 0.0, 3.1277, 6.1363, 9.0257, 11.7961, 14.4472, 16.9792, and 19.5112.

The next submesh in the x-direction extends from  $XL(2) = 19.5112$  to  $XL(3) = 44.29$ , with the smallest mesh cells centered at  $XC(2) = 24.5752$ . There are  $NXL(2) = 2$  cells to the left of  $XC(2)$  and  $NXR(2) = 7$  cells to the right. The minimum cell size in this region is  $DXMN(2) = 2.532$ . Notice that in this subregion the spacing from  $XL(2)$  to  $XC(2)$  has been chosen to be twice the minimum cell size, 2.532. The cell to the right of  $XC(2)$  will also have this minimum size, as did the last two cells in the first x submesh. Thus five cells in a row have been given a uniform size of 2.532. These five cells span the cold leg, a region where relatively fine resolution is needed and where uniform cell size is preferred. The cell size increases in both directions away from the cold leg, with the minimum cell size in the third x submesh  $DXMN(3) = 3.685$ .

The y and z submeshes are constructed in the same manner. There are  $NKY = 4$  submeshes in the y-direction and  $NKZ = 2$  submeshes in the z-direction. These are formulated to maximize resolution across the downcomer gap and in the cold leg, with a coarser grid elsewhere.

Lines 20-27 in Table B-I provide information that controls the graphics output. The velocity plots are prescribed through the quantities  $IV1(n)$ ,  $IV2(n)$ ,  $JV1(n)$ ,  $JV2(n)$ ,  $KV1(n)$ , and  $KV2(n)$  on lines 21-23. The coordinate reference is in terms of mesh cells. For example, for the first velocity plot  $IV1(1) = 9$ ,  $IV2(1) = 9$ ,  $JV1(1) = 2$ ,  $JV2(1) = 99$ ,  $KV1(1) = 2$ , and  $KV2(1) = 99$ . This indicates that the plot is over a constant I plane,  $I = 9$ , and covers the full range of fluid cells in the J- and K-directions, the value 99 indicating the upper limit. This same procedure holds for the contour plots, using the information on lines 24-26.

Table B-II shows a problem update file in which quantities that are peculiar to a specific study are specified. These are primarily boundary conditions. Line 3 of Table B-II identifies the amount of storage required for the three-



dimensional arrays, in this case 241000 words. To determine this value, one can start a calculation using a large tentative value for IBASC but stop it early in subroutine SOLA. The value of the quantity NCR2 in memory at that time is the minimum value of IBASC for the problem. While the calculation is stopped at this point, it is convenient to inspect other variables. For example, RIJK is the reciprocal of the total number of fluid cells in the study, exclusive of boundary cells. One can also examine the mesh that has been generated for the problem at this time by displaying the film file PLOT.

The parameter LMX on line 5 must have a minimum value that is 6 times the maximum of IMAX x JMAX, IMAX x KMAX, or JMAX x KMAX, where IMAX, JMAX, and KMAX are the total number of cells in each of the coordinate directions, including boundary cells. For the example of Table B-I,

$$IMAX = \sum_{n=1}^3 [NXL(n) + NXR(n)] + 2 = 22 ,$$

$$JMAX = \sum_{n=1}^4 [NYL(n) + NYR(n)] + 2 = 42 , \text{ and}$$

$$KMAX = \sum_{n=1}^2 [NZL(n) + NZR(n)] + 2 = 33 .$$

Thus the minimum value of LMX is 8316 (6 x JMAX x KMAX). The parameters IKP100 and IKP200 on lines 7 and 9 have the values

$$IKP100 = IMAX \times KMAX + 100 \text{ and}$$

$$IKP200 = IMAX \times KMAX + 200 .$$

Lines 10-27 in Table B-II supply the boundary conditions at the HPI inlet. WINECC is the injection velocity of HPI fluid, obtained by dividing the volume rate of flow by the inlet area. In this particular example, the fluid is in-

jected through the tops of two cells located at  $I = 9$ ,  $J = 28$  and  $29$ , and  $K = 24$ . (These cells lie at the top of the cold leg on the centerline.) The vertical component of velocity at the tops of these cells is set equal to the inlet velocity on line 18. The HPI injection pipe is angled at  $60^\circ$  to the cold-leg pipe, so we include a y-component of velocity in the cell above the cold leg,  $VINECC = WINECC \times \cot 60^\circ$ . This tangential velocity does not contribute to the mass flow into the system, but it does affect the flow direction in the cold leg through the shear stress. This shear stress acting across the wall is limited to the HPI region; elsewhere a rigid wall boundary condition is applied.

Notice in lines 18-26 of Table B-II that single indexing is used in SOLA-PTS. The values of these indices are computed in subroutine CALCIJK, which is called on line 17. The calculation mesh in SOLA-PTS is subdivided into component meshes, which are distinct from the submeshes described above in the mesh generation procedure. A component mesh exists for each subregion of the mesh that has different I and K limits. In the present example there are three component meshes, corresponding to the core region, the downcomer, and the cold leg. Subroutine CALCIJK computes the indices for cells in each of the component meshes and for neighbors that may lie across a component mesh boundary.

The index convention used in SOLA-PTS is to refer to cell-centered quantities or face-centered velocities with the index IJK. For example,  $P(IJK)$  is the cell-centered pressure and  $W(IJK)$  is the vertical velocity component at the upper boundary of the cell. The index IJKP is used to access quantities for the cell above and IJKM for the cell below. The index IMJKP on line 21 refers to the cell on the left and above.

The variables referred to on lines 18-26 are the vertical component of velocity  $W$ , the radial component  $V$ , the azimuthal\* component  $U$ , the flag function BETA (by which we identify various types of boundary cells), the turbulent energy  $TE$ , the turbulent energy dissipation rate  $E$ , the temperature  $TEM$ , and the mean-square fluctuating temperature  $TPS$ . Setting BETA in the cell above to 1.0 on line 22 identifies that cell as a prescribed inflow cell. Other BETA values are 2.0 for a continuative inflow or outflow cell, 0.0 for an exterior boundary cell, -1.0 for an interior boundary cell, -2.0 for a heat-conducting boundary cell, and any number greater than 2.0 for a fluid cell.

---

\*We use the terms radial and azimuthal only for orientation purposes, since we deal with an unwrapped downcomer and compute in Cartesian coordinates.

The particular values used for  $TE$ ,  $E$ , and  $TPS$  on lines 23, 24, and 26 are reasonable to use at the HPI inlet, although the interior values of these quantities are not very sensitive to these boundary values. The temperature on line 13 is the prescribed HPI temperature from the Creare experiment.<sup>11</sup>

Lines 28-46 specify the loop flow boundary conditions at the end of the cold leg, which is located at  $J = 42$ . Lines 34-37 deal with an aspect of index calculations that was not encountered in the DO loop above. The call to IKLIMS4, an entry point in the CALC IJK subroutine, is made to calculate for the current value of  $J$  the upper and lower limits in the I- and K- directions, IUL, ILL, KUL, KLL. These limits are used in the DO loop specifications on lines 35 and 36. The call to IJKAJCT is similar to the call to CALC IJK on line 17 except that instead of all possible neighbors of cell IJK, we only need those with one increment displacement each in the I-, J-, and K-directions.

The loop flow inlet velocity and temperature, lines 31 and 32, are obtained from the Creare experiment. The value of BETA in the exterior boundary cells is set to 1.0 to signify a prescribed inlet boundary. The turbulent kinetic energy and its dissipation rate in the boundary cells are smaller than at the HPI inlet corresponding to the smaller Reynolds number of the loop flow, although, as indicated above, these inlet values do not strongly influence the interior turbulent field.

The Creare experiment<sup>11</sup> that is being considered here is one in which the mass flow rates at the HPI and loop flow inlets are constant. Therefore, the mass flow rate out through the top of the core is also constant and equal to the sum of the HPI and loop flow rates. This outflow, as shown on lines 48-53, is at K level 12 and spans the J planes 2 and 3.

In the rest of the update file shown in Table B-II only the problem-dependent lines from the code are replaced, and these often correspond to the setting of indices. The reader is therefore assumed to have a copy of the SOLA-PTS compile file available in order to interpret the context of the coding in which these update changes are made.

Lines 54-59 define the cells that will be occupied by the hot-leg obstacle. In the Creare experiments<sup>11</sup> the hot leg is represented as a hemispherical cylinder at one edge of the downcomer (Fig. 1). In the code we approximate the cylindrical boundary by a stair-step grid of cells.

The indices that define the cold leg are prescribed on lines 60-63. The fluid cells in the cold leg extend from J planes 9 - JM1, where JM1 = JMAX-1, and

over I planes 7 - 11 and K planes 20 - 24. I planes 6 and 12 and K planes 19 and 25 are rigid boundary cells (BETA = -1.0), except at the HPI inlet.

Lines 64-67 define the expansion region in the downcomer (Fig. 1) while lines 68-71 set the indices for the core-barrel wall obstacle. The BETA values for the HPI inlet, the loop flow inlet, and the top of the core are initially set on lines 72-81. Although these BETA values are also set in the boundary condition subroutine BC (see above), they must first be set here so that they will be available for setting the initial values of the variables in the SETUP subroutine.

The upper and lower limits on the I and K indices for the three mesh components considered in this example are defined on lines 84-86. The first group of numbers on lines 85 and 86 are I limits, the second group are K limits, and the third group are the J values that define the mesh components. Consider this third group of numbers on these two lines. The first numbers in these groups on lines 85 and 86 are 1 and 3, respectively. This signifies that the first mesh component extends from  $J = 1 - 3$ . The second pair of numbers indicates that the second mesh component covers the range  $J = 4 - 10$ , and the third pair of numbers indicates that the final mesh component includes  $J = 11 - 42$ . Corresponding to these values of J the three I limits are 1 - 22, 1 - 22, and 6 - 12, and the three K limits are 1 - 13, 1 - 33, and 19 - 25.

Lines 87-107 give the locations of the Creare thermocouples. The x-components of these sensor locations are listed relative to the value of x at the cold leg centerline XCLCL; the y-components are relative to the value of y at the vessel wall YVESWL; and the z-components are relative to the value of z at the bottom of the cold leg ZBOTCL. These values are listed on line 88. In this example there are 55 sensor locations. Transient temperatures are recorded at these positions in the course of the calculation and then compared with digitized Creare data<sup>11</sup> using a postprocessing routine.

Lines 108-109 specify a J plane at which various measurements of flow parameters are made in the cold leg and then printed at regular intervals during a calculation. The interested reader should inspect this region of the code to identify these parameters.

The beginning and ending J planes at which the three-equation model of turbulence is applied are specified with lines 110-114. J3EQ11 and J3EQ12 are the J limits of the first region in which this model is applied, which includes the downcomer, lower plenum, and core. The second region includes J planes

J3EQ21 - J3EQ22. This region includes the HPI inlet planes and two J planes on each side of these inlet planes.

The update changes on lines 115-138 deal with prints that indicate net flow through various planes in the calculation mesh. These prints give a measure of the accuracy of the pressure iteration in satisfying the incompressibility condition. If this condition is satisfied exactly, the flow through the various planes would be identical. However, the convergence of the iteration procedure is only approximate, so these flows should disagree slightly. Initially the convergence factor is coarse, so one should not expect good agreement between these numbers until the convergence criterion EPSI is reduced to  $10^{-4}$ .

The form loss at a horizontal bend in the Creare<sup>11</sup> cold leg is accounted for by the update changes on lines 139-141.

The modifications shown on lines 142-151 are concerned with certain Tensor Viscosity factors that are not computed at prescribed inlet and outlet boundaries and must be set over from interior cells.

Finally, the update change on lines 152-153 is an ad hoc adjustment to one of the turbulent shear-creation terms in the fluid computational cell below the core-barrel wall. The vertical component of the velocity in the plane of cells adjacent to the core barrel is usually large, while in the cell below the core-barrel wall this component is zero because it is normal to a rigid wall. As a result the derivative  $\partial W/\partial y$  can be so large that it distorts the turbulence field in the lower plenum region. To correct this we have arbitrarily reduced this derivative in this cell at the bottom of the core-barrel wall.

## TABLE B-1

## PROBLEM INPUT FILE FOR SOLA-PTS

```

1  $XPUT
2  JNM=8HCREARE51,NAME=14HTEST SOURCE33 ,
3  EPSI=0.01, DELT=0.01, TI=337.4, TU=337.4,
4  FLTDT=10.0, TDDT=20.0, TWFIN=10.2, VELMX=4.0,
5  $END
6  $MESHGN
7  NKX=3, XL(1)=0., 19.5112, 44.29, 62.23,
8  XC=16.9792, 24.5752, 47.49 ,
9  NXL=6,2,1,   NXR=1,7,3,
10 DXMN(1)=2.532, 2.532, 3.685,
11 NKY=4, YL=0.0, 10.0, 14.1275, 61.24, 183.8,
12 YC= 8.0, 11.031875, 15.0802, 96.4,
13 NYL= 2,1,1,7,   NYR=1,3,12,13,
14 DYMN=4.2,  1.031875, 1.5, 4.0,
15 NKZ=2, ZL=0.0, 92.502, 132.13,
16 ZC= 89.97, 102.63,
17 NZL=18,4,   NZR=1,8,
18 DZMN=2.532, 2.532,
19 $END
20 $GRAFIC
21 IV1(1)=9,2,2,11,2,2,2,7,   IV2(1)=9,99,99,11,99,99,99,7,
22 JV1(1)=2,2,2,2,6,5,8,2,   JV2(1)=99,99,99,99,6,5,8,99,
23 KV1(1)=2,24,20,2,2,2,2,2,   KV2(1)=99,24,20,99,99,99,99,99,
24 IC1(1)=9,2,2,2,2,7,2,2,   IC2(1)=9,99,99,99,99,7,99,99,
25 JC1(1)=2,2,2,6,8,2,5,7,   JC2(1)=99,99,99,6,8,99,5,7,
26 KC1(1)=2,24,20,2,2,2,2,2,   KC2(1)=99,24,20,99,99,99,99,99,
27 $END

```

## TABLE B-II

## PROBLEM UPDATE FILE FOR SOLA-PTS

```

1 *IDENT CREATE
2 *D,SLCOM1.2
3     PARAMETER (IBASC=241000)
4 *D,SLCOM1.5
5     PARAMETER (IJMX=9000)
6 *D,SLCOM1.7
7     PARAMETER (IKP100=826)
8 *D,SLCOM1.9
9     PARAMETER (IKP200=926)
10 *D,BC.22,64
11     WINECC=-6.67
12     VINECC=0.57735*WINECC
13     TINECC=289.67
14     K=24
15     I=9
16     DO 125 J=28,29
17     CALL CALCIJK
18     W(IJK)=WINECC
19     V(IJK)=VINECC
20     U(IJK)=0.0
21     U(IMJK)=0.0
22     BETA(IJK)=1.0
23     TE(IJK)=3.0
24     E(IJK)=1.0
25     TEM(IJK)=TINECC
26     TPS(IJK)=1.0
27 125 CONTINUE
28 C
29 C     SET LOOP FLOW
30 C
31     VINL=-1.578
32     TINL=337.1
33     J=41
34     CALL IKLIMS4
35     DO 1255 I=ILL,IUL
36     DO 1255 K=KLL,KUL

```

TABLE B-II (cont.)

```

37      CALL IJKAJCT
38      V(IJK)=VINL
39      U(IJK)=0.0
40      W(IJK)=0.0
41      BETA(IJK)=1.0
42      TE(IJK)=0.5
43      E(IJK)=0.5
44      TEM(IJK)=TINL
45      TFS(IJK)=1.0
46      1255 CONTINUE
47      2 CONTINUE
48 C
49 C      SET SPECIFIED OUTFLOW AT TOP OF CORE
50 C
51      VELOUT=0.77941
52      K=12
53      DO 126 J=2,3
54 *D,BETACAL.8,9
55      DATA (KLOW(I),I=19,21) / 19,18,17 /
56      DATA (KUP(I),I=19,21) / 25,26,27 /
57 *D,BETACAL.48,49
58      DO 415 J=5,8
59      DO 415 I=19,21
60 *D,BETACAL.58
61      DO 50 J=9,JM1
62 *D,BETACAL.62
63      IF (I.GT.6.AND.I.LT.12.AND.K.GT.19.AND.K.LT.25) GO TO 50
64 *D,BETACAL.72,74
65      J=9
66      DO 127 I=2,IM1
67      DO 127 K=2,15
68 *D,BETACAL.81
69      J=4
70 *D,BETACAL.84
71      DO 350 K=5,KUL
72 *D,BETACAL.91,93
73      K=25
74      I=9
75      DO 250 J=28,29
76 *D,BETACAL.101
77      J=42
78 *D,BETACAL.109,111
79      K=13

```



TABLE B-II (cont.)

```

80      DO 251 J=2,3
81      DO 251 I=2,IM1
82      *D,BETACAL.43
83      IF (K.EQ.KMAX.AND.J.GT.3) BETA(IJK)=0.0
84      *D,CALCIJK.13,14
85      2 1,1,6,1,1, 1,1,19,1,1, 1,4,11,1,1,
86      3 22,22,12,0,0, 13,33,25,0,0, 3,10,42,0,0 /
87      *D,SENSORS.9,28
88      DATA ZBOTCL,YVESWL,XCLCL / 89.97,14.1275,20.7772 /
89      DATA (DX(L),L=1,55) /0.0,0.0,0.0,0.0,0.0,0.0,0.0,11.10,0.0,0.0,
90      1 -11.10,4.0,11.10,0.0,0.0,-11.10,0.0,0.0,0.0,19.51,11.10,
91      2 0.0,0.0,-11.10,4.0,0.0,5.54,2.77,-2.77,-5.54,11.10,
92      3 4.0,-5.54,-11.10,0.0,0.0,0.0,0.0,5.54,-5.54,4.0,
93      4 0.0,0.0,0.0,0.0,0.0,0.0,0.0,-4.0,-4.0,-4.0,
94      5 0.0,0.0,0.0,0.0,-4.0 /
95      DATA (DY(L),L=1,55) / 11.96,11.96,11.96,11.96,11.96,0.0,
96      1 0.0,-4.13,0.0,0.0,.9527,.9527,-4.13,.9527,.9527,-4.13,.9527,
97      2 .9527,.9527,.9527,-4.13,.9527,0.0,.9527,0.0,0.0,0.0,.9527,
98      3 0.0,.9527,.9527,102.11,79.25,56.39,33.53,-4.13,-4.13,0.0,
99      4 0.0,124.97,124.97,124.97,124.97,0.0,0.0,0.0,0.0,
100     5 0.0,0.0,61.98,61.98,61.98,61.98,0.0 /
101     DATA (DZ(L),L=1,55) /0.41,2.99,6.33,9.67,12.25,-10.13,
102     1 -10.13,-12.67,-10.13,-1.0,-16.23,-16.23,-17.50,-16.23,-28.93,
103     2 -30.20,-41.63,-54.33,-54.33,-54.33,-55.60,-54.33,2.0,
104     3 -56.87,-10.13,-10.13,-10.13,-10.13,-28.93,6.0,-28.93,
105     4 -28.93,0.0,0.0,0.0,-12.67,-12.67,11.0,-1.0,0.41,
106     5 2.99,9.67,12.25,2.0,6.0,11.0,-1.0,2.0,6.0,0.41,
107     6 2.99,9.67,12.25,11.0 /
108     *D,SENSORS.82
109     J=13
110     *D,SETUP.16,19
111     J3ER11=1
112     J3ER12=9
113     J3ER21=26
114     J3ER22=31
115     *D,SOLA.193
116     J=4
117     *D,SOLA.201,203
118     FLOUTJ4=SUM
119     SUM=0.0
120     J=11
121     *D,SOLA.211,214
122     FLOUTJ11=SUM

```

TABLE B-II (cont.)

```

123      SUM=0.0
124      K=12
125      DO 492 J=2,3
126 *D,SOLA.220,223
127      FLOUTK12=SUM
128      SUM=0.0
129      K=17
130      DO 498 J=5,8
131 *D,SOLA.230
132      FLOUTK17=SUM
133 *D,SOLA.233
134      1 , FLOUTJ4, FLOUTJ11, FLOUTK12, FLOUTK17
135 *D,SOLA.259,261
136      1 7H DELT=,E12.5,8H EPSI=,E12.5/ 9H FLOUTJ4=,E12.5,
137      2 10H FLOUTJ11=,E12.5,10H FLOUTK12=,E12.5,
138      3 10H FLOUTK17=,E12.5)
139 *D,TILDE.236
140      IF(J.EQ.18) VLAG(IJK)=VLAG(IJK)-1.0E-3*DELT*ABS(VN(IJK))*VN(IJK)
141      1 *RDYP(J)
142 *D,TILDE.372,374
143      K=12
144      DO 900 J=2,3
145      DO 900 I=2,IM1
146 *D,TILDE.378,380
147      K=23
148      I=9
149      DO 905 J=28,29
150 *D,TILDE.385
151      J=40
152 *I,TURE.51
153      IF(J.EQ.4.AND.BETA(IJKP).LE.0.0) DWEDF=0.5*DWEDF

```

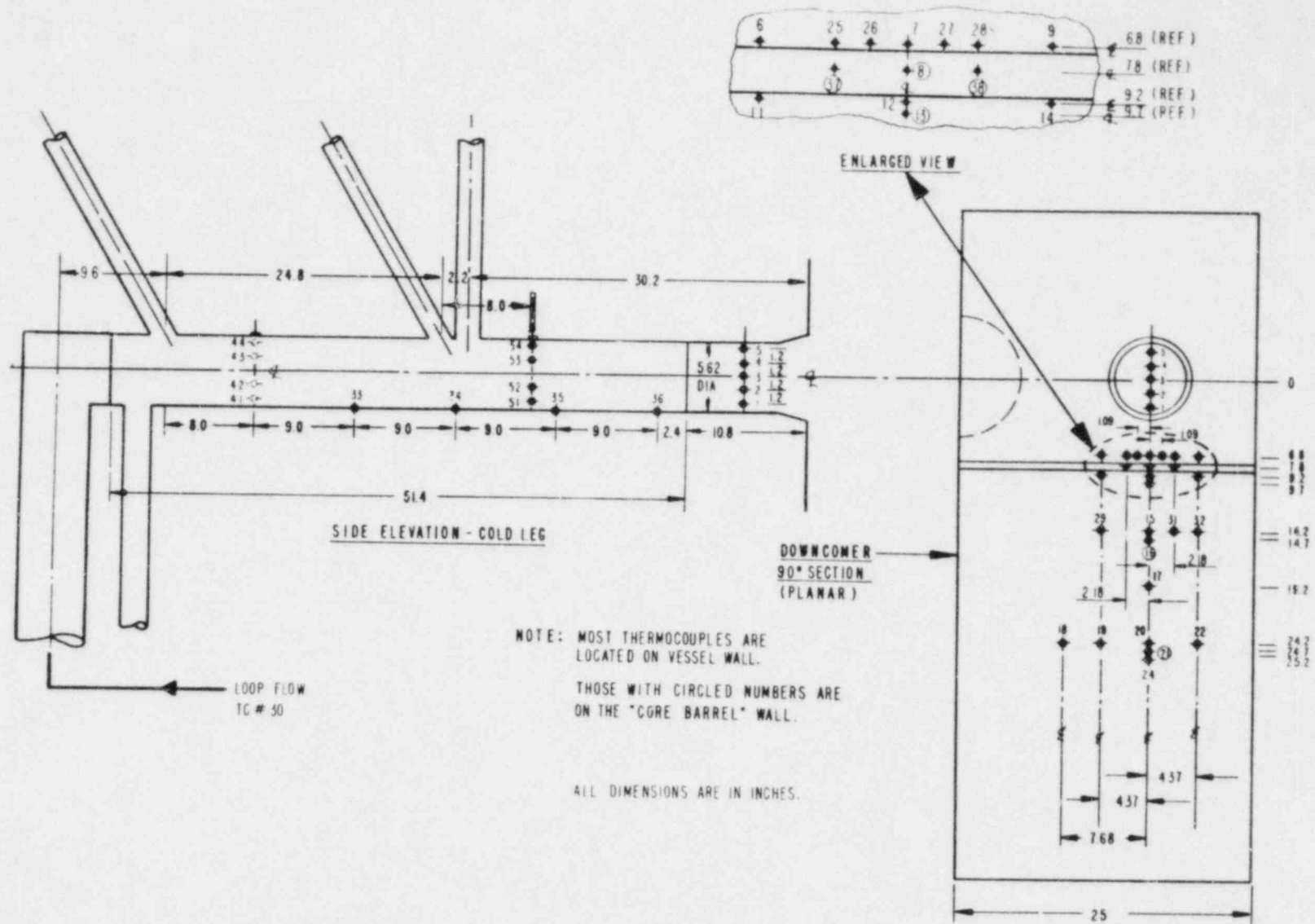


Fig. 1. Creare cold leg and downcomer configurations showing thermocouple locations and various HPI inlet pipes. The dashed semicircle in the downcomer marks the hot leg obstacle, while the pair of horizontal lines show the top of an expansion in the lower part of the downcomer. This figure is reprinted from reference 11.

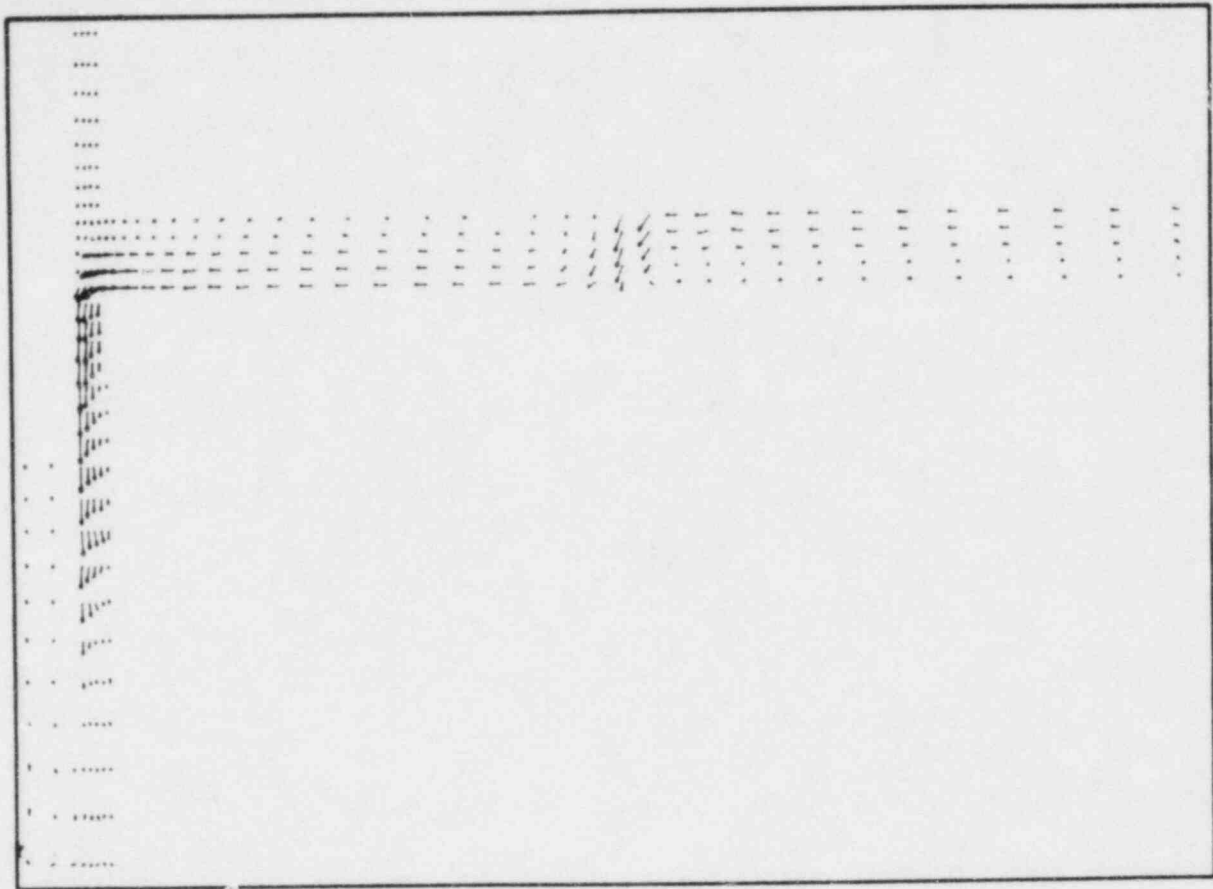


Fig. 2. A velocity vector plot in a vertical plane through the centerline of the cold leg from a calculation of Creare experiment 51 at 100 s. Included in the plot are the cold leg, downcomer, lower plenum, and core. The HPI fluid enters the cold leg where it mixes with the loop flow and then flows as a stratified layer along the bottom of the cold leg to the downcomer.

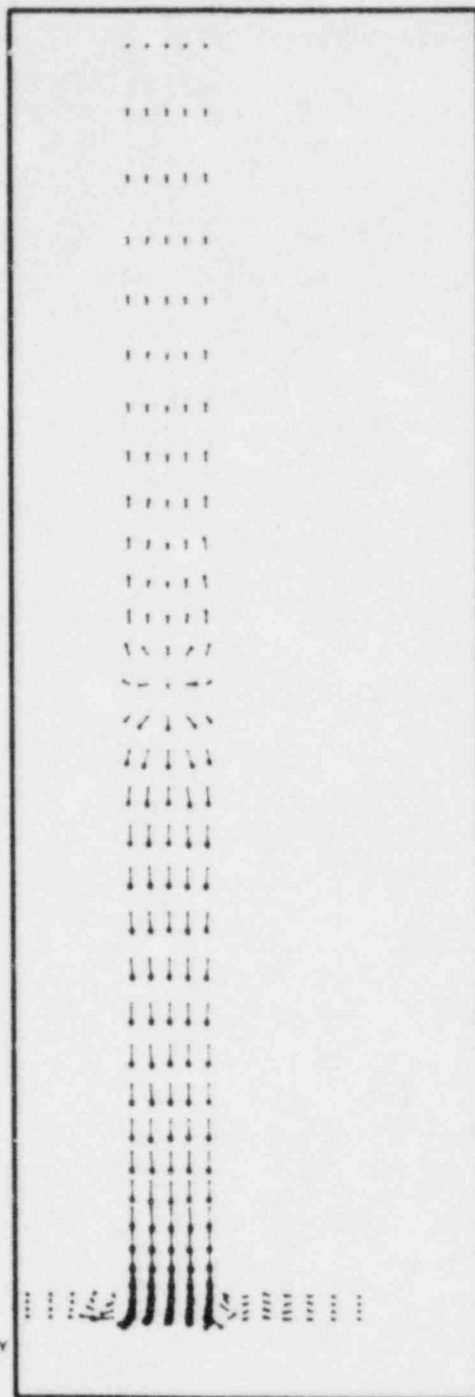


Fig. 3. A velocity vector plot in a horizontal plane through the bottom of the cold leg from a calculation of Creare experiment 51 at 100 s. The HPI jet impacts on the bottom of the cold leg and fluid spreads upstream and downstream from the impaction point. The cold fluid layer at the bottom of the cold leg impacts on the core barrel wall in the downcomer. The blank region on the right in the downcomer is the hot leg obstacle.

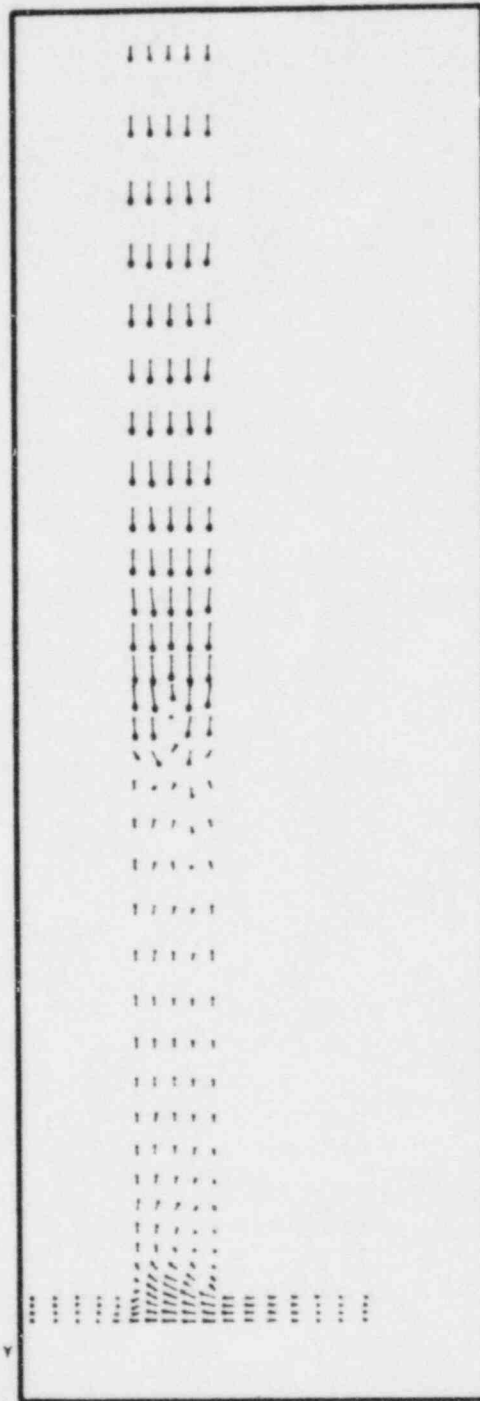


Fig. 4. A velocity vector plot in a horizontal plane through the top of the cold leg from a calculation of Creare experiment 51 at 100 s. Fluid flows toward the HPI inlet from the loop flow entrance at the top of the plot and as entrained fluid from the downcomer at the bottom.

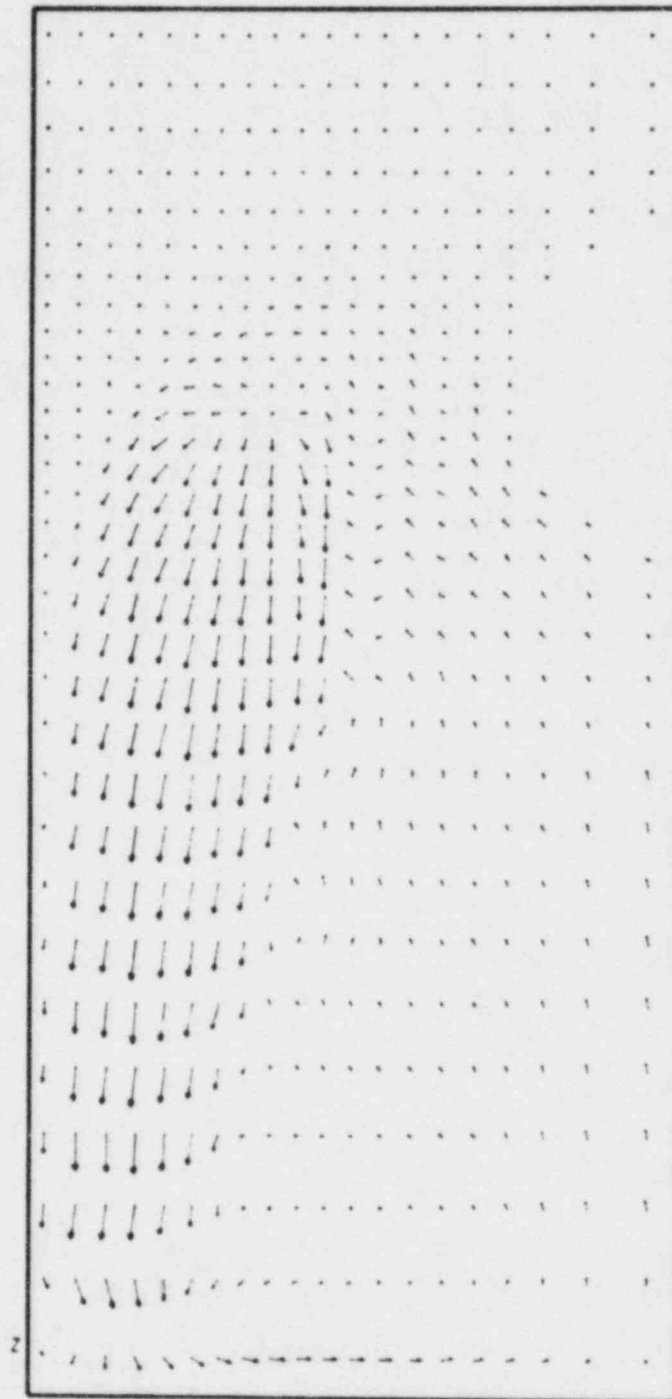


Fig. 5. A velocity vector plot in a vertical plane parallel and adjacent to the core barrel wall from a calculation of Creare experiment 51 at 100 s. The cold fluid from the bottom of the cold leg impacts on this surface, spreads, and then falls as a plume to the lower plenum. The blank region at the upper right is the hot leg obstacle.

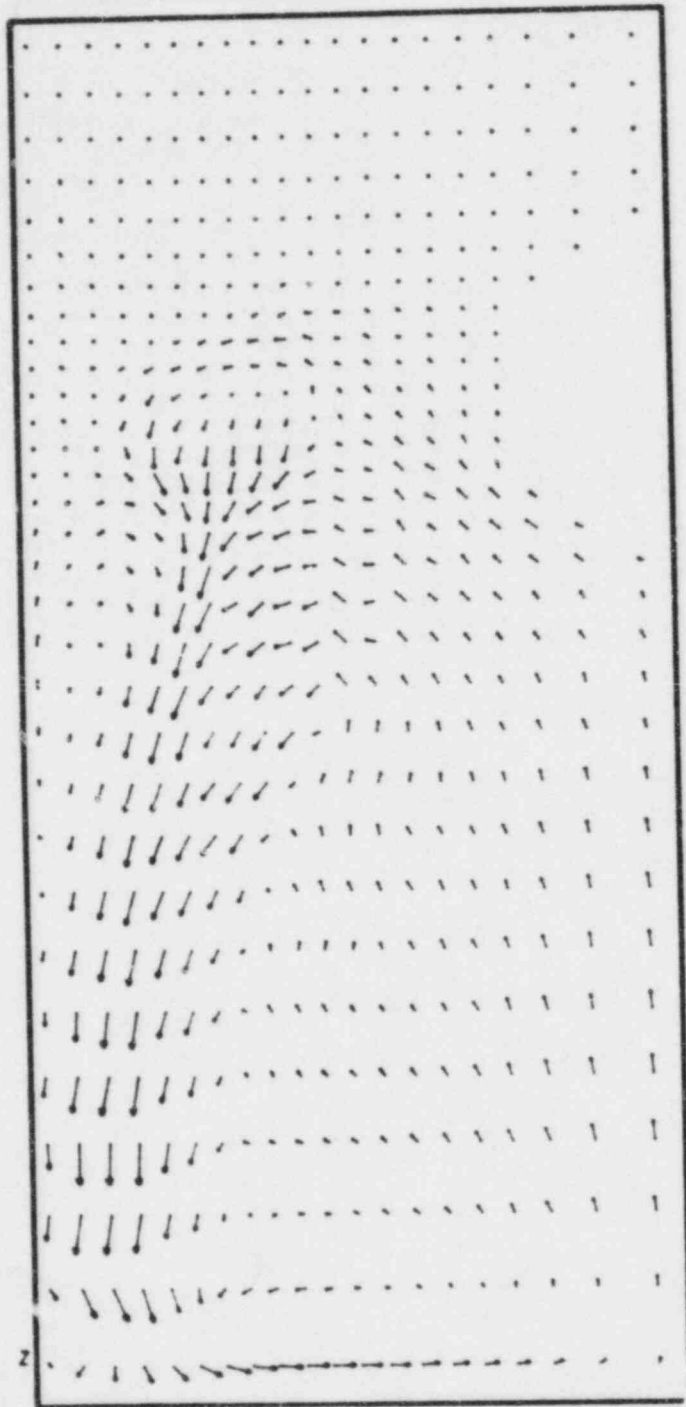


Fig. 6. A velocity vector plot in a vertical plane parallel and adjacent to the vessel wall from a calculation of Creare experiment 51 at 100 s. Warm recirculating water is entrained into the cold water plume so its temperature is rapidly reduced with depth in the downcomer.



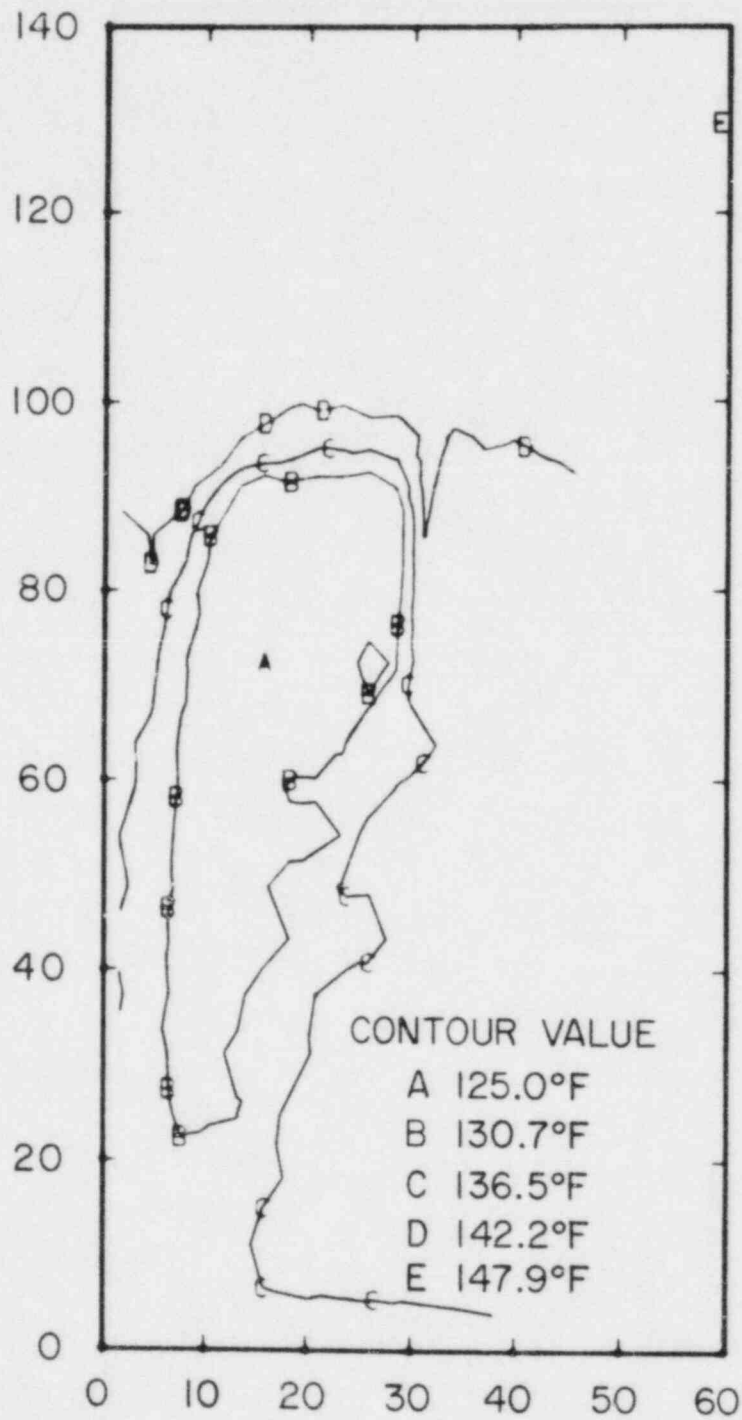


Fig. 7. A temperature contour plot in a vertical plane parallel and adjacent to the core barrel wall from a calculation of Creare experiment 51 at 100 s. Fluid flows from the cold leg junction to the bottom of the downcomer along this wall without appreciable warming. The region at the top of the downcomer is a hot stagnant zone.

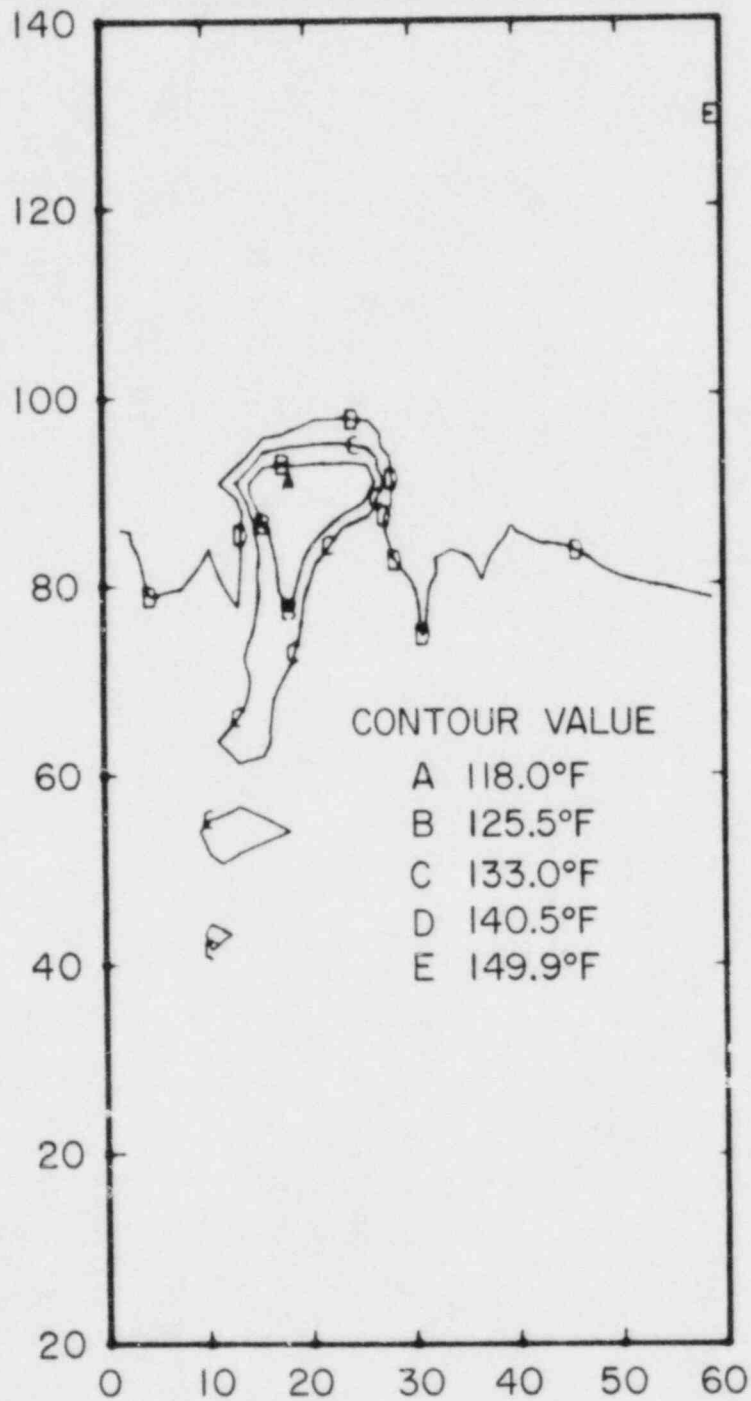


Fig. 8. A temperature contour plot in a vertical plane parallel and adjacent to the vessel wall from a calculation of Creare experiment 51 at 100 s. More mixing with warm water occurs here than on the core barrel wall so the cold water does not penetrate as far into the downcomer.

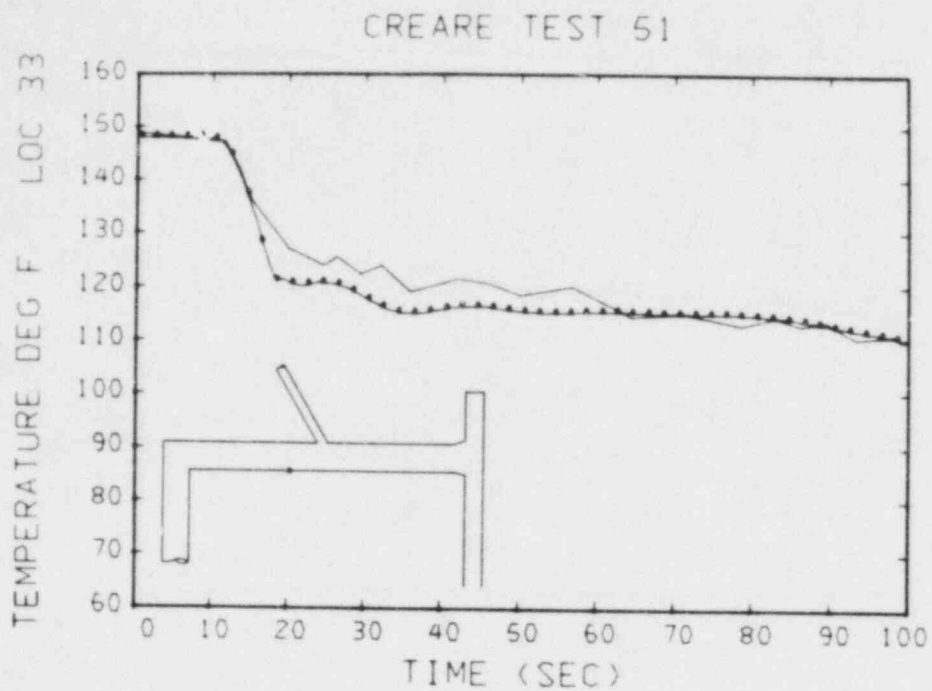


Fig. 9. Comparison between calculated (the datum points) and measured temperature at thermocouple 33.

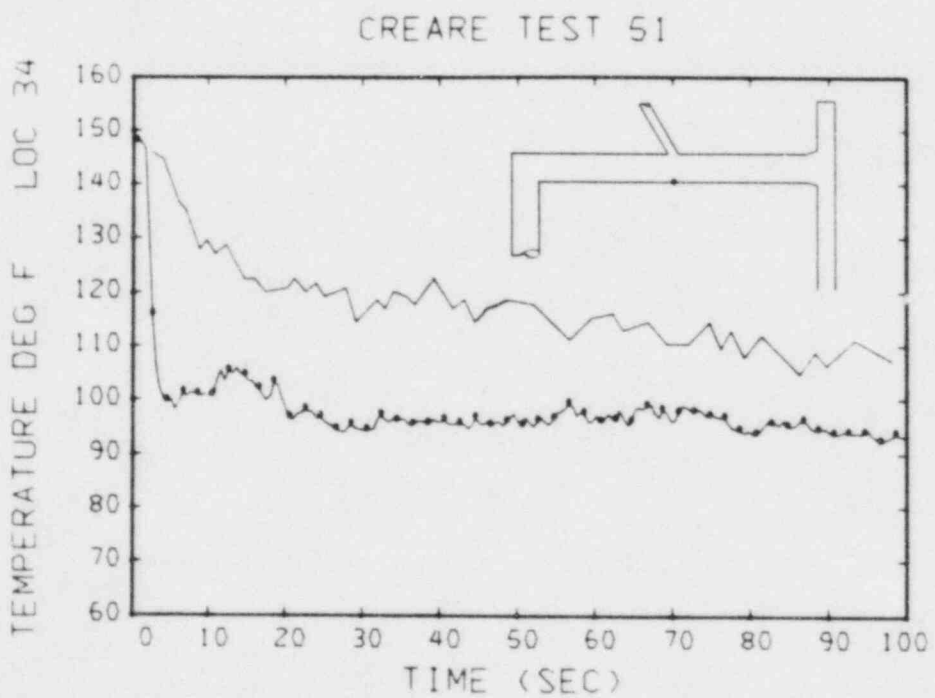


Fig. 10. Comparison between calculated (the datum points) and measured temperature at thermocouple 34.

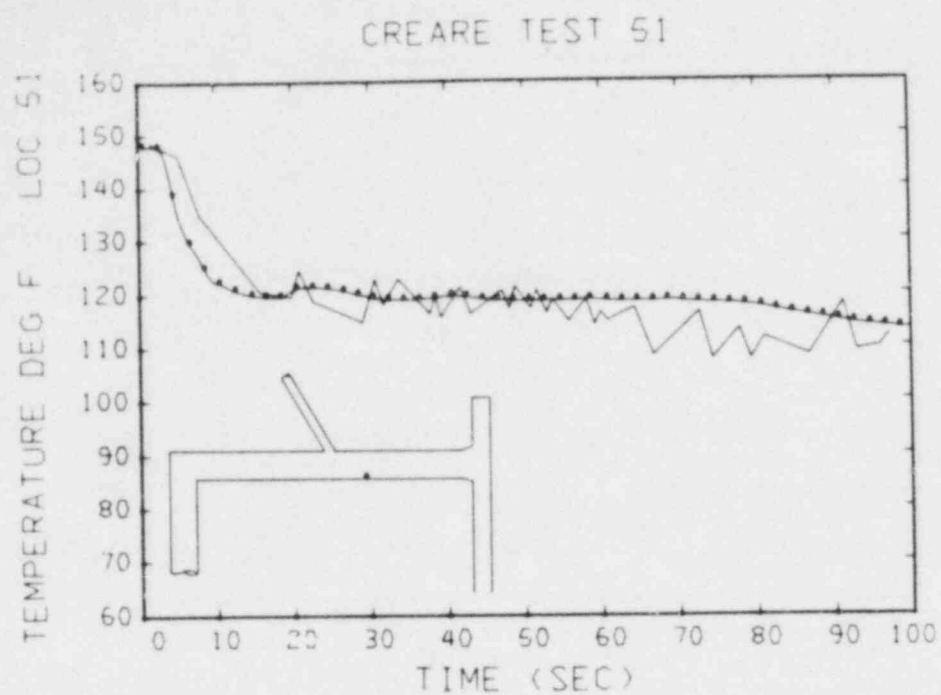


Fig. 11. Comparison between calculated (the datum points) and measured temperature at thermocouple 51.

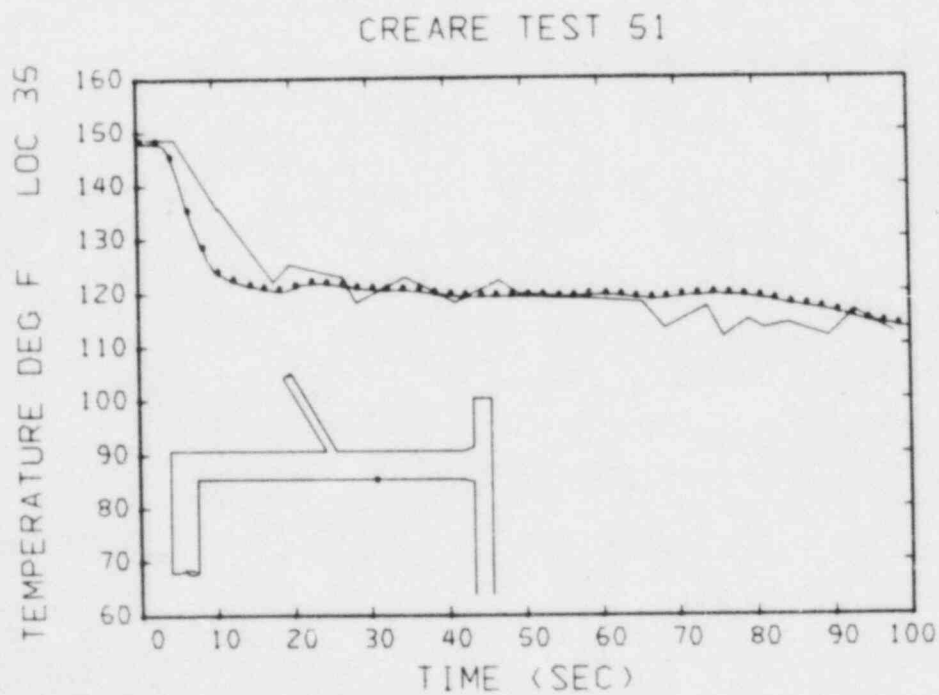


Fig. 12. Comparison between calculated (the datum points) and measured temperature at thermocouple 35.

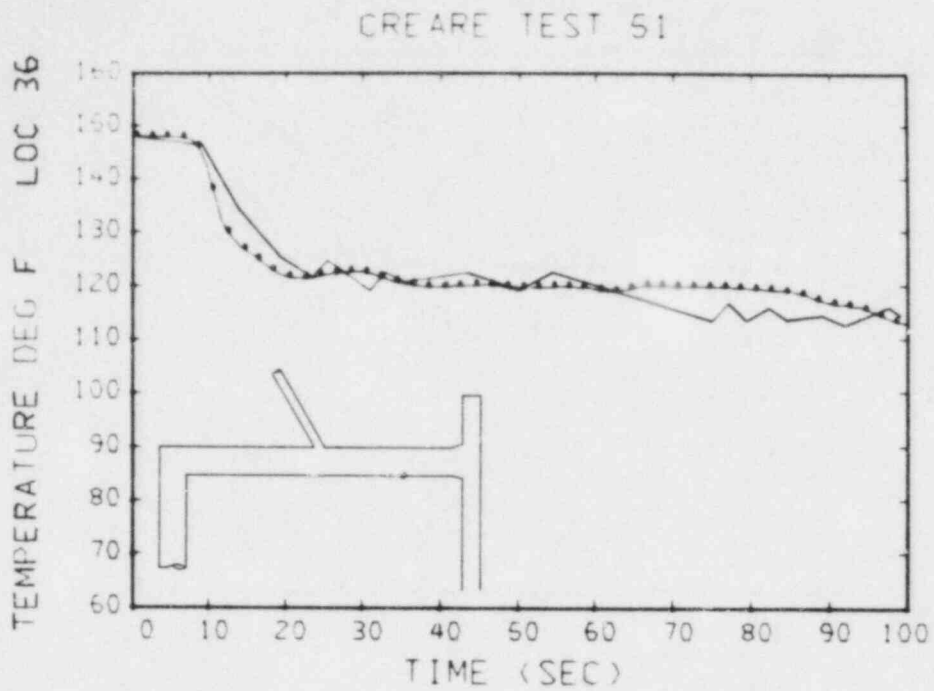


Fig. 13. Comparison between calculated (the datum points) and measured temperature at thermocouple 36.

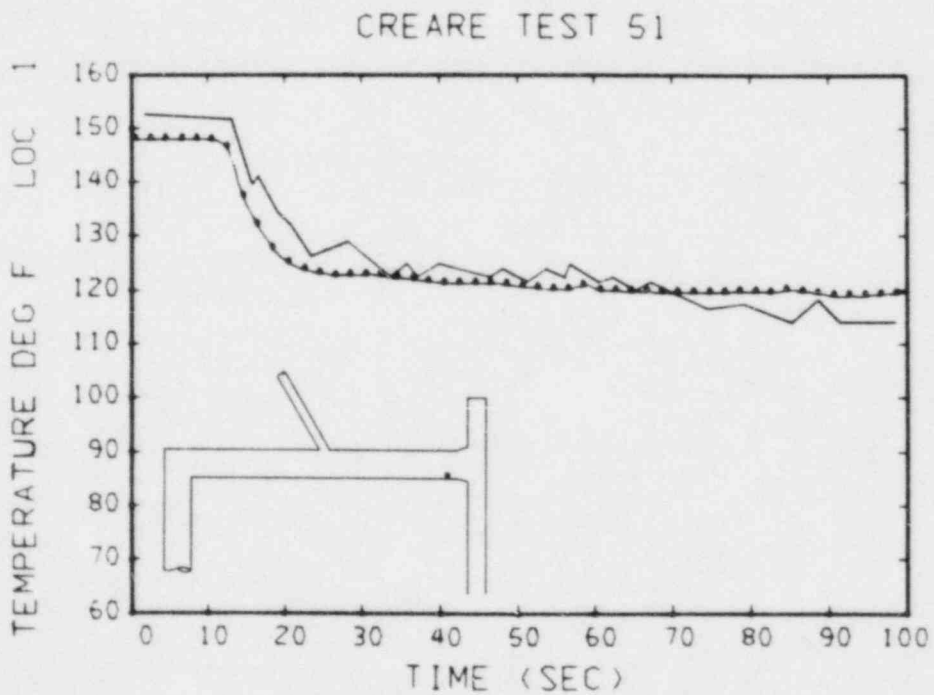


Fig. 14. Comparison between calculated (the datum points) and measured temperature at thermocouple 1.

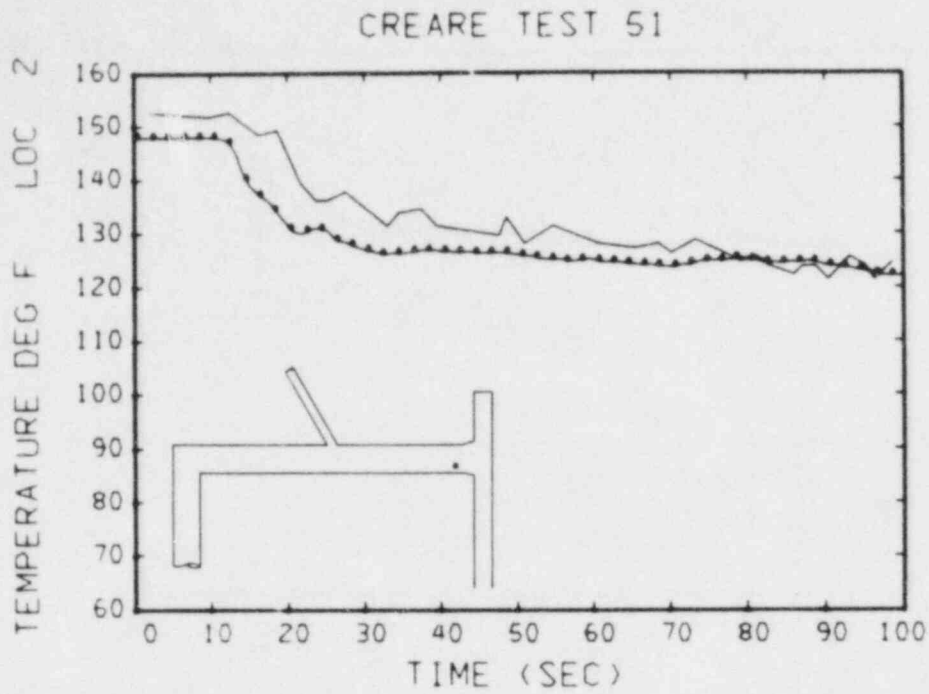


Fig. 15. Comparison between calculated (the datum points) and measured temperature at thermocouple 2.

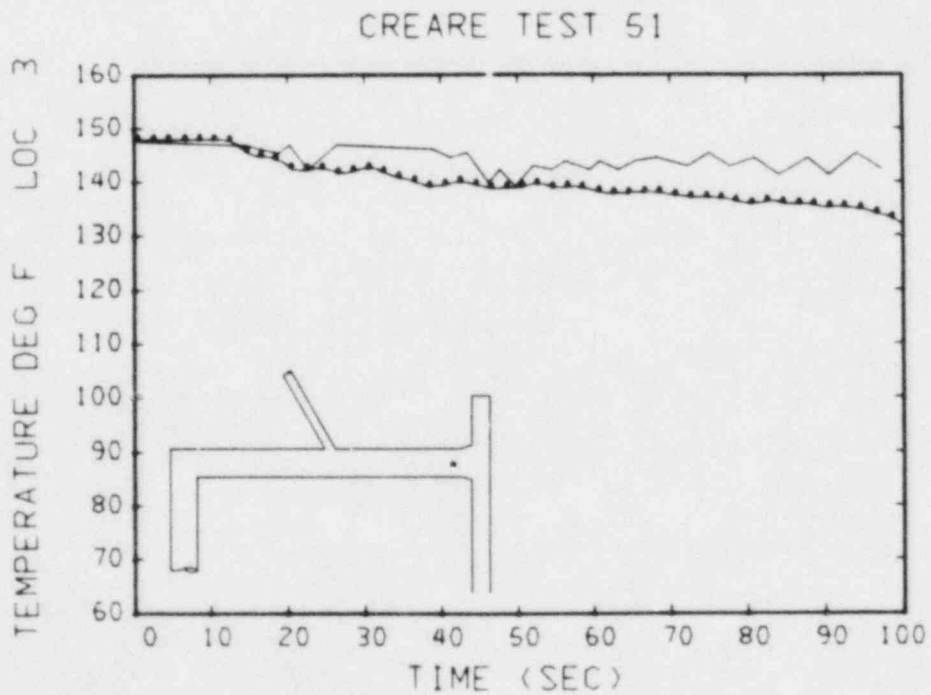


Fig. 16. Comparison between calculated (the datum points) and measured temperature at thermocouple 3.

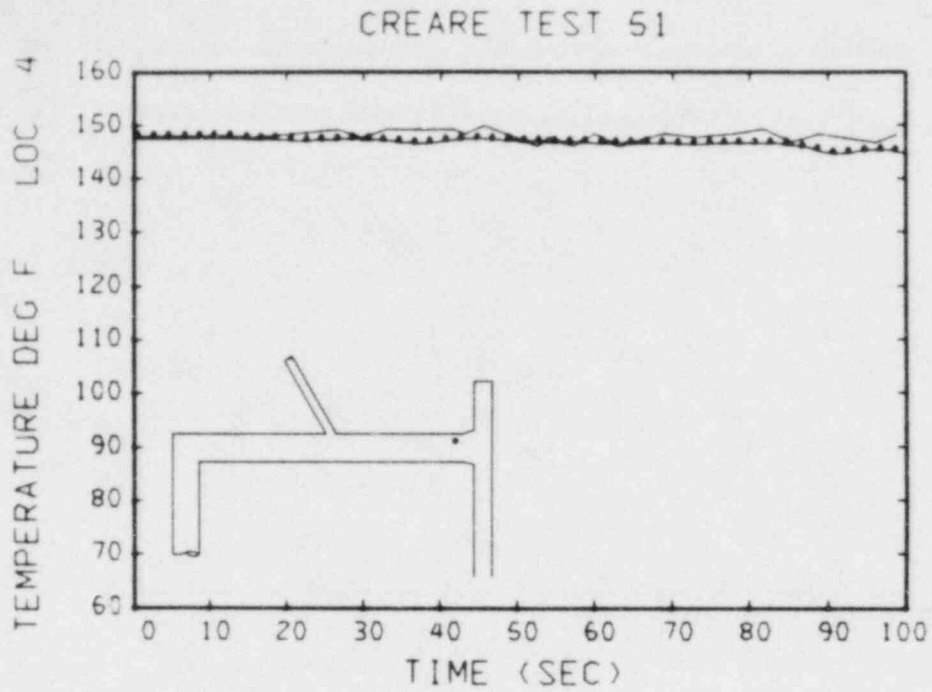


Fig. 17. Comparison between calculated (the datum points) and measured temperature at thermocouple 4.

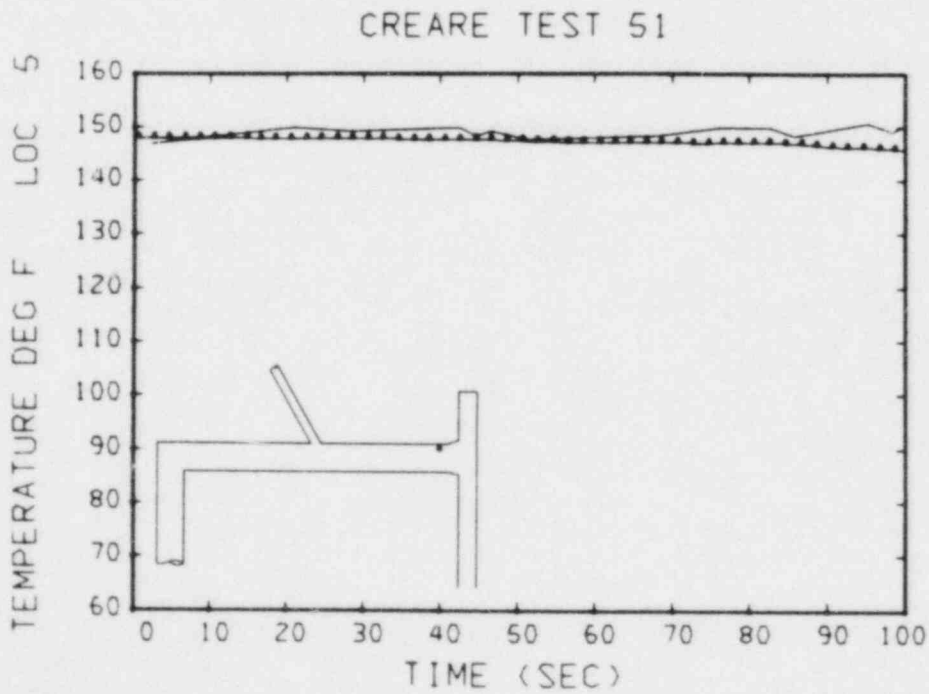


Fig. 18. Comparison between calculated (the datum points) and measured temperature at thermocouple 5.

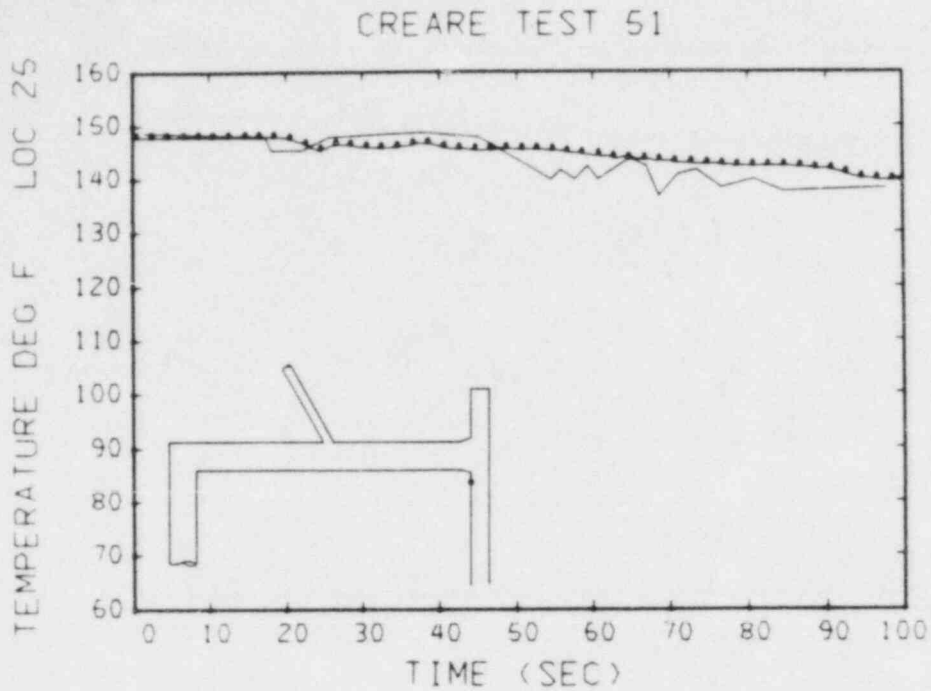


Fig. 19. Comparison between calculated (the datum points) and measured temperature at thermocouple 25.

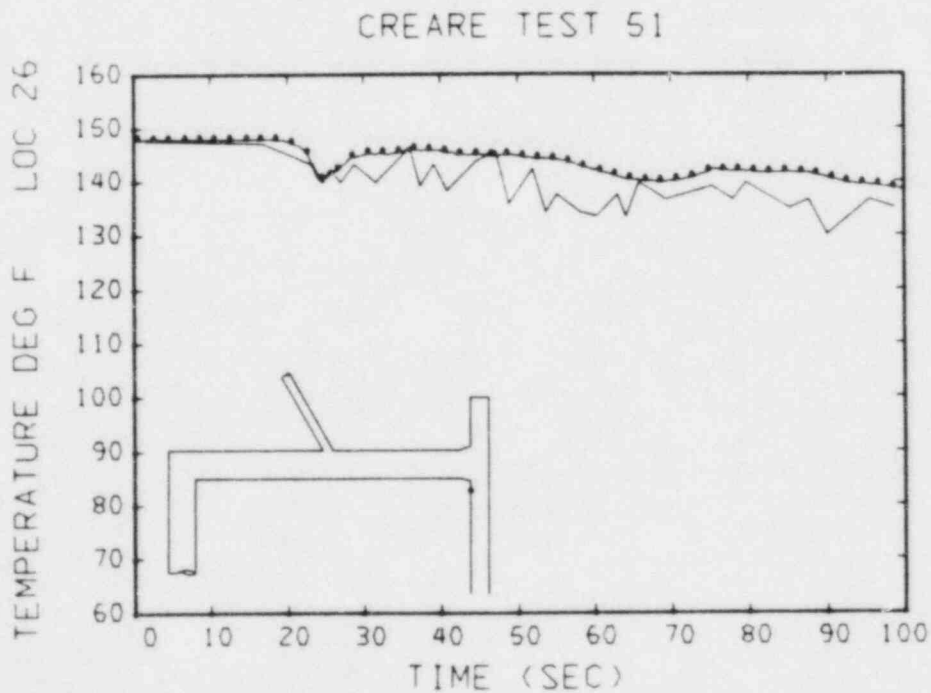


Fig. 20. Comparison between calculated (the datum points) and measured temperature at thermocouple 26.



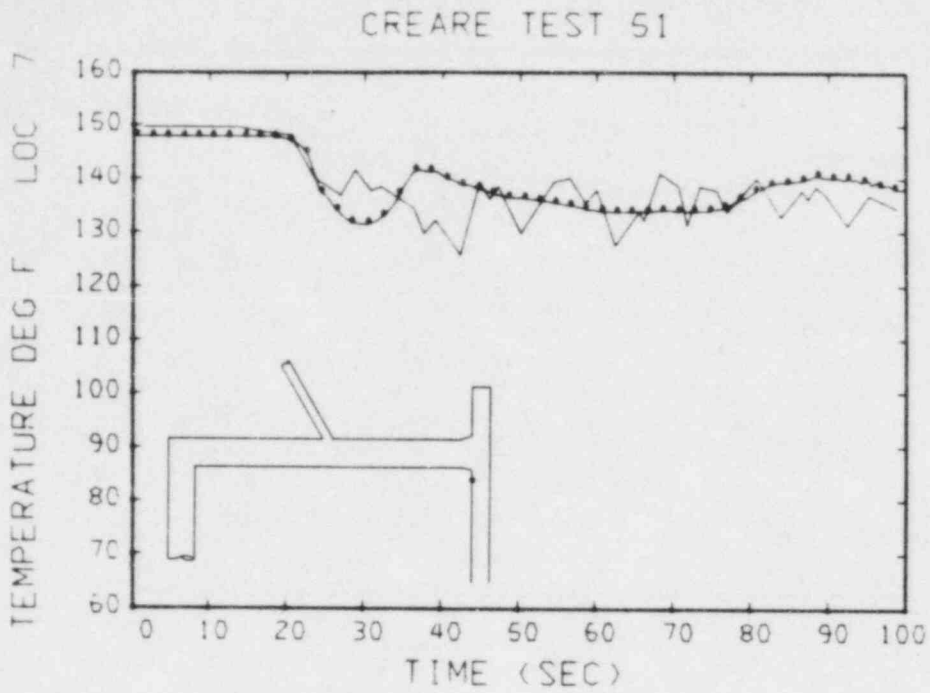


Fig. 21. Comparison between calculated (the datum points) and measured temperature at thermocouple 7.

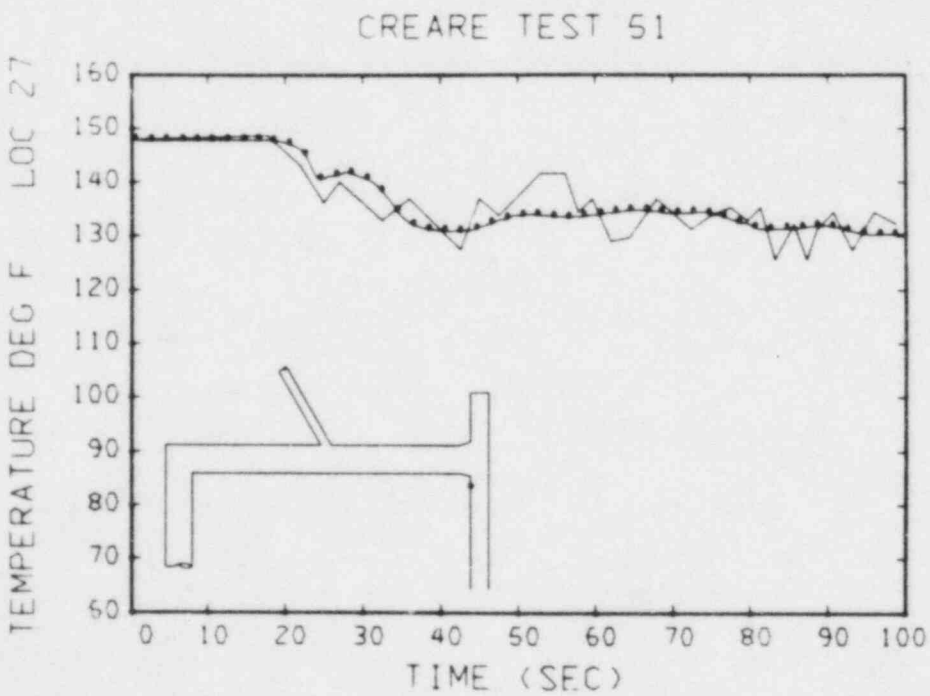


Fig. 22. Comparison between calculated (the datum points) and measured temperature at thermocouple 27.

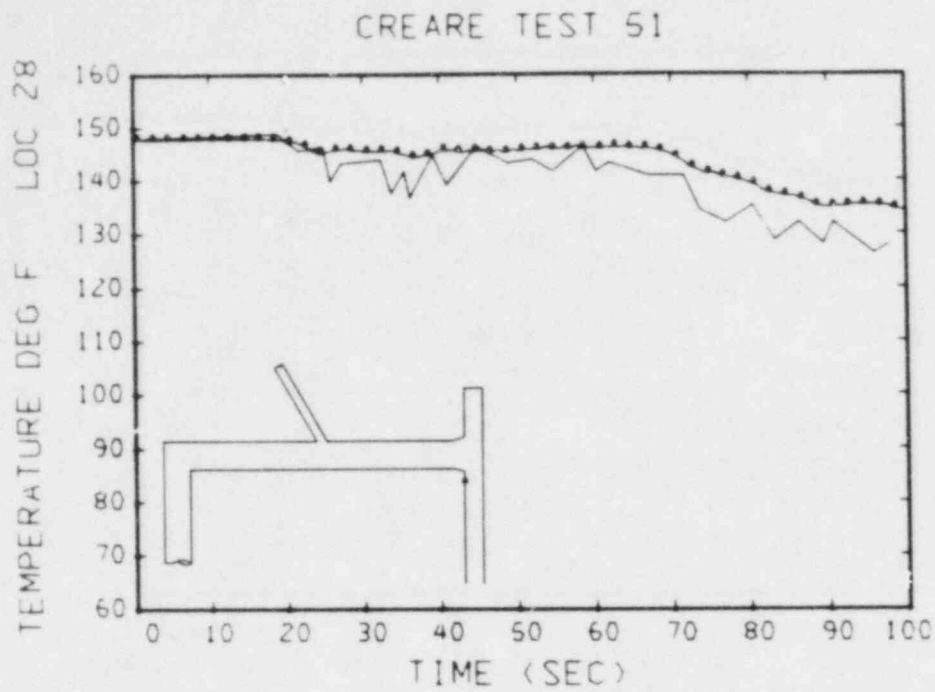


Fig. 23. Comparison between calculated (the datum points) and measured temperature at thermocouple 28.

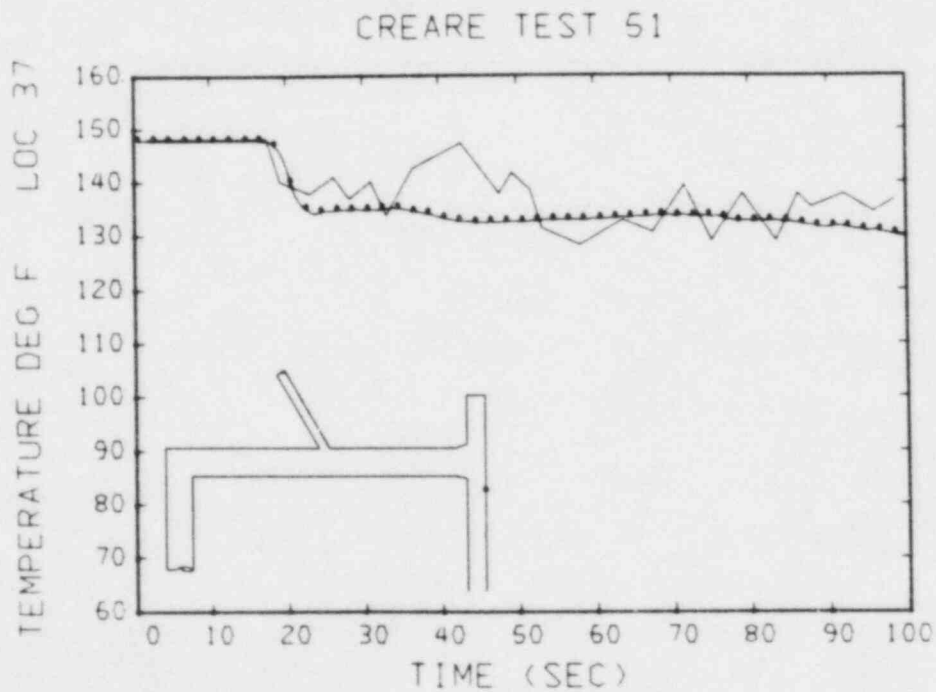


Fig. 24. Comparison between calculated (the datum points) and measured temperature at thermocouple 37.

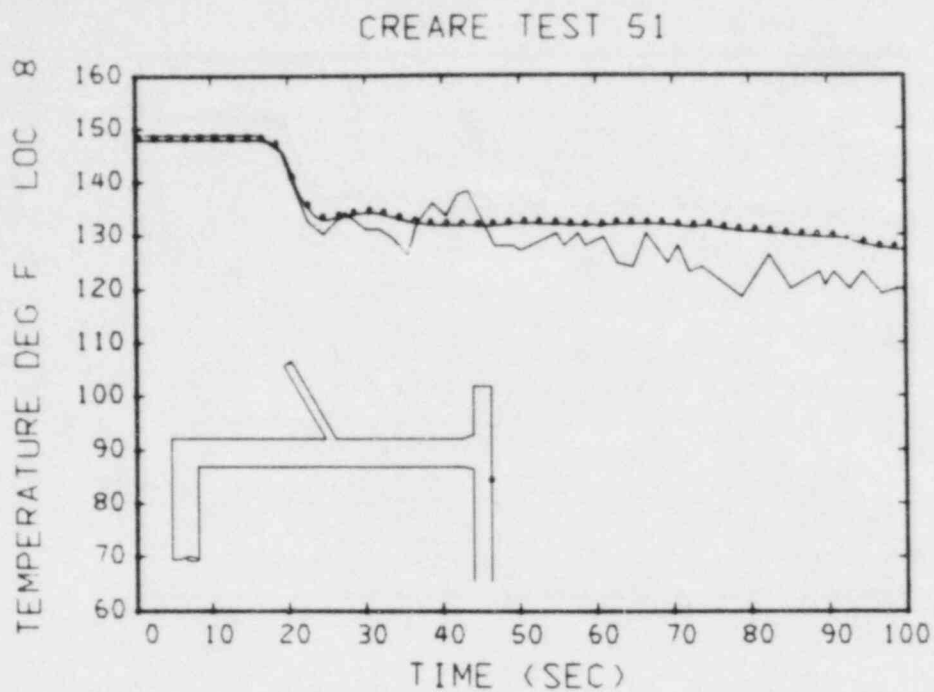


Fig. 25. Comparison between calculated (the datum points) and measured temperature at thermocouple 8.

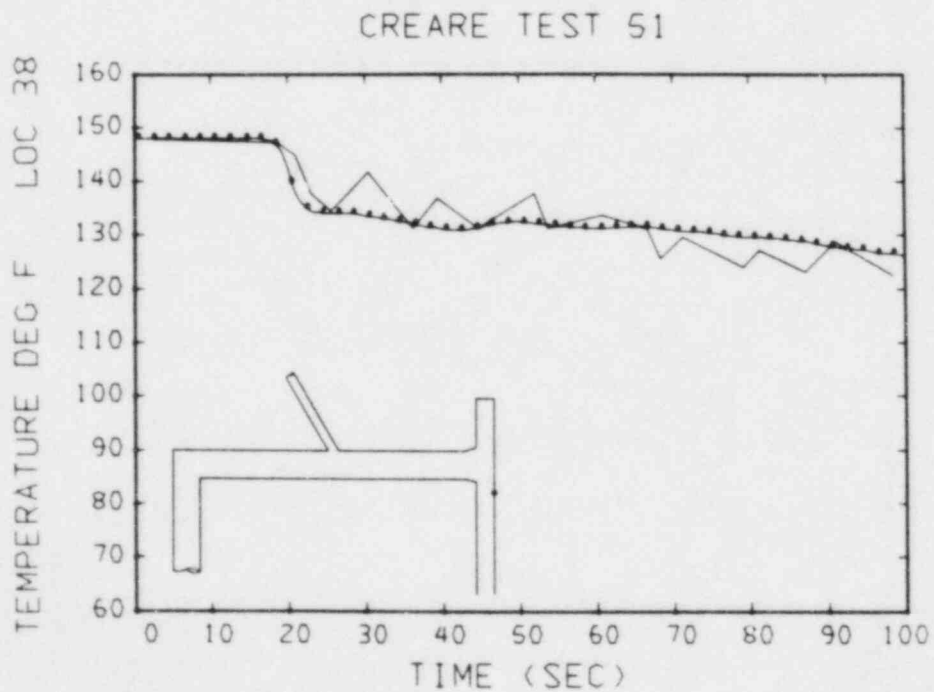


Fig. 26. Comparison between calculated (the datum points) and measured temperature at thermocouple 38.

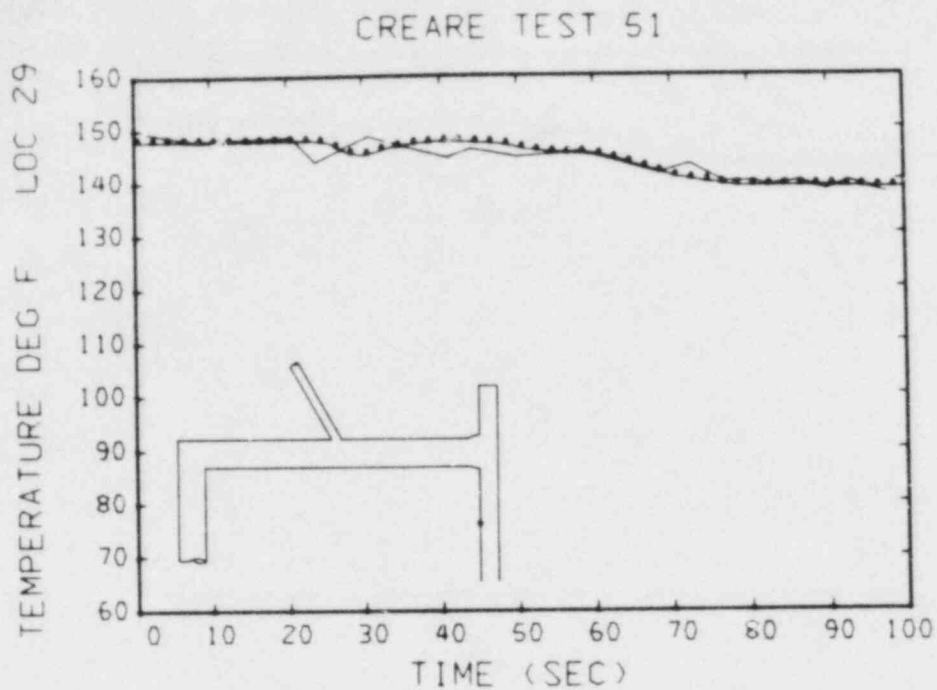


Fig. 27. Comparison between calculated (the datum points) and measured temperature at thermocouple 29.

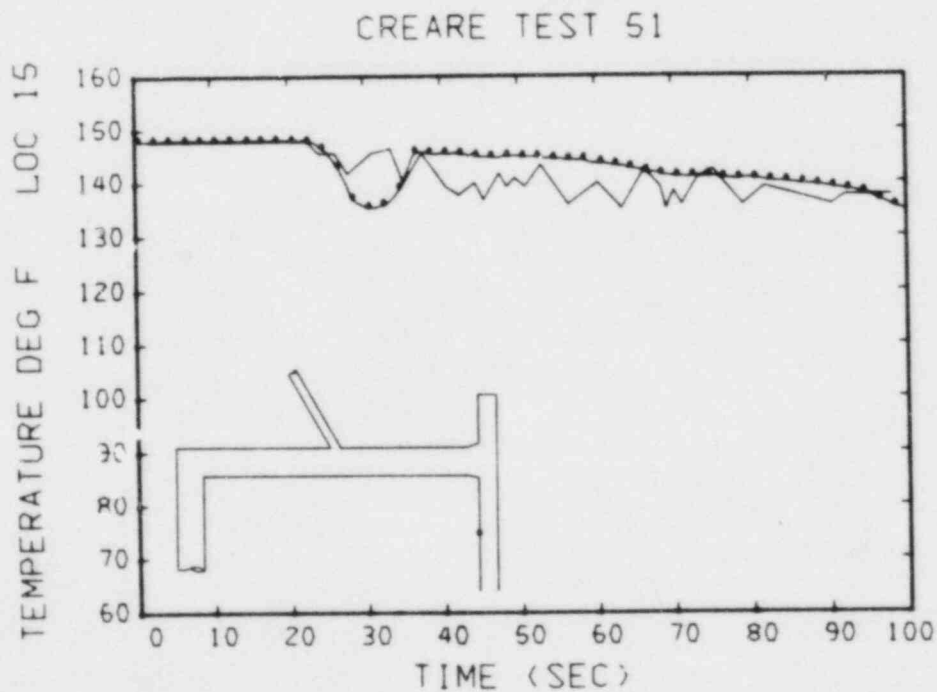


Fig. 28. Comparison between calculated (the datum points) and measured temperature at thermocouple 15.

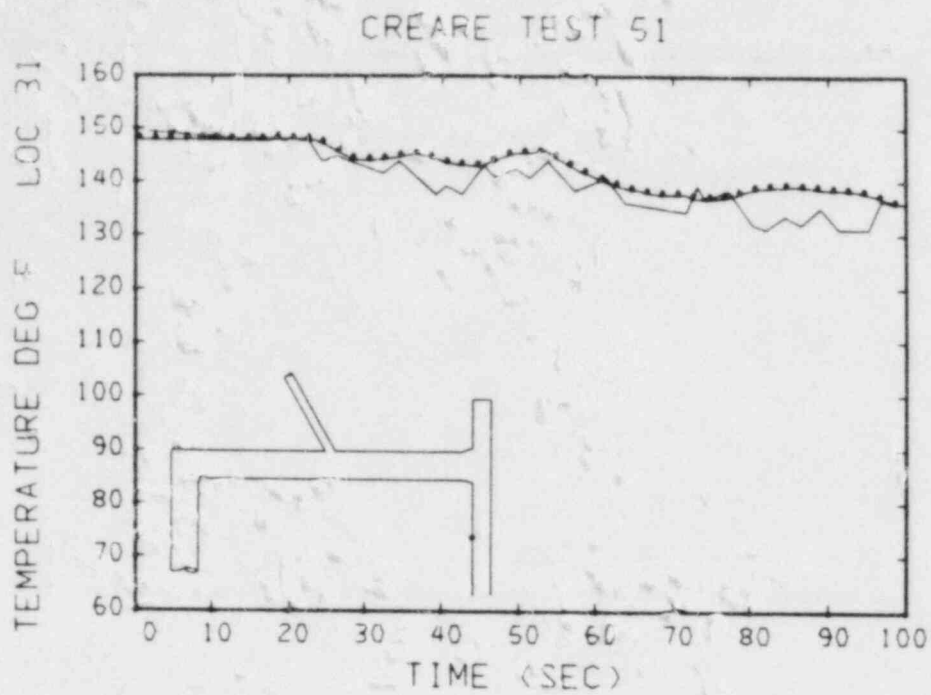


Fig. 29. Comparison between calculated (the datum points) and measured temperature at thermocouple 31.

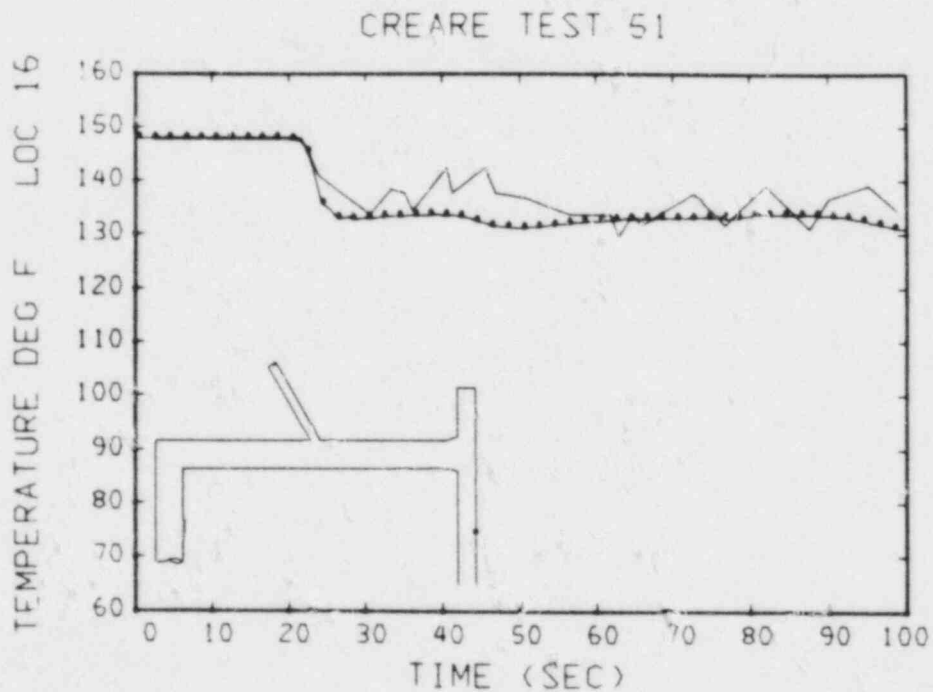


Fig. 30. Comparison between calculated (the datum points) and measured temperature at thermocouple 16.

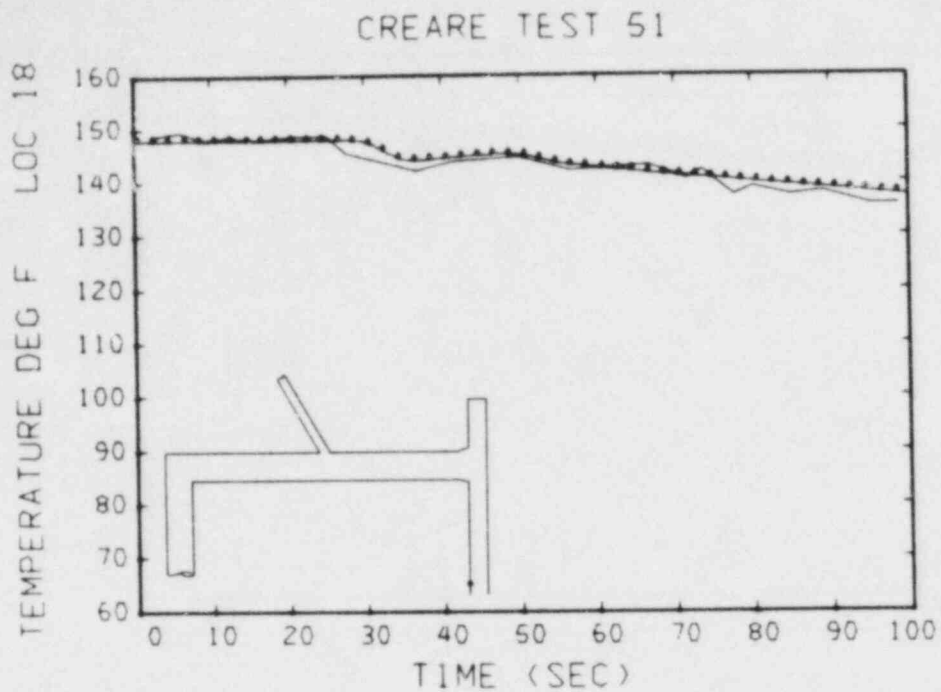


Fig. 31. Comparison between calculated (the datum points) and measured temperature at thermocouple 18.

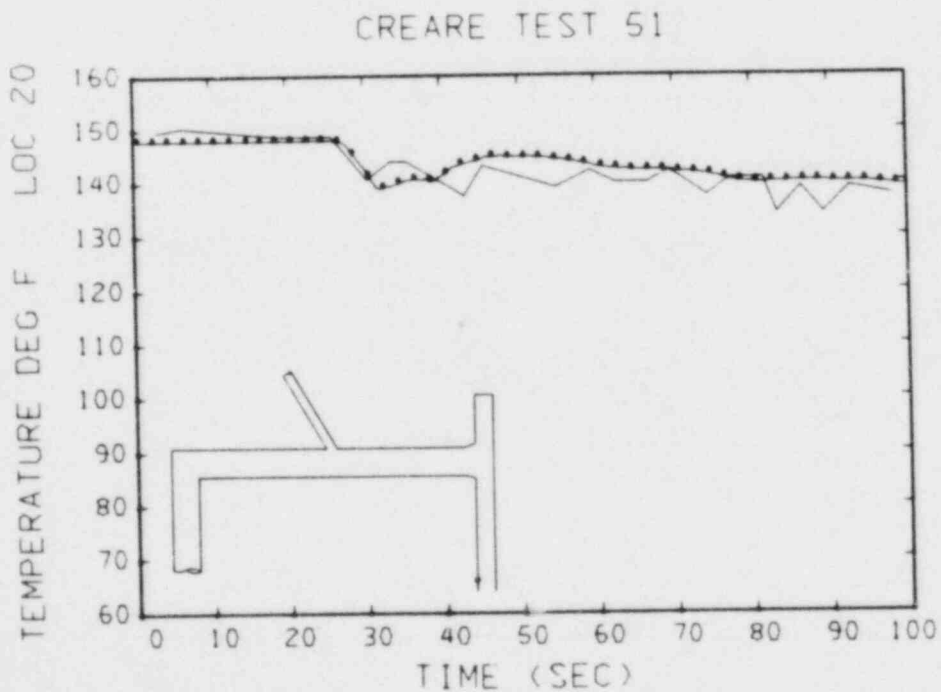


Fig. 32. Comparison between calculated (the datum points) and measured temperature at thermocouple 20.

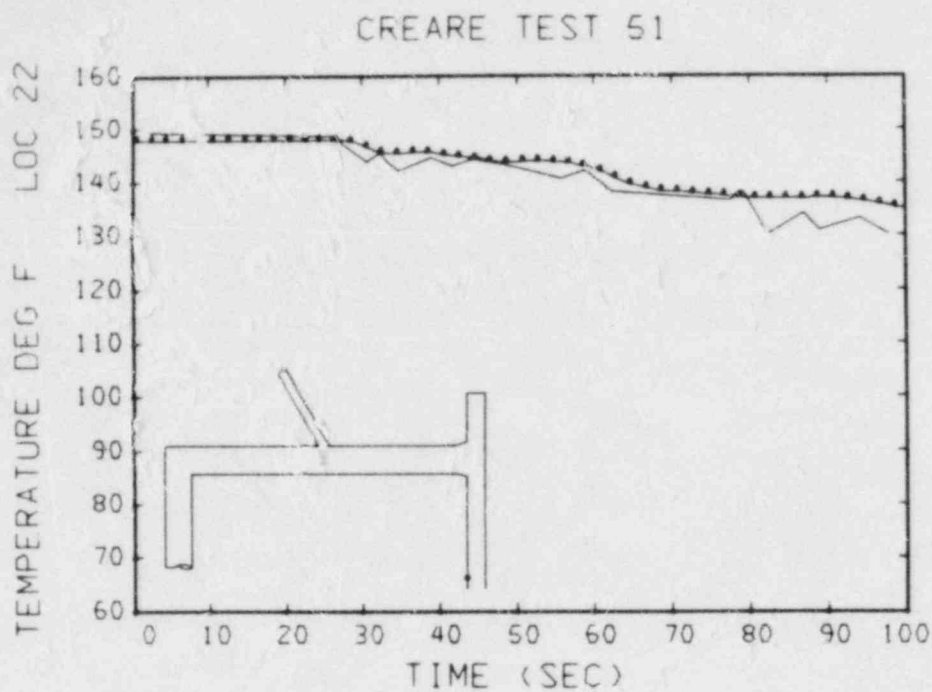


Fig. 33. Comparison between calculated (the datum points) and measured temperature at thermocouple 22.

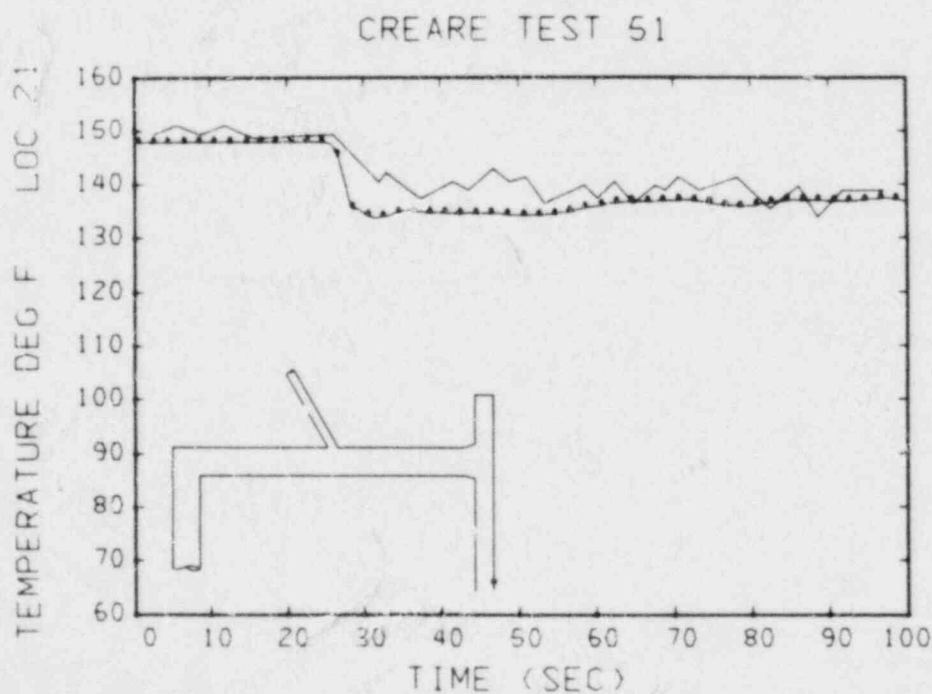


Fig. 34. Comparison between calculated (the datum points) and measured temperature at thermocouple 21.

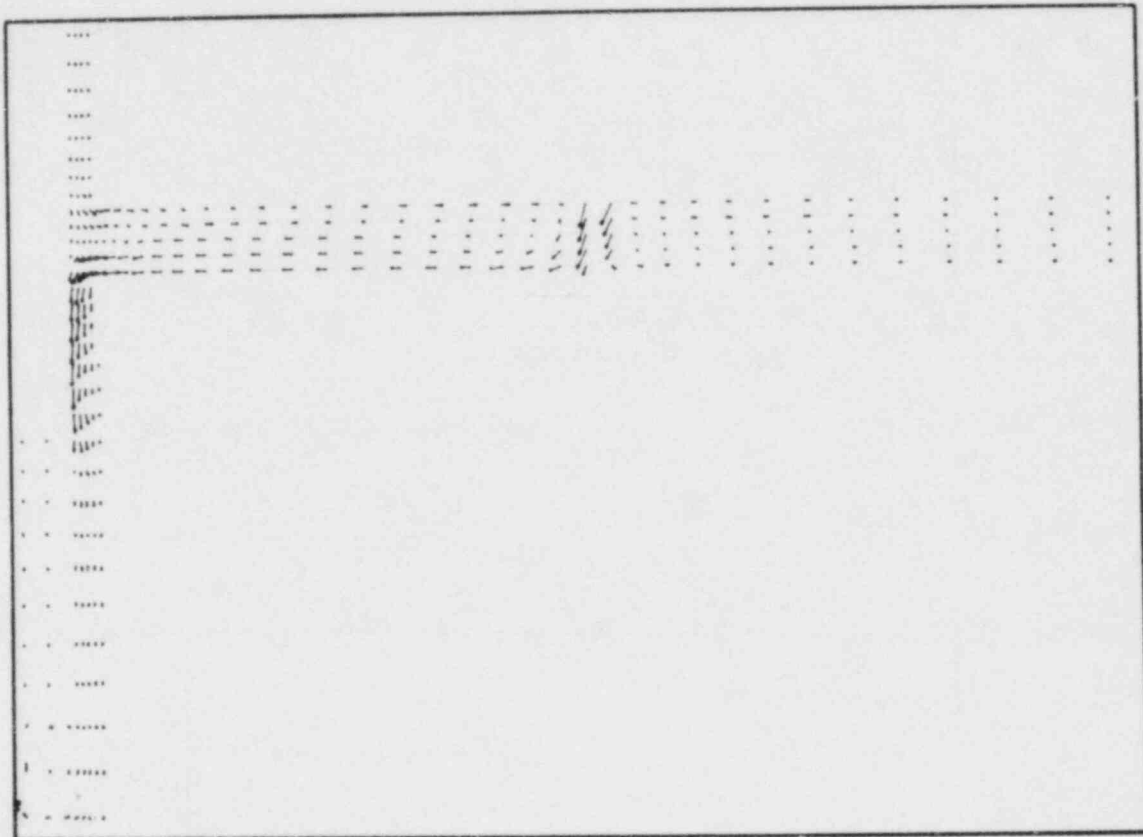


Fig. 35. A velocity vector plot in a vertical plane through the centerline of the cold leg from a calculation of Creare experiment 50 at 100 s. The cold water plume in the downcomer has been diverted azimuthally and thus appears to stagnate in this vertical cut.



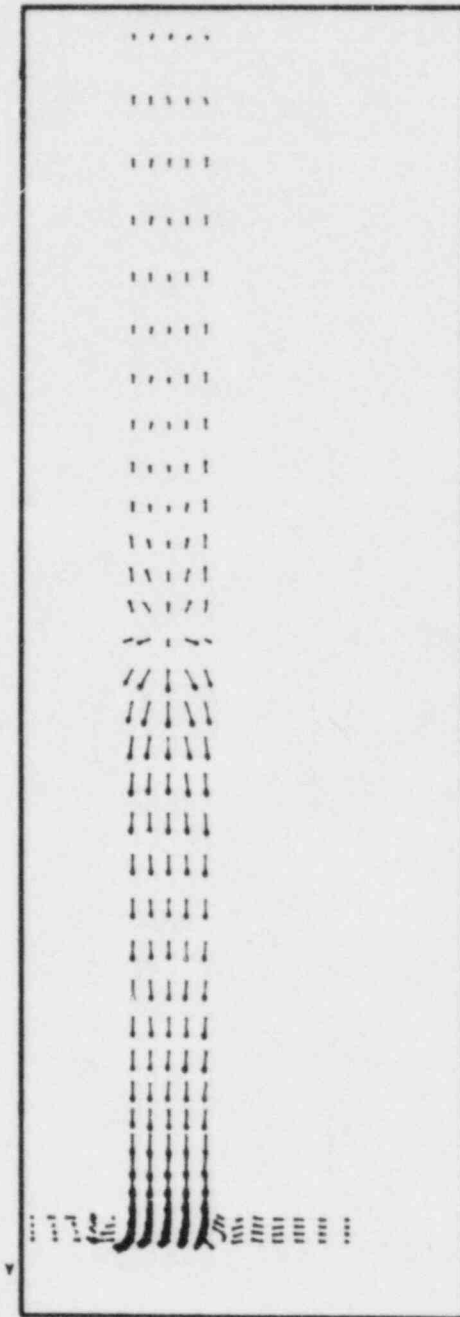


Fig. 36. A velocity vector plot in a horizontal plane through the bottom of the cold leg from a calculation of Creare experiment 50 at 100 s.

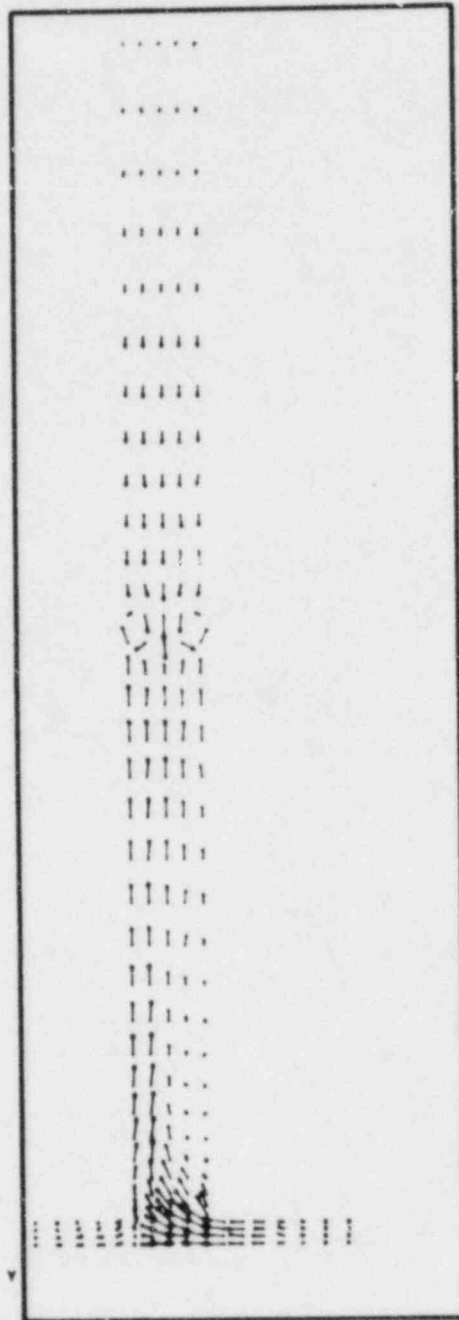


Fig. 37. A velocity vector plot in a horizontal plane through the top of the cold leg from a calculation of Creare experiment 50 at 100 s. Azimuthally flowing fluid from the downcomer is entrained into the cold leg.

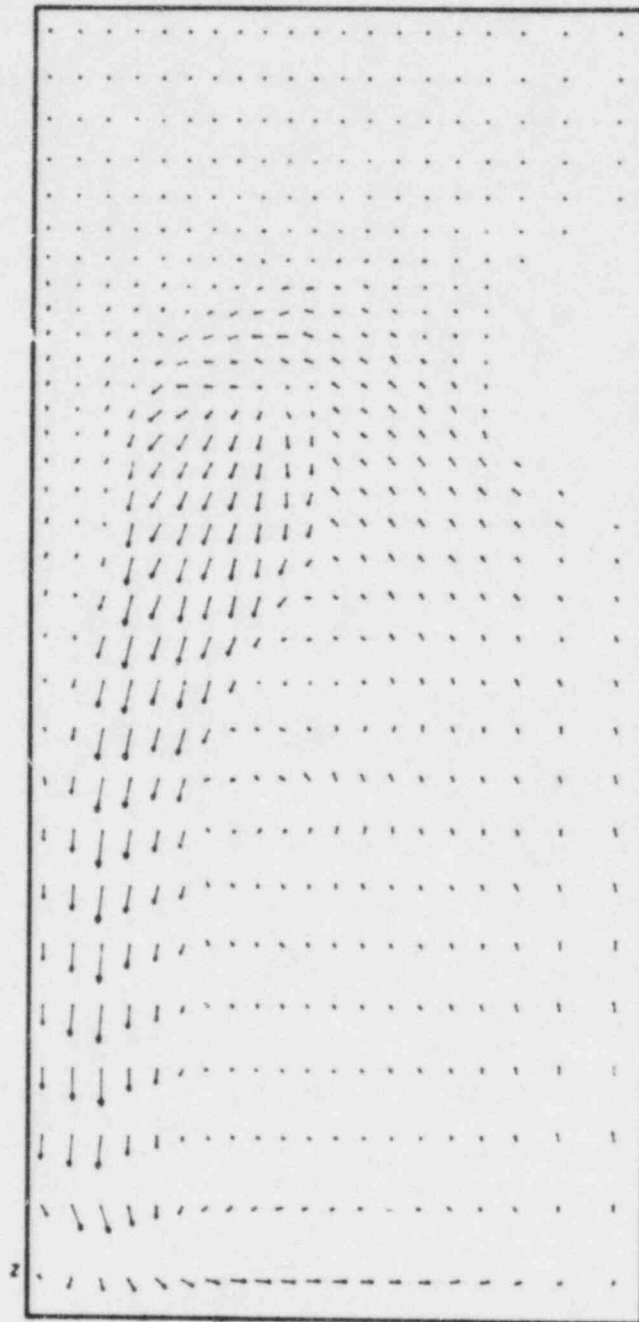


Fig. 38. A velocity vector plot in a vertical plane parallel and adjacent to the core barrel wall from a calculation of Creare experiment 50 at 100 s. The cold water plume is experiencing a strong azimuthal displacement at this time in the transient.

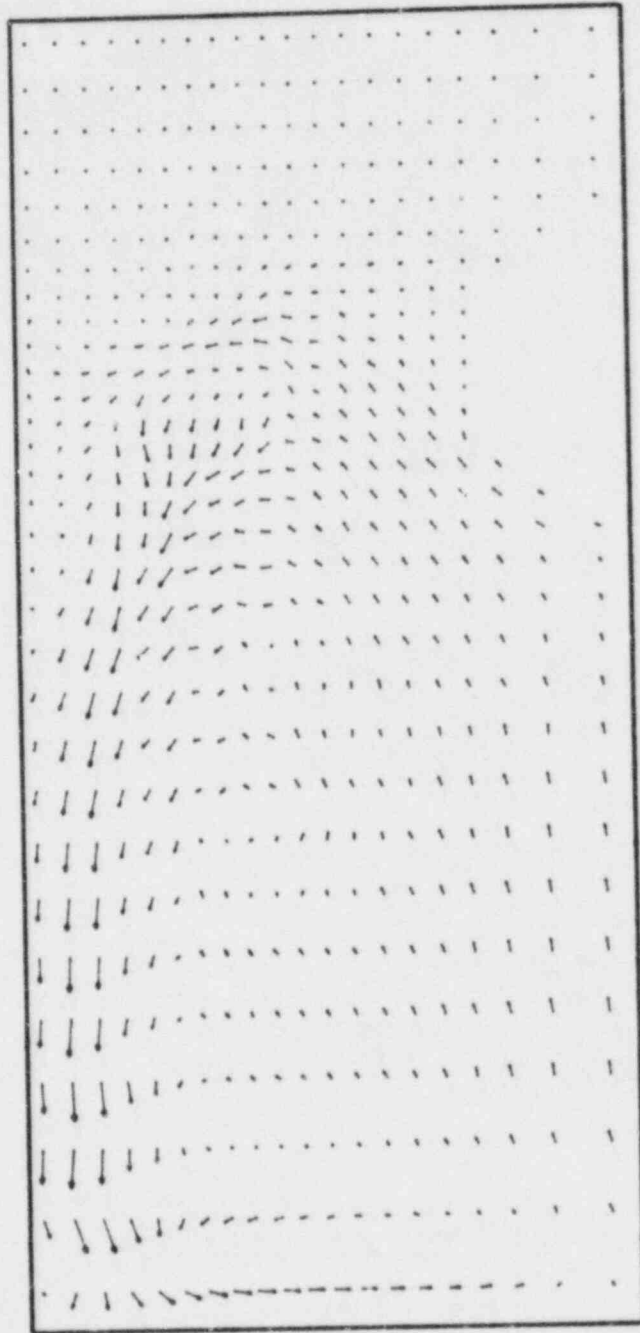


Fig. 39. A velocity vector plot in a vertical plane parallel and adjacent to the vessel wall from a calculation of Creare experiment 50 at 100 s.

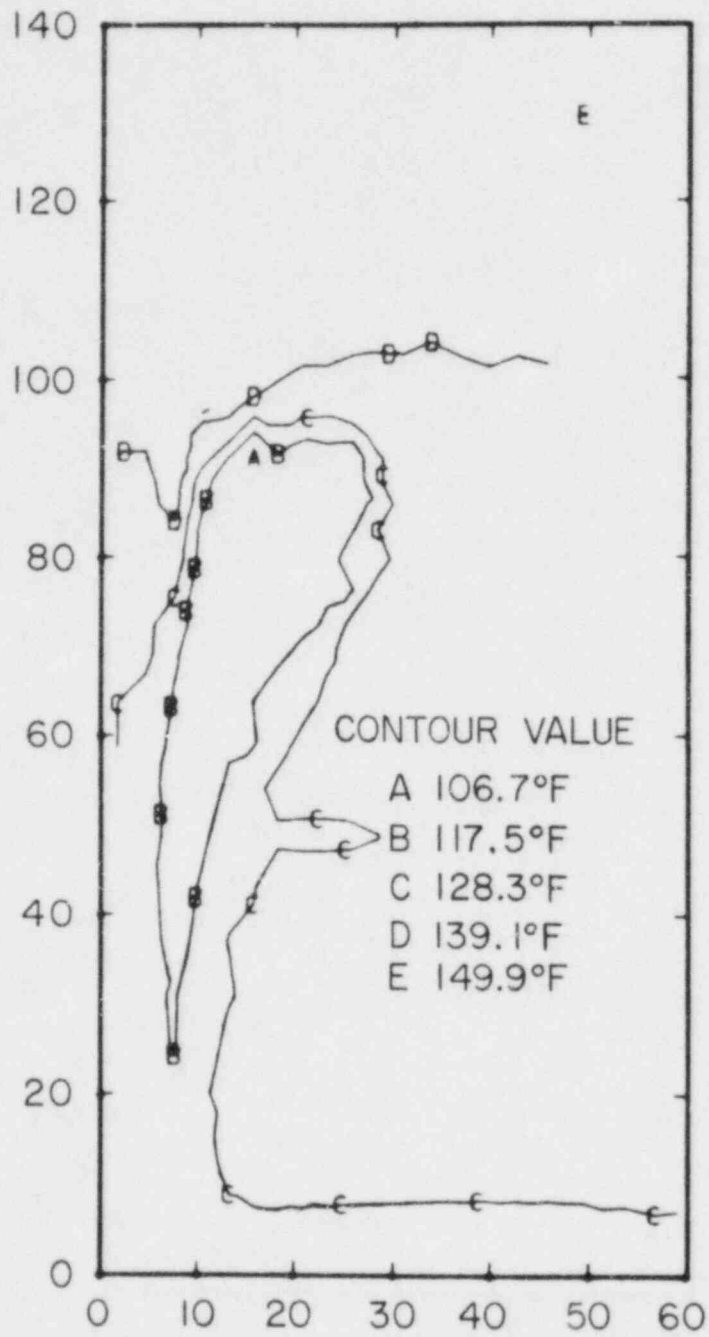


Fig. 40. A temperature contour plot in a vertical plane parallel and adjacent to the core barrel wall from a calculation of Creare experiment 50 at 100 s. This plot shows the azimuthal displacement of the cold water plume.

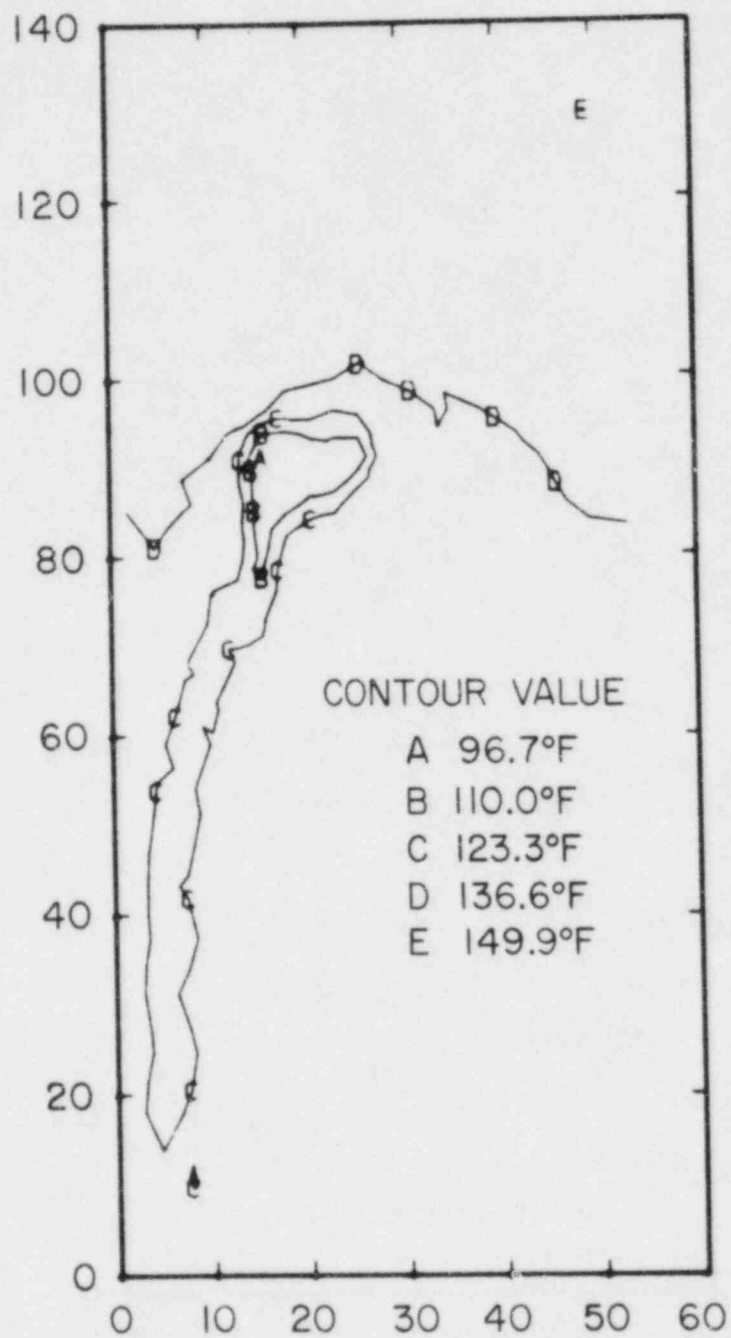


Fig. 41. A temperature contour plot in a vertical plane parallel and adjacent to the vessel wall from a calculation of Creare experiment 50 at 100 s. The cold water penetrates to the bottom of the downcomer in this calculation.

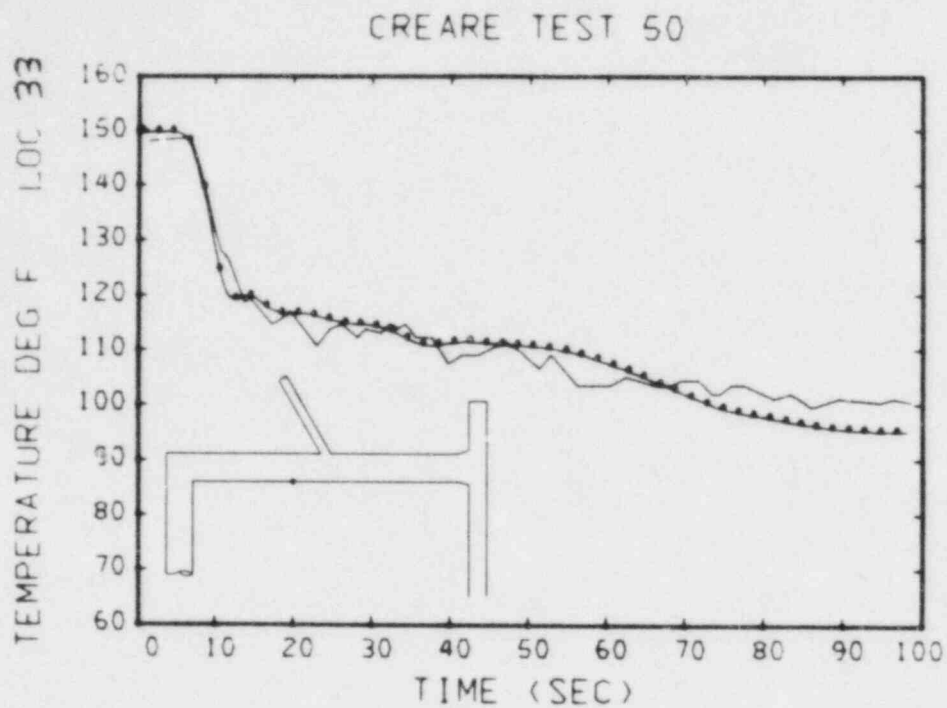


Fig. 42. Comparison between calculated (the datum points) and measured temperature at thermocouple 33.

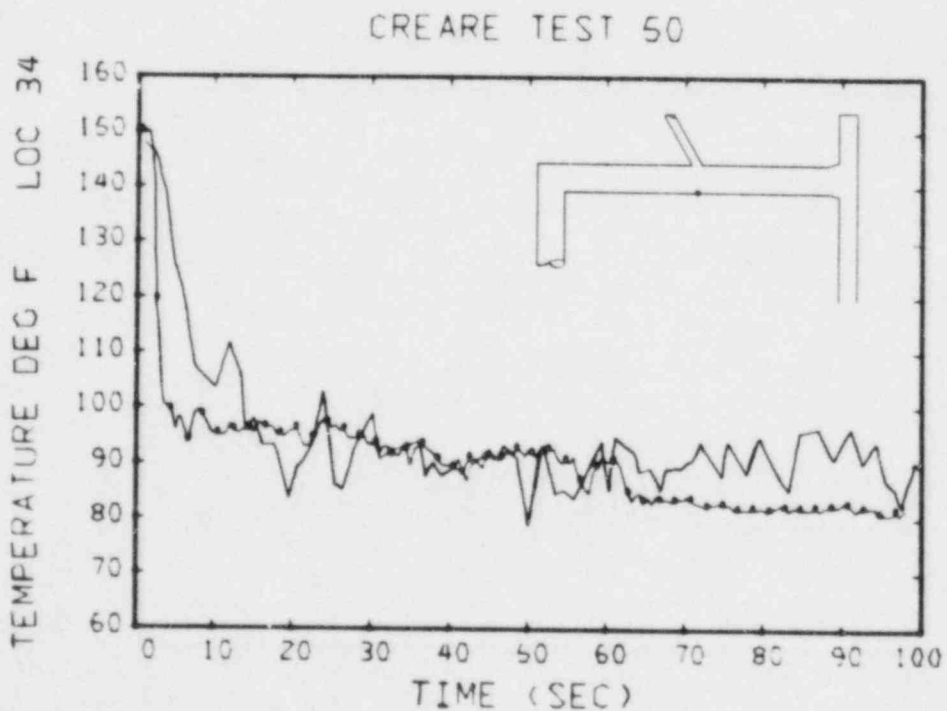


Fig. 43. Comparison between calculated (the datum points) and measured temperature at thermocouple 34.

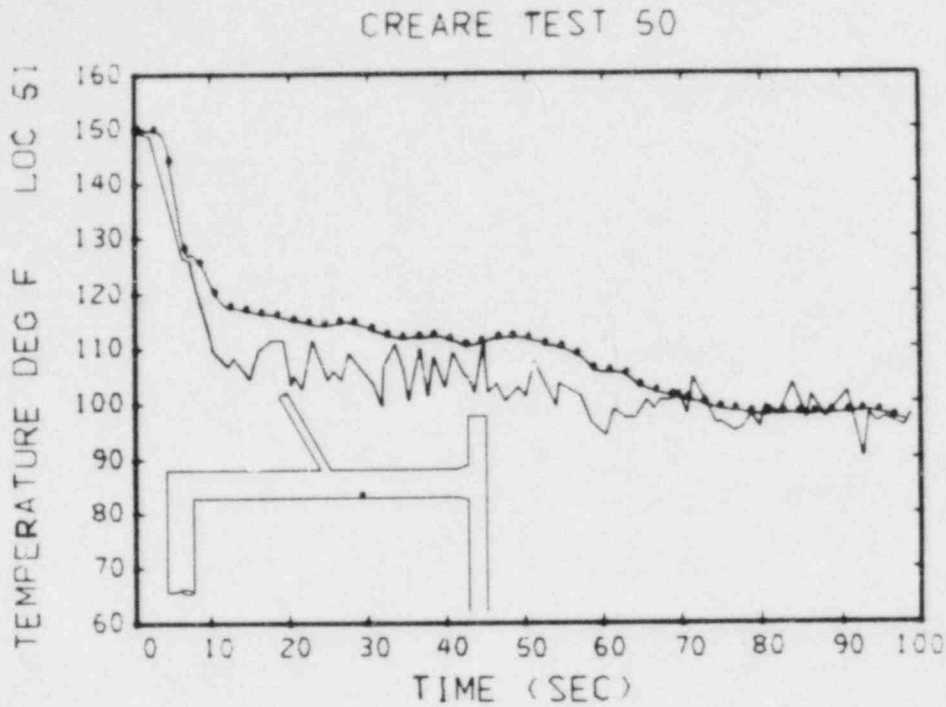


Fig. 44. Comparison between calculated (the datum points) and measured temperature at thermocouple 51.

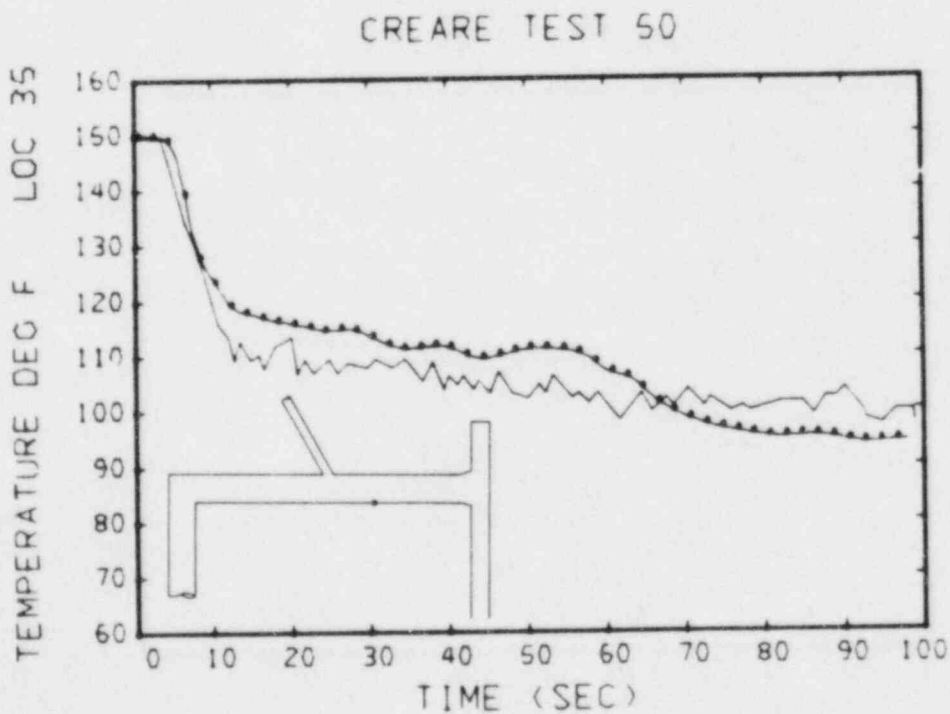


Fig. 45. Comparison between calculated (the datum points) and measured temperature at thermocouple 35.



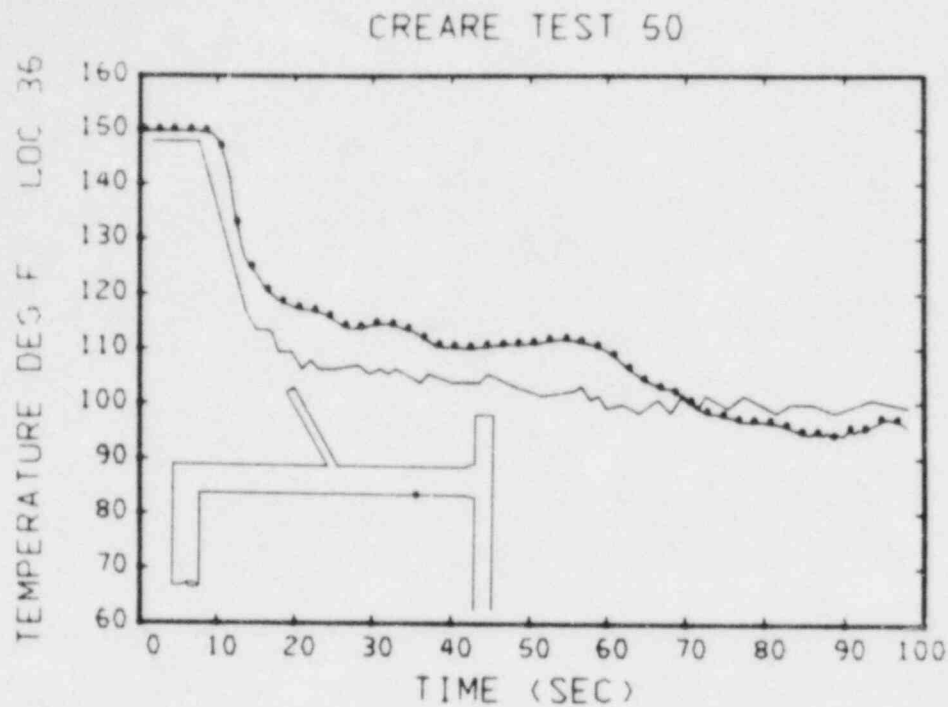


Fig. 46. Comparison between calculated (the datum points) and measured temperature at thermocouple 36.

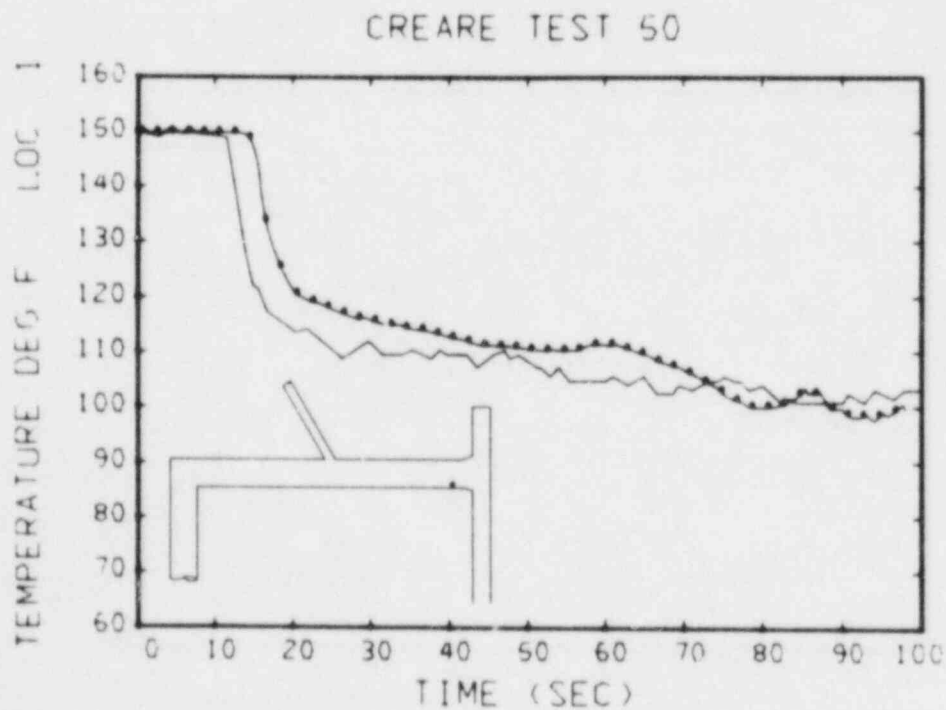


Fig. 47. Comparison between calculated (the datum points) and measured temperature at thermocouple 1.

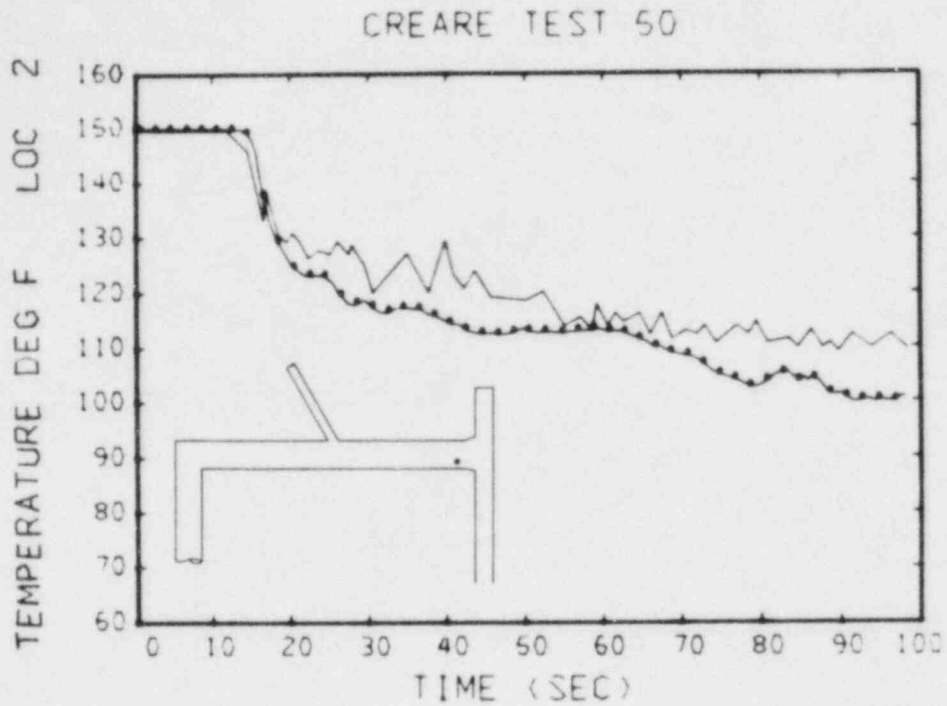


Fig. 48. Comparison between calculated (the datum points) and measured temperature at thermocouple 2.

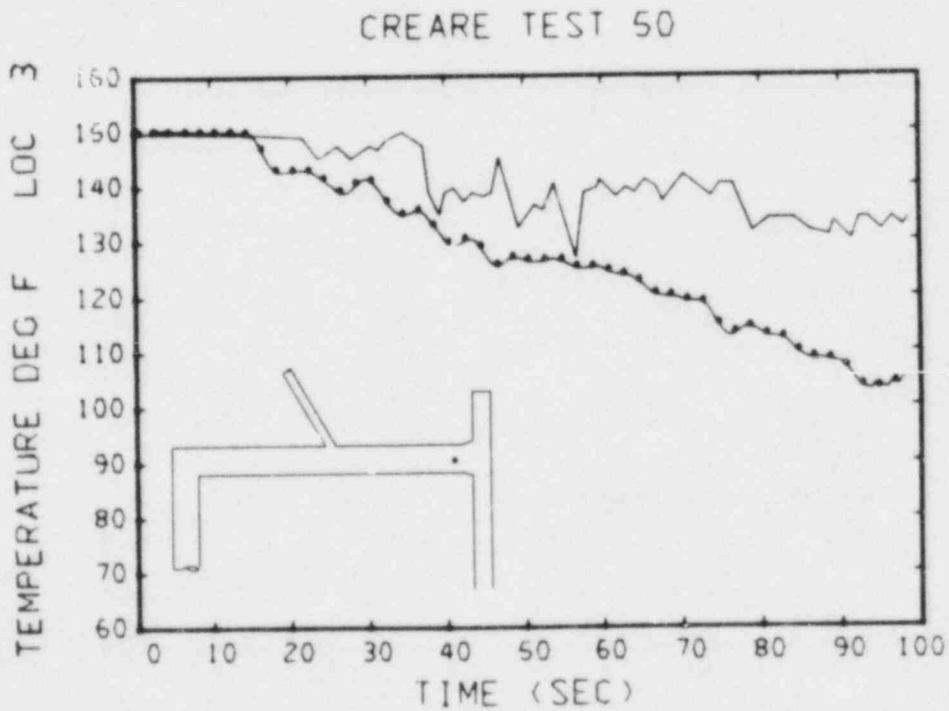


Fig. 49. Comparison between calculated (the datum points) and measured temperature at thermocouple 3.

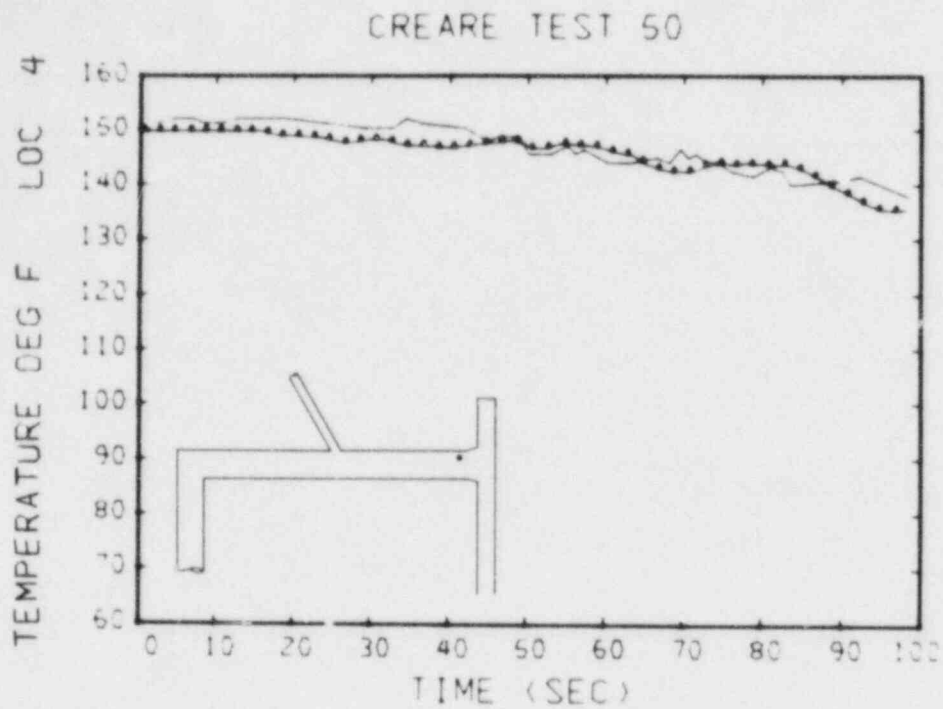


Fig. 50. Comparison between calculated (the datum points) and measured temperature at thermocouple 4.

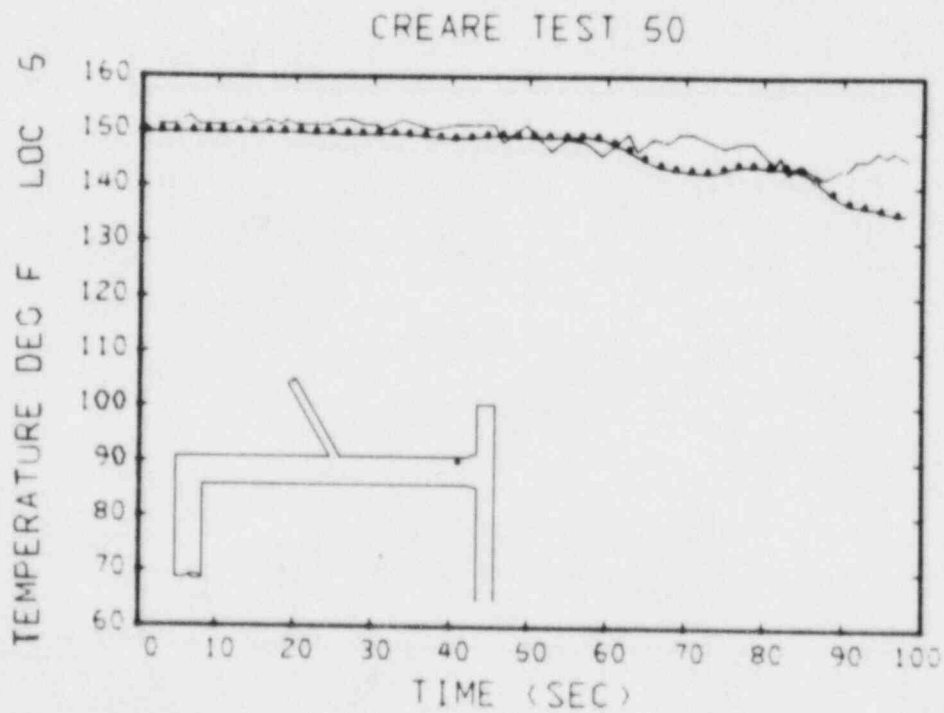


Fig. 51. Comparison between calculated (the datum points) and measured temperature at thermocouple 5.

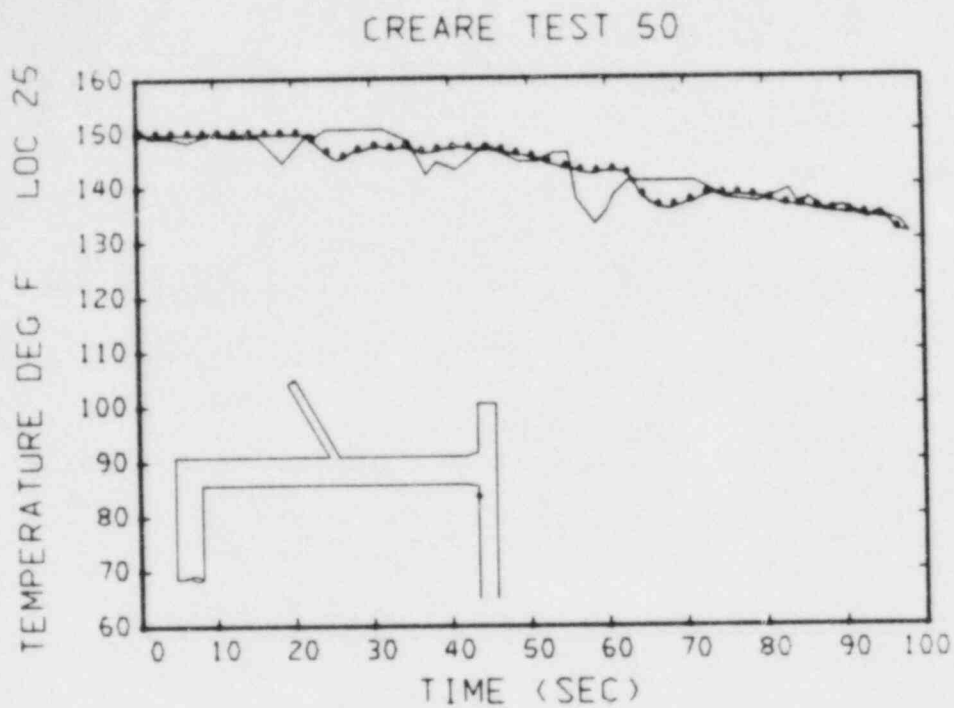


Fig. 52. Comparison between calculated (the datum points) and measured temperature at thermocouple 25.

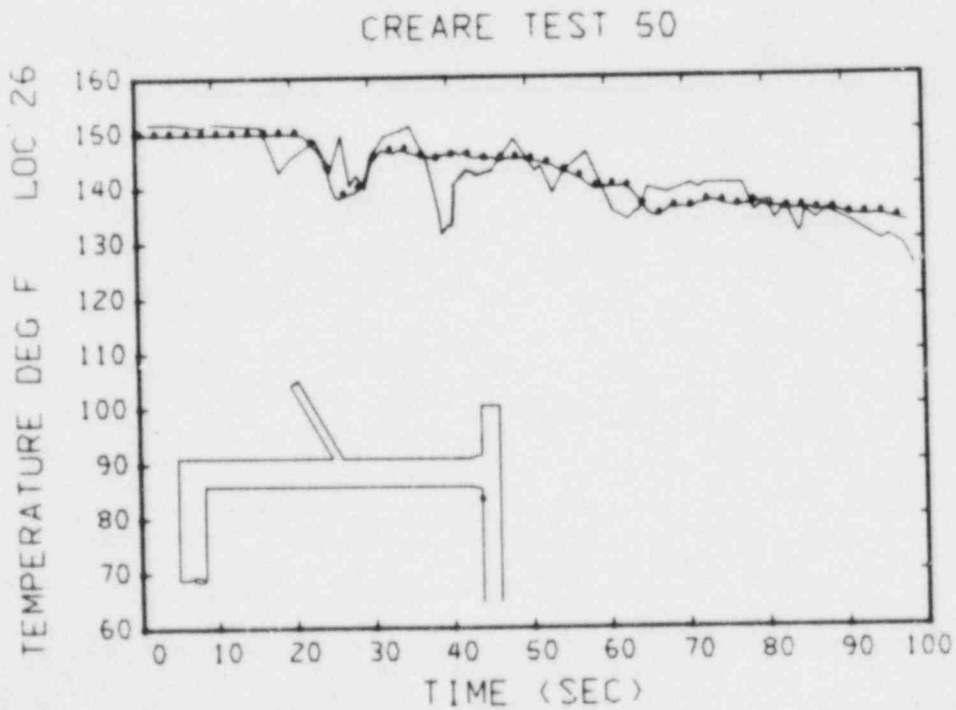


Fig. 53. Comparison between calculated (the datum points) and measured temperature at thermocouple 26.

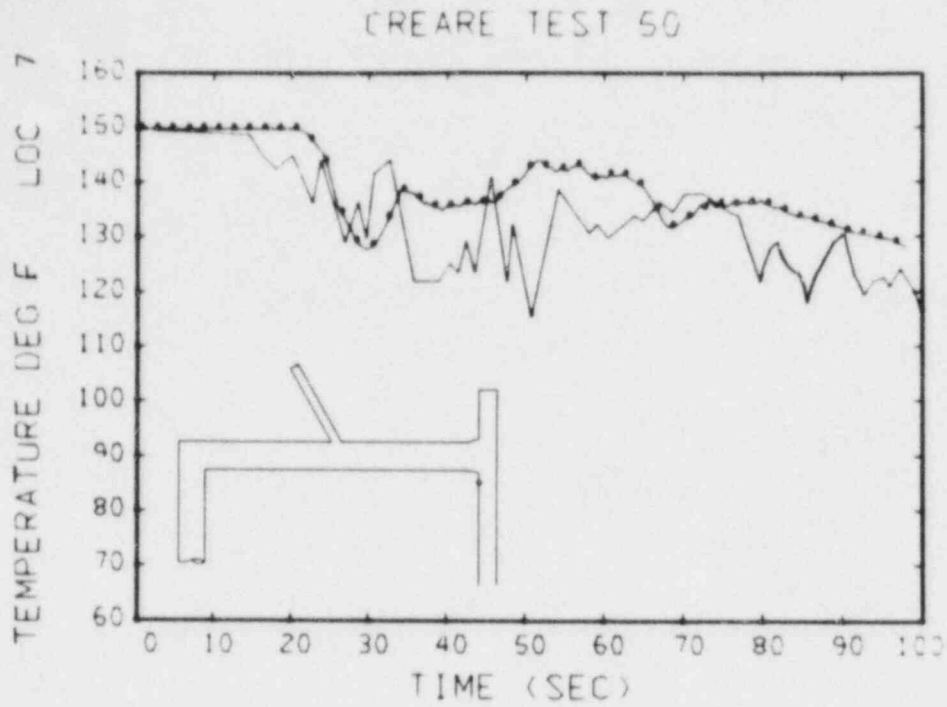


Fig. 54. Comparison between calculated (the datum points) and measured temperature at thermocouple 7.

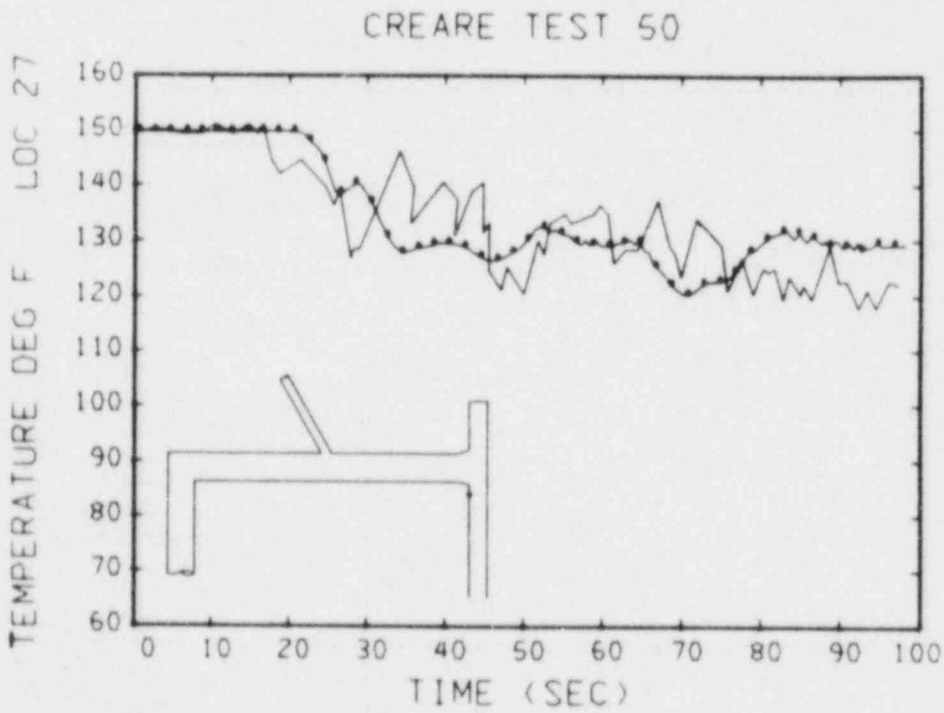


Fig. 55. Comparison between calculated (the datum points) and measured temperature at thermocouple 27.

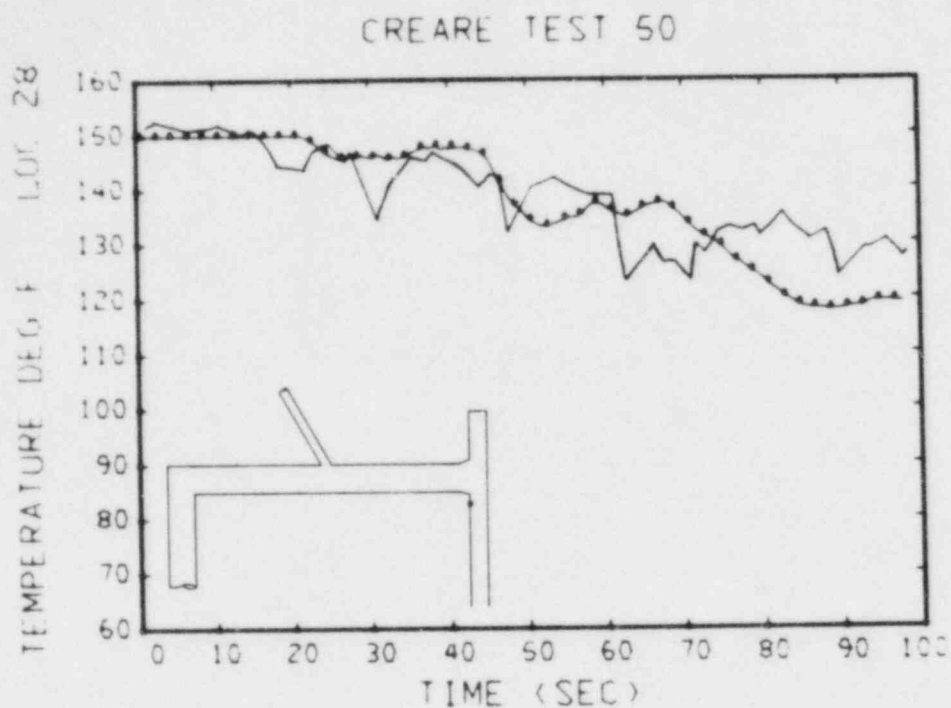


Fig. 56. Comparison between calculated (the datum points) and measured temperature at thermocouple 28.

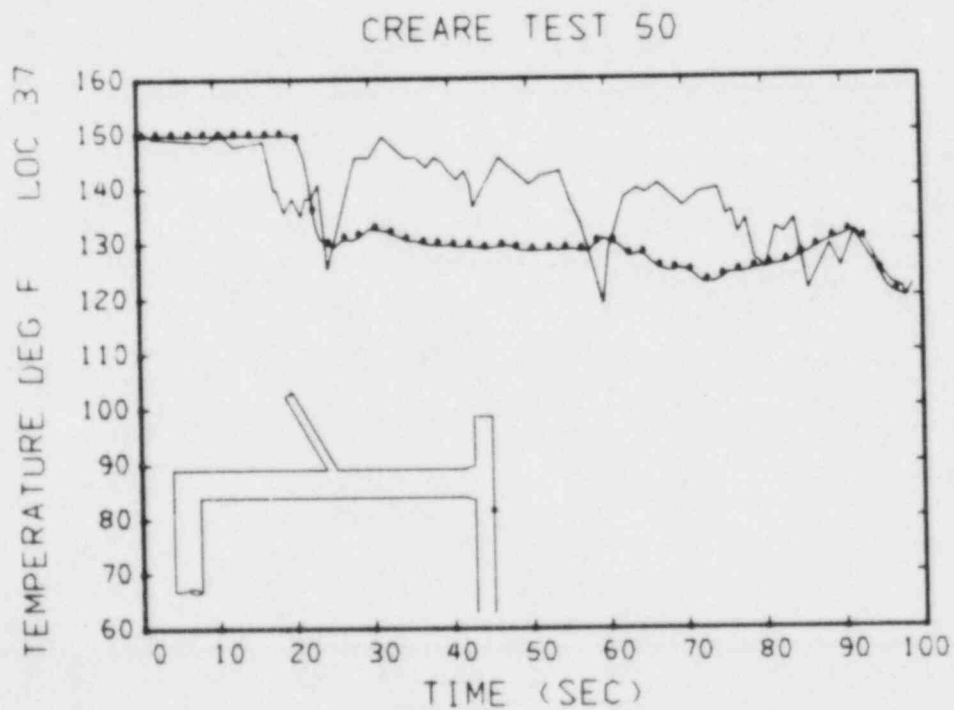


Fig. 57. Comparison between calculated (the datum points) and measured temperature at thermocouple 37.

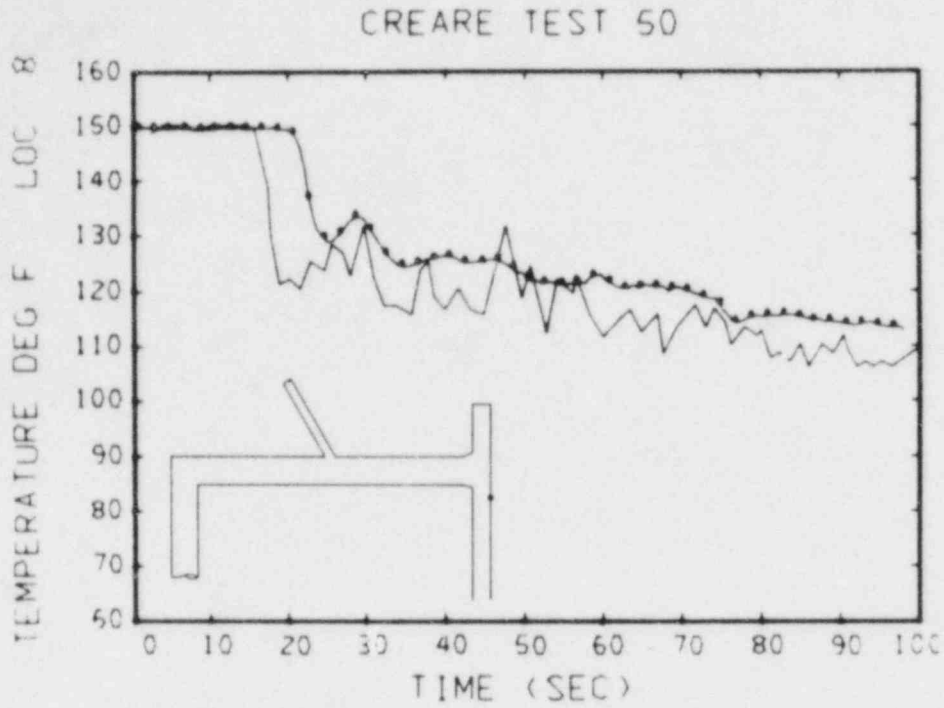


Fig. 58. Comparison between calculated (the datum points) and measured temperature at thermocouple 8.

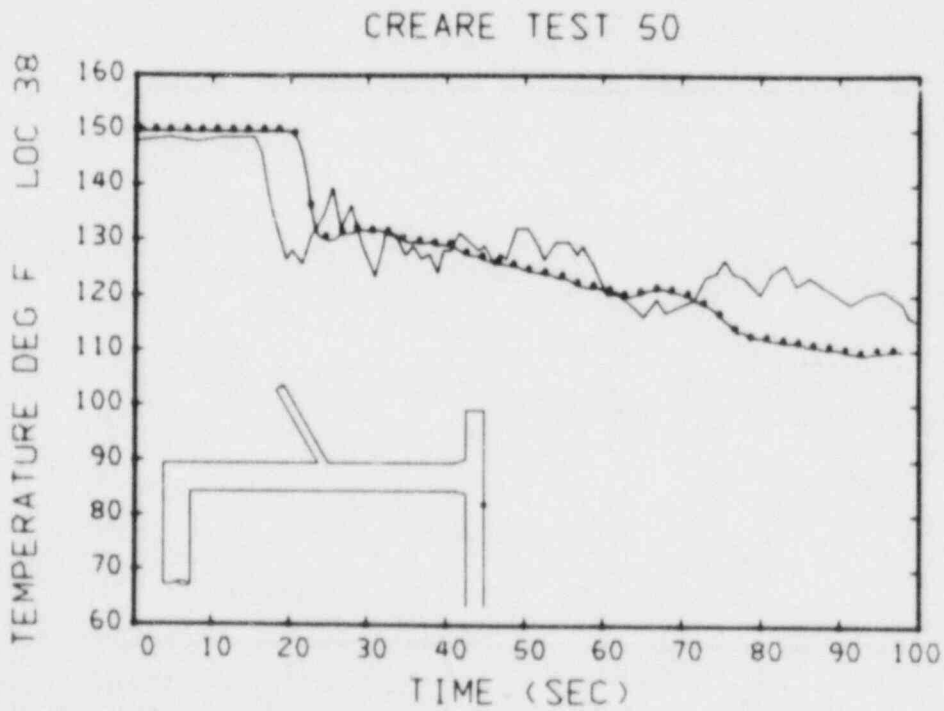


Fig. 59. Comparison between calculated (the datum points) and measured temperature at thermocouple 38.

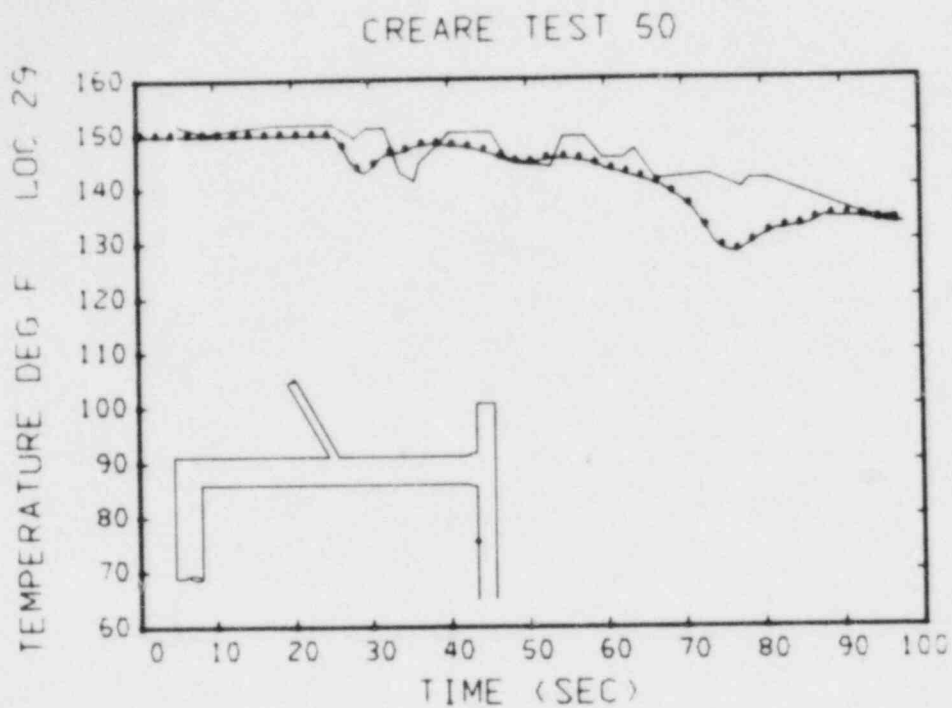


Fig. 60. Comparison between calculated (the datum points) and measured temperature at thermocouple 29.

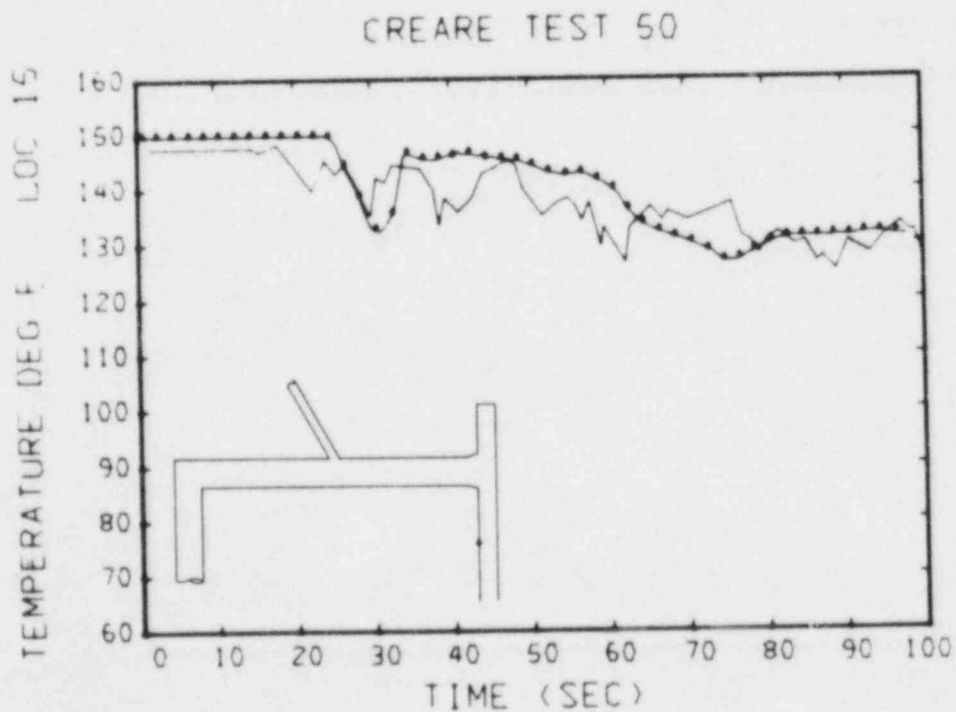


Fig. 61. Comparison between calculated (the datum points) and measured temperature at thermocouple 15.



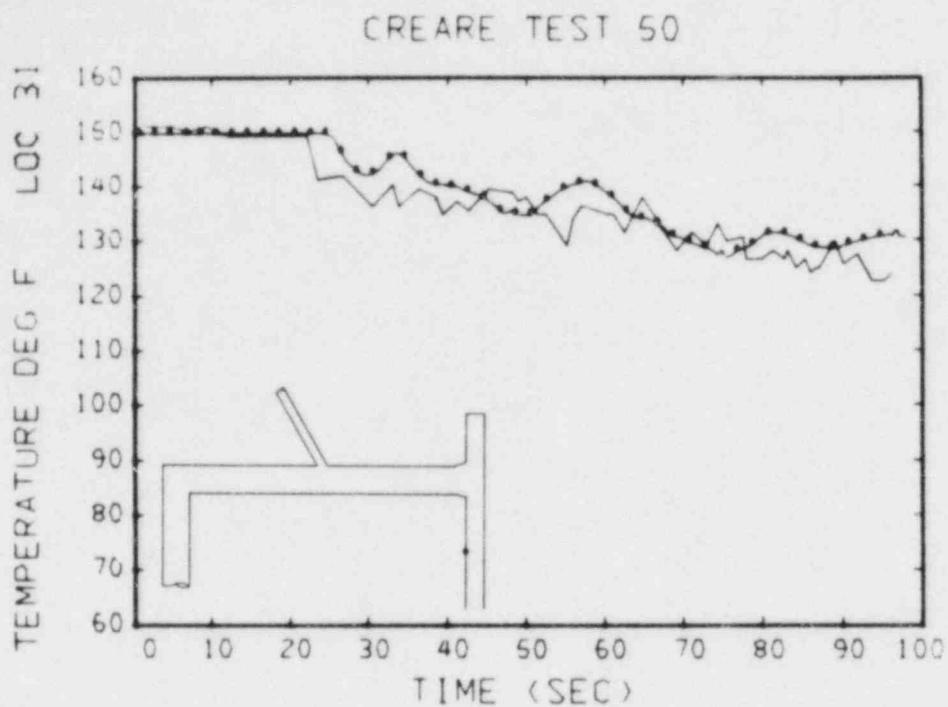


Fig. 62. Comparison between calculated (the datum points) and measured temperature at thermocouple 31.

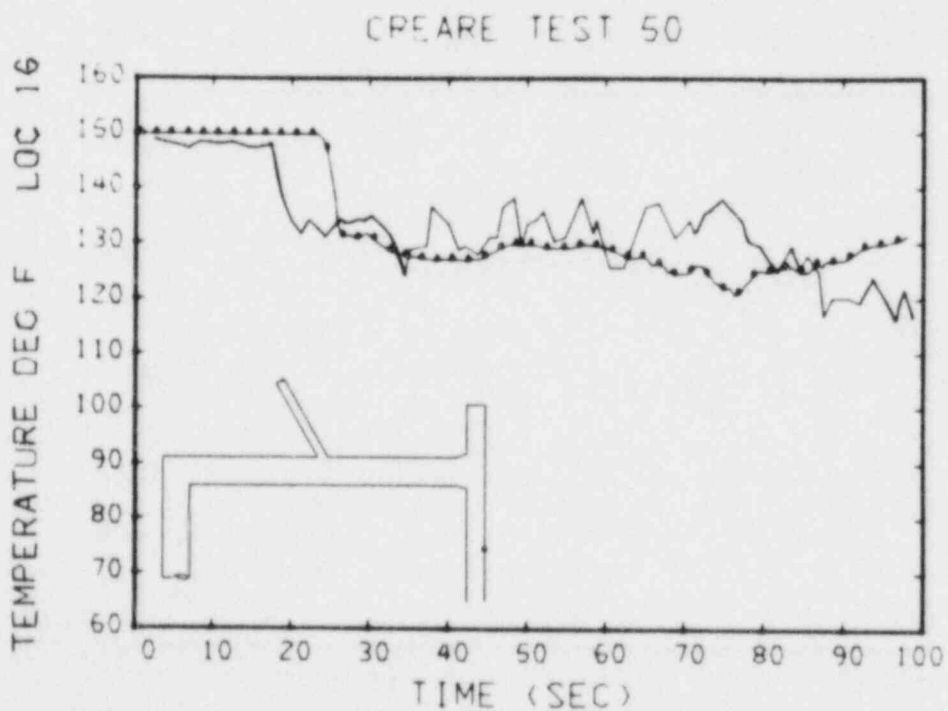


Fig. 63. Comparison between calculated (the datum points) and measured temperature at thermocouple 16.

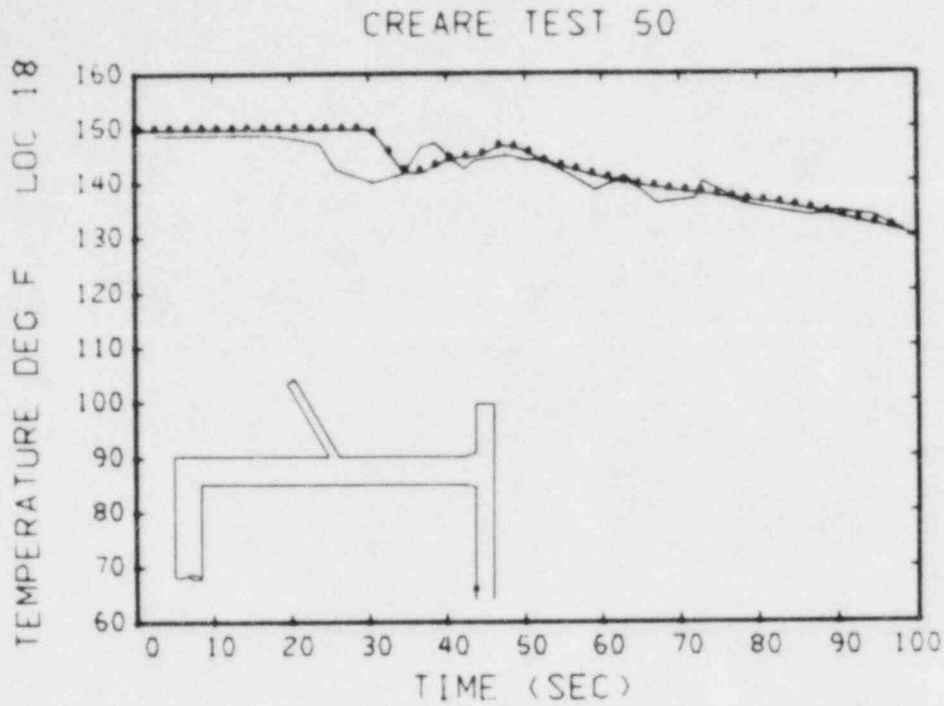


Fig. 64. Comparison between calculated (the datum points) and measured temperature at thermocouple 18.

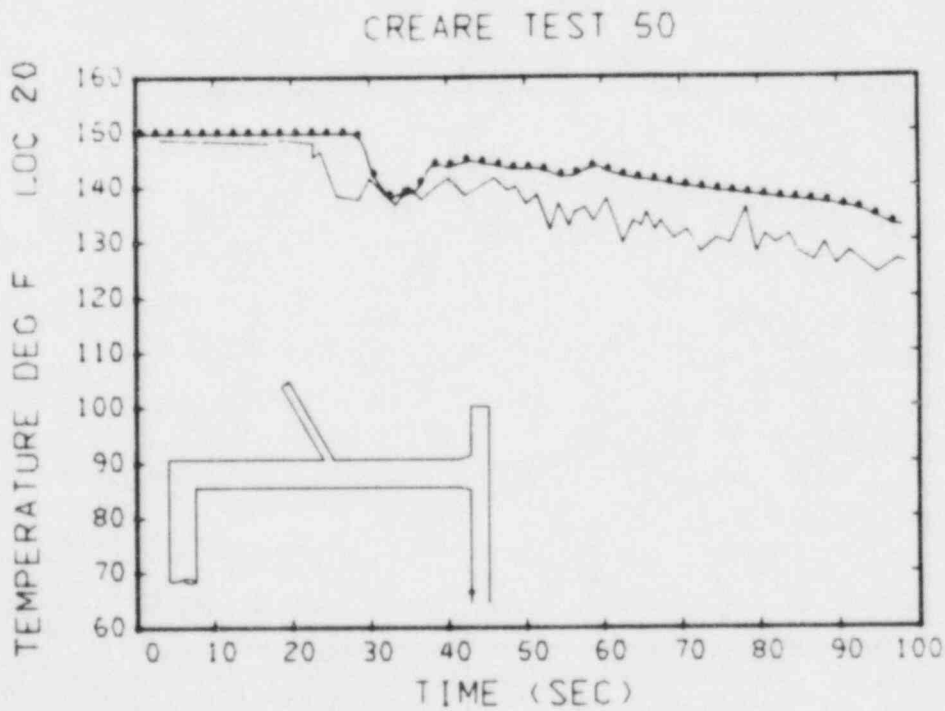


Fig. 65. Comparison between calculated (the datum points) and measured temperature at thermocouple 20.

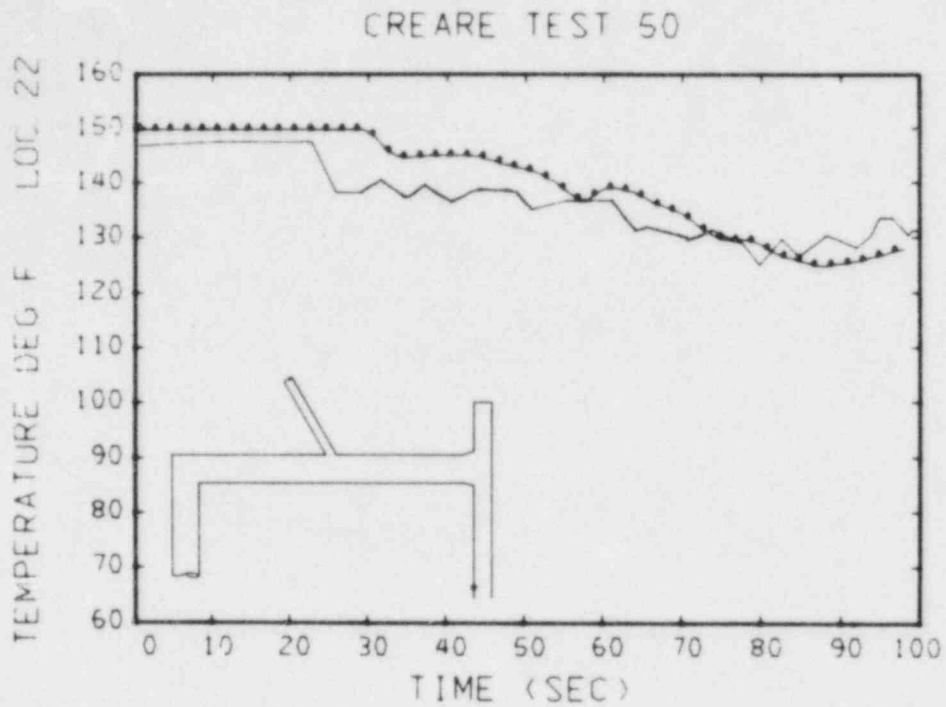


Fig. 66. Comparison between calculated (the datum points) and measured temperature at thermocouple 22.

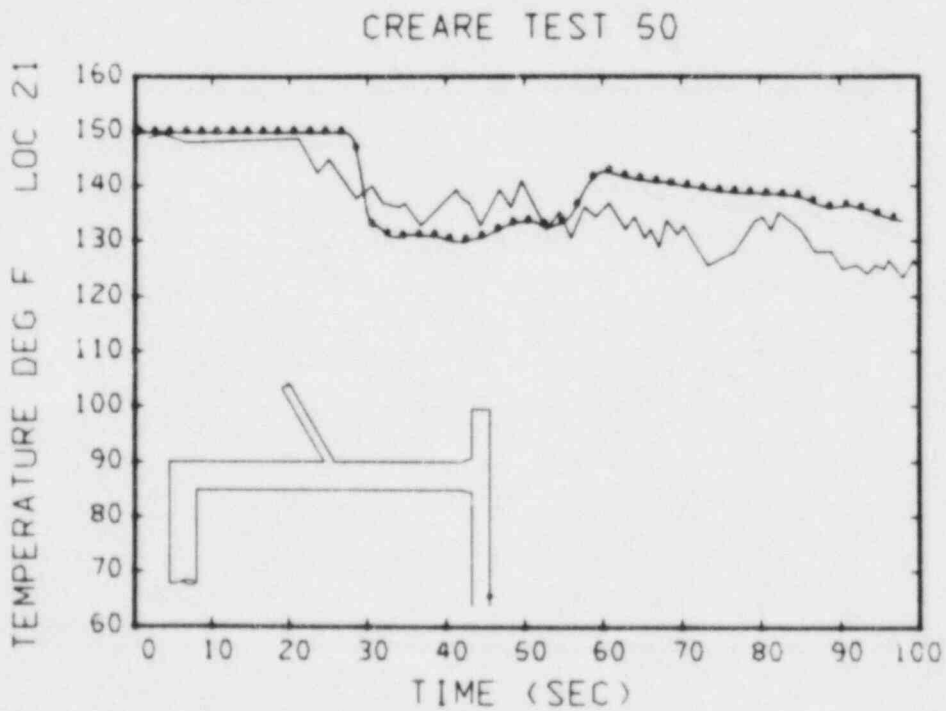


Fig. 67. Comparison between calculated (the datum points) and measured temperature at thermocouple 21.

DISTRIBUTION

	<u>Copies</u>
Nuclear Regulatory Commission, R4, Bethesda, Maryland	406
Technical Information Center, Oak Ridge, Tennessee	2
Los Alamos National Laboratory, Los Alamos, New Mexico	<u>50</u>
Total:	458

**BIBLIOGRAPHIC DATA SHEET**

NUREG/CR-3822  
LA-10132-MS

3 TITLE AND SUBTITLE

SOLA-PTS: A Transient, Three-Dimensional Algorithm for Fluid-Thermal Mixing and Wall Heat Transfer in Complex Geometries

2 LEAVE BLANK

4 RECIPIENT'S ACCESSION NUMBER

5 DATE REPORT COMPLETED

MONTH YEAR  
May 1984

6 AUTHOR(S)

Bart J. Daly, Martin D. Torrey

7 DATE REPORT ISSUED

MONTH YEAR  
July 1984

8 PERFORMING ORGANIZATION NAME AND MAILING ADDRESS (Include Zip Code)

Los Alamos National Laboratory  
Los Alamos, NM 87545

9 PROJECT/TASK/WORK UNIT NUMBER

10 FIN NUMBER

A7306

11 SPONSORING ORGANIZATION NAME AND MAILING ADDRESS (Include Zip Code)

Division of Accident Evaluation  
Office of Nuclear Regulatory Research  
US Nuclear Regulatory Commission  
Washington, DC 20555

12a TYPE OF REPORT

Informal

12b PERIOD COVERED (Inclusive Dates)

13 SUPPLEMENTARY NOTES

14 ABSTRACT (200 words or less)

The SOLA-PTS computer code has been developed to analyze fluid-thermal mixing in the cold legs and downcomer of pressurized water reactors in support of the pressurized thermal shock study. SOLA-PTS is a transient, three-dimensional code with the capability of resolving complex geometries using variable cell noding in the three coordinate directions. The computational procedure is second-order accurate and utilizes a state-of-the-art iteration method that allows rapid convergence to an accurate solution for the pressure field. Two different turbulence models are used in the code, a two-equation  $k-\epsilon$  model that is used in the cold leg pipe away from the HPI inlet and a three-equation  $k-\epsilon-T'^2$  model for use near the HPI inlet and in the downcomer.

The physical modeling and the numerical procedure used in SOLA-PTS are described in this report. Applications of the method to two Creare 1/5th-scale experiments are also presented. Two appendices are included. Appendix A provides a comparison of the two- and three-equation turbulence models, while Appendix B provides instructions for setting up and running a problem with SOLA-PTS.

15a KEY WORDS AND DOCUMENT ANALYSIS

15b DESCRIPTORS

16 AVAILABILITY STATEMENT

17 SECURITY CLASSIFICATION (This report)

Unclassified

18 NUMBER OF PAGES

19 SECURITY CLASSIFICATION (This page)

Unclassified

20 PRICE

\$

